

THERMOELECTRIC EFFECT IN LAYERED NANOSTRUCTURES

**A Thesis Submitted to
the Graduate School of Engineering and Sciences of
İzmir Institute of Technology
in Partial Fulfillment of the Requirements for the Degree of**

DOCTOR OF PHILOSOPHY

in Physics

**by
Gözde ÖZBAL SARGIN**

**July 2019
İZMİR**

We approve the thesis of Gözde ÖZBAL SARGIN

Examining Committee Members:



Prof. Dr. R. Tuğrul SENER
Department of Physics, İzmir Institute of Technology



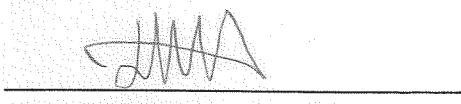
Assoc. Prof. Dr. A. Devrim GÜÇLÜ
Department of Physics, İzmir Institute of Technology



Assoc. Prof. Dr. Hasan ŞAHİN
Department of Photonics, İzmir Institute of Technology



Assoc. Prof. Dr. Cem SEVİK
Department of Mechanical Engineering, Eskişehir Technical University



Assoc. Prof. Dr. Ümit AKINCI
Department of Physics, Dokuz Eylül University

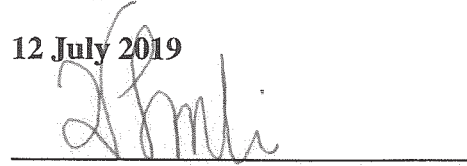


Prof. Dr. R. Tuğrul SENER
Supervisor, Department of Physics
İzmir Institute of Technology



Prof. Dr. Lütfi ÖZYÜZER
Head of the Department of
Physics

12 July 2019



Assoc. Prof. Dr. Haldun SEVİNÇLİ
Co-Supervisor, Department of
Materials Science and Engineering
İzmir Institute of Technology

Prof. Dr. Aysun SOFUOĞLU
Dean of the Graduate School of
Engineering and Sciences

ACKNOWLEDGMENTS

I would first like to express my gratitude to my supervisor Prof. Dr. R. Tuğrul SENER who guide and encourage me through all M.Sc. and Ph.D. process. I feel honored to be supervised by him. I want to give special thanks to my co-advisor Assoc. Prof. Dr. Hâldun Sevinçli for endless support, patience and valuable contributions to this work. I feel fortunate to be able to benefit from his broad and deep knowledge.

I am also thankful to all the members CMP group for their collaboration and delightful discussions. I sincerely appreciate my groupmate Koray Sevim for his great contributions.

My special thanks go to my dear friend Dr. Canan Karahan for giving motivation to keep going and being a sister to me.

I would like to express my deep gratitude to my family's powerful women to teach me overcome every obstacle in my life especially to my lovely mom for her pure love. Finally, I am very grateful to my husband Ozan for his never-ending love, patience and support.

ABSTRACT

THERMOELECTRIC EFFECT IN LAYERED NANOSTRUCTURES

In this thesis, ballistic transport and thermoelectric (TE) properties of semiconducting and dynamically stable two-dimensional materials are investigated by combining first-principles calculations with Landauer formalism. Motivated by finding novel promising TE materials, transition metal dichalcogenides (TMDs) and oxides (TMOs) (namely MX_2 with $\text{M} = \text{Cr, Mo, W, Ti, Zr, Hf}$; $\text{X} = \text{O, S, Se, Te}$) are studied systematically in their 2H- and 1T-phases in Chapter 3. Having computed structural, as well as ballistic electronic and phononic transport properties for all structures, we analyze the thermoelectric properties of the semiconducting ones. We report for the first time that, 2H-phases of four of the studied structures have very promising thermoelectric properties, unlike their 1T-phases.

Next, ballistic transport and thermoelectric (TE) properties of group III-monochalcogenides (group III-VI) are presented in a wide range temperature from 100 K to 1000 K. This large family composed of 25 compounds which stands out with their unique electronic band structures. In addition to Mexican hat shaped (quartic energy-momentum relation) valence band character, some of the structures exhibit valley degeneracies which can occur either in their conduction and valence bands.

Moreover, TE and transport calculations are performed for BO and BS monolayers which consist of lightest species in group III-monochalcogenides. Surprisingly, BO and BS monolayers exhibit high TE efficiency at low temperatures. Low thermal conductance at low temperatures and stepwise electronic transmission at the valence band edge are the physical mechanisms behind achieving large ZT .

ÖZET

KATMANLI NANOYAPILARDA TERMOELEKTRİK ETKİ

Bu tezde ilk prensip hesapları ve Landauer-Büttiker formülasyonu kullanılarak, dinamik kararlılığa sahip yarı iletken iki boyutlu malzemelerin balistik taşınım ve termoelektrik özellikleri incelenmiştir. Umut vadeden yeni termoelektrik malzemeler bulma motivasyonu, geçiş metali dikalkojenitleri ve oksitleri (MX_2 bileşiminde $M = Cr, Mo, W, Ti, Zr, Hf$; $X = O, S, Se, Te$ olmak üzere) 2H- ve 1T-fazlarında sistematik olarak çalışılmıştır. Yapısal, elektronik ve fononik özelliklerinin incelenmesinden sonra, yarı-iletken ve dinamik kararlılığa sahip olan tüm yapıların termoelektrik özellikleri analiz edilmiştir. 1T-fazının tersine, 2H-fazındaki dört yapının termoelektrik özelliklerinin oldukça ümit verici olduğu ilk defa raporlanmıştır.

Geçiş metali ve oksitlerinden sonra, grup III monokalkojenitlerinin balistik taşınım ve termoelektrik özellikleri 100 K'den 1000 K'e kadar geniş bir sıcaklık aralığında sunuldu. 25 bileşimden oluşan bu büyük aile, özgün elektronik bant yapısına sahip olmaları sebebiyle, geriye kalan iki boyutlu yapılar arasında öne çıkmaktadır. Meksika şapkası şeklindeki valans bant yapısına ek olarak bazı yapılar hem iletim hem de valans bandında ortaya çıkabilen vadi dejenerelikleri sergiler.

Ayrıca, grup III-monokalkojenitlerinden en hafif elementleri içeren BO ve BS tek tabakalı yapılarının taşınım ve termoelektrik özellikleri geniş bir sıcaklık aralığında hesaplanmıştır. Şaşırtıcı bir şekilde, BO ve BS tek tabakalıları düşük sıcaklıklarda oldukça yüksek termoelektrik verim vermişlerdir. Düşük sıcaklıklarda yüksek termoelektrik verime sahip olmalarının arkasındaki fiziksel mekanizma, düşük sıcaklıklarda düşük termal iletkenliğe ve termoelektrik performansını arttıran valans bant kenarında basamaklı elektronik ilettime sahip olmalarıdır.

TABLE OF CONTENTS

LIST OF FIGURES	viii
LIST OF TABLES	xi
CHAPTER 1. INTRODUCTION	1
CHAPTER 2. COMPUTATIONAL METHODS	6
2.1. Density Functional Theory: A Brief Introduction	6
2.1.1. Born-Oppenheimer Approximation	7
2.1.2. From Wavefunctions to Electron Density	7
2.1.3. Hohenberg-Kohn Theorems	8
2.1.3.1. Khon-Sham Equations.....	9
2.1.3.2. Local Density Approximation (LDA)	10
2.1.3.3. Generalized Gradeint Approximation (GGA)	11
2.2. Quantum Transport.....	11
2.2.1. Contact Resistance	11
2.2.2. Landauer Formalism and Green Functions	14
2.2.3. Thermoelectric Coefficients	16
CHAPTER 3. TRANSPORT AND THERMOELECTRIC PROPERTIES OF TRANSITION METAL DICHALCOGENIDES AND OXIDES	18
3.1. Structural and Electronic Properties.....	18
3.2. Vibrational Properties	22
3.3. Thermoelectric Properties.....	29
CHAPTER 4. BALLISTIC TRANSPORT AND THERMOELECTRIC PROPERTIES OF GROUP III-VI MONOCHALCOGENIDES	37
4.1. Structural and Electronic Properties.....	37
4.2. Phonon Dispersion Relations and Transmission Spectra	40
4.3. Electronic Transport and Thermoelectric Properties	42
4.3.1. High n-type ZT Depending on Flatness and Valley Degeneracy	44
4.3.2. High n-type ZT Depending on Valley Degeneracy	45

4.3.3. High p-type ZT Depending on Flatness and Valley Degeneracy	48
4.3.4. Quartic Band "Mexican Hat Shape" Effect on ZT	48
CHAPTER 5. BX (X=O,S) MONOLAYERS:PROMISING THERMOELECTRIC PERFORMANCE AT LOW TEMPERATURES	55
5.1. Structural and Electronic Properties	55
5.2. Thermal Transport Properties	57
5.3. Electronic Transport and Thermoelectric Properties	59
CHAPTER 6. CONCLUSION	69
REFERENCES	71
APPENDICES	
APPENDIX A. TEMPERATURE DEPENDENCE OF PHONON THERMAL CONDUCTANCE	86

LIST OF FIGURES

<u>Figure</u>	<u>Page</u>
Figure 3.1. Crystal structures of TMDs and TMOs. The 2H-phase (a), and the 1T-phase (b). The Brillouin zone, reciprocal lattice vectors and the high symmetry points are given in (c).	18
Figure 3.2. Electronic band diagrams of investigated TMDs and TMOs according to PBE results.	21
Figure 3.3. Calculated electronic band structures of selected 2H-MX ₂ compounds; CrO ₂ , TiTe ₂ , ZrTe ₂ , HfTe ₂ based on PBE (red solid line) and PBE+HSE (blue dashed line) functional. Fermi level is set to zero for all subfigures.	23
Figure 3.4. Phonon dispersion relations of investigated TMDs and TMOs.	25
Figure 3.5. Phonon dispersion, phonon transmission spectrum and thermal conductance per length vs temperature of ZrSe ₂ , ZrTe ₂ , HfS ₂ and HfSe ₂ are shown respectively.	26
Figure 3.6. Heat capacities at various temperatures from 300K to 1000 K are shown for the semiconducting compounds in the 2H-phase.	27
Figure 3.7. Heat capacities at various temperatures from 300K to 1000 K are shown for the semiconducting compounds in the 1T-phase.	29
Figure 3.8. Electronic transmission, Seebeck coefficient, power factor and thermoelectric figure of merit are plotted around the Fermi level for 2H-ZrSe ₂ , 2H-ZrTe ₂ , 2H-HfS ₂ and 2H-HfSe ₂	32
Figure 3.9. Electronic band structure of 1T-TiS ₂ with PBE (solid red) and hybrid HSE06 (dashed blue) functionals. Transition from semimetallic to semiconducting phase is occurred with hybrid functional.	33
Figure 3.10. Electronic transport and thermoelectric properties are performed based on HSE06+PBE functional for these narrow gap 2H phases of CrO ₂ , TiTe ₂ , ZrTe ₂ , HfTe ₂ and semimetallic 1T-TiS ₂ compounds.	35
Figure 4.1. Atomic structure of group III-monochalcogenides from (a) top and (b) side view. (c) First Brillouin zone.	37
Figure 4.2. Linear, quadratic and quartic electronic band dispersion.	39
Figure 4.3. The electronic band structures and electronic transmission spectrums of the group III-monochalcogenides calculated at PBE level. Band gap values which are shown shaded area are listed in Table 4.1.	41

Figure 4.4. Calculated electronic band structures of narrow band gap and semi-metallic group III-VI compounds; a) InO, b) TlO, c) TlS, d) TlSe, e) TIPO based on PBE (red solid line) and PBE+HSE (blue dashed line) functional. Fermi level is set to zero for all subfigures.	42
Figure 4.5. Phonon dispersion relations and phonon transmission spectrums for all studied materials.	43
Figure 4.6. Electronic band structure, contour lines at $E-E_{CBM}$ with a value 0.5 (dashed blue), 0.1 (dashed red), 0.005 (dashed yellow) eV and related isoenergy surfaces near the conduction band in the entire brillouin zone of a) BTe b) BSe monolayer.	46
Figure 4.7. Electronic band structure, contour lines at $E-E_{CBM}$ and related isoenergy surfaces near the conduction band in the entire brillouin zone of a) GaS b) GaTe c) TlTe monolayers.	47
Figure 4.8. Electronic band structure, contour lines at $E_{VBM}-E$ and related isoenergy surfaces near the conduction band in the entire brillouin zone of a) GaO b) TlO monolayers.	49
Figure 4.9. Electronic band structure, contour lines at $E_{VBM}-E$ and related isoenergy surfaces near the conduction band in the entire brillouin zone of GaTe monolayer.	52
Figure 5.1. (a) Schematic illustration of the unitcell from the top and side view. (b) and (e) Electronic band structure, density of states, and electronic transmisson spectra of BO and BS monolayer respectively. (c) and (f) Selected contour lines for BO and BS monolayer. (d) and (g) Isoenery surface plot of the selected contour lines which are shown in (c) and (f).	56
Figure 5.2. Phonon dispersion, transmission spectrum and the thermal conductance as a function of tmeperature of BO and BS structures. Red and blue lines indicate that BO and BS monolayers respectively.	58
Figure 5.3. Comparison of logarithmic phonon thermal conductance of BO, BS, InS and three longitudinal-acoustic (LA), transverse-acoustic (TA) and out-of-plane (ZA) acoustic branches belong to BO in a temperature range from 10 K to 100 K.	58
Figure 5.4. n-type and p-type ballistic thermoelectric coefficients of BO monolayer under 100 K.	61
Figure 5.5. n-type and p-type ballistic thermoelectric coefficients of Bs monolayer under 100 K.	63

Figure 5.6. The ratio between phononic and electronic contributions to the thermal conductance of BO, BS and MoS₂ monolayers in a temperature range from 3 K to 100 K. 64

Figure 5.7. Phonon dispersion, transmission spectrum and the thermal conductance of BO and BS structures. Red and blue lines indicate that BO and BS monolayers respectively. 64



LIST OF TABLES

<u>Table</u>	<u>Page</u>
Table 3.1. Structural and electronic properties of semiconducting TMDs and TMOs, which are dynamically stable. The lattice parameter of the unit cell (a), bond lengths (d_{MX}), layer heights (h), bond angles (θ_1, θ_2), band gap (E_g^{PBE}), cohesive energy (E_{coh}), transferred charge to X (ρ_M), charge received by X (ρ_X) and the fractional ionic character (FIC), respectively. Bond lengths and angles are shown in Fig. 3.1 and band structures are illustrated in Fig. 3.2	19
Table 3.2. Thermal conductance per length which is perpendicular to the transport direction for various temperatures.	28
Table 3.3. p - and n -type Seebeck coefficient (S), power factor (P) and thermoelectric figure of merit (ZT) at different temperatures based on PBE calculations.	30
Table 3.4. Difference between chemical potential μ where p -type ZT_{max} (n -type ZT_{max}) is obtained and valence band edge value (conduction band edge) in meV.	36
Table 3.5. p - and n -type ZT values at different temperatures based on the HSE06 calculations.	36
Table 4.1. a is the lattice constant, $d_{III-III}$, d_{VI-VI} and d_{III-VI} are bond lengths, θ_1 and θ_2 show bond angles and E_g gives bandgap of monolayers based on GGA-PBE functional. These structural parameters are illustrated in Fig. 4.1.	51
Table 4.2. Critical wave vector k_c and α parameters of group III-monochalcogenides.	51
Table 4.3. Pnonon thermal conductance values in a wide temperature range from 100 K to 1000 K.	52
Table 4.4. Thermoelectric figure of merit ZT and power factor PF values in which ZT reaches peak value from 100 K to 1000 K.	53
Table 4.5. Seebeck coefficient S and electronic contribution to the thermal conductance κ_{el} values in which ZT reaches peak value from 100 K to 1000 K.	53
Table 4.6. Electronic conductance values G in which ZT reaches peak value from 100 K to 1000 K.	54

Table 5.1. a is the lattice constant, $d_{III-III}$, d_{VI-VI} and d_{III-VI} are bond lengths, θ_1 and θ_2 show bond angles and E_g gives bandgap of monolayers based on GGA-PBE. These structural parameters are also shown in Figure. 5.1. . . 55



CHAPTER 1

INTRODUCTION

Thermoelectric (TE) materials make it possible to drive electric currents using temperature gradients, and conversely cooling of a system just by using a voltage difference, namely the Seebeck and Peltier effects, respectively. Thermoelectric generators (TEG) work based on Seebeck effect and maximum TE efficiency of a TEG is determined by the thermoelectric figure of merit ZT_{TEG} of generator materials and temperature difference between the hot side (T_H) and cold side (T_C) (Snyder (2004); Snyder and Toberer (2008); Snyder and Snyder (2017))

$$\eta = \frac{\Delta T}{T_H} \cdot \frac{\sqrt{1 + ZT_{TEG}} - 1}{\sqrt{1 + ZT_{TEG}} - \frac{T_C}{T_H}} \quad (1.1)$$

where ZT_{TEG} is a device thermoelectric figure of merit which is different from material thermoelectric figure of merit ZT . Similarly, efficiency of thermoelectric or Peltier coolers (TEC) is defined as follows (Snyder et al. (2012)),

$$\phi = \frac{T_C}{\Delta T} \cdot \frac{\sqrt{1 + ZT_{TEC}} - \frac{T_H}{T_C}}{\sqrt{1 + ZT_{TEC}} + 1} \quad (1.2)$$

TEG can provide the power required by TEC device therefore it is possible to combine these devices. Recent study has reported that a new design of TEC-TEG system fulfill a significant increase in the cooling capacity (Lin et al. (2019)). In the rest of the thesis we will discuss material thermoelectric figure of merit ZT .

The TE performance of a material is quantified by the dimensionless figure of merit ZT , which includes strongly interrelated electronic and thermal transport properties. When the charge carrier concentration and ZT relation is investigated, it is seen that insulators and metals are not suitable for being good TE materials. Low charge carrier concentration brings an advantage to obtain high Seebeck coefficient (S), however it reduces electronic conductance (G) in insulators. For metals, charge carrier concentration is sufficiently high, but coexistence of opposite carriers decreases Seebeck coefficient. As a result

semiconductors are most suitable materials for being a promising TE candidate. Because of this interrelation among S and G , it is challenging to achieve high power factor PF which is defined as $PF = S^2G$. Furthermore, low phonon thermal conductance (κ_{ph}) gives rise to high ZT . As a result, significant enhancement of ZT is an extremely difficult task and achieving high PF and low κ_{ph} is a desired scenario for high performance TE materials. Under these circumstances improvement of TE efficiency has been relatively slow, and typical ZT values do not exceed 1 for several bulk materials (Poudel et al. (2008)).

The most well-known TE materials are a class of bulk materials and their alloys, including the Bi_2Te_3 , PbTe , SiGe and CoSb_3 . Bi_2Te_3 -based alloys are most preferred as working material in cooling systems. Electronic and thermal properties of Bi_2Te_3 lead to enhancement in its TE performance (Witting et al. (2019)). In addition, p- and n-type excellent thermoelectric figure of merit values are obtained above 2.0 and 1.8 for mid-temperature PbTe -based materials (Xiao and Zhao (2018)). However, studies on finding cheaper and lead-free TE materials are maintained due to the high cost of the Te and absence of environmentally friendly PbTe -based structures. In this regard, $ZT \sim 0.9$ at 350 K is observed for n-type Mg_3Bi_2 -based materials which are more suitable for practical TE cooling applications (Mao et al. (2019)).

With the advances in the production of low dimensional structures, a new quest for high performance TE materials gained acceleration (Hicks and Dresselhaus (1993a,b); Mahan and Lyon (1994); Hicks et al. (1996); Broido and Reinecke (1995); Dresselhaus et al. (2007)). The advent of atomically thin graphene provided a new platform to study transport and thermoelectric properties in two- and one-dimensions (2D and 1D) (Amollo et al. (2018); Dollfus et al. (2015); Xu et al. (2014)). However, absence of an electronic band gap in 2D graphene and ultra-high thermal conductivity suppress its thermoelectric efficiency (Zuev et al. (2009); Ghahari et al. (2016); Balandin (2011); Jiang et al. (2009); Wang et al. (2011)). Still, there are numerous proposals to enhance the TE performance of graphene (Anno et al. (2015, 2017); D'Souza and Mukherjee (2018); Dragoman and Dragoman (2007); Gunst et al. (2011); Sevinçli et al. (2013); Sevinçli and Cuniberti (2010); Sandonas et al. (2018); Ouyang and Guo (2009); Mazzamuto et al. (2011); Yang et al. (2012); Dollfus et al. (2015)). A more recent family of 2D materials, semiconducting TMDs and TMOs attracted attention due to the wide range of band gaps and lower lattice thermal conductivities. One of the most detailed studies on stability, electronic, mechanical and magnetic analysis of single layer TMDs and TMOs belongs to (Ataca et al. (2012)). Majority of the theoretical studies have been devoted towards MX_2 ($\text{M}=\text{Mo},\text{W}$; $\text{X}=\text{S},\text{Se}$) monolayers (Adessi et al. (2017); Ouyang et al. (2018); Chen et al. (2015); Babaei et al.

(2014); Nakamura (2018); Jin et al. (2015); Huang et al. (2013); Zhang and Zhang (2017); Kumar and Schwingenschlögl (2015)), fewlayers (Arab and Li (2015); Wickramaratne et al. (2014); Kayyalha et al. (2016); Hippalgaonkar et al. (2017); Huang et al. (2014); Wang et al. (2017)), hybrid nano-ribbons (Ouyang et al. (2016); Zhang et al. (2016)) or heterostructures (Wu et al. (2016)) Phonon engineering, (Liu et al. (2018)) band structure engineering (Hong et al. (2016)) and strain engineering (Shen et al. (2017); Dimple et al. (2017); Guo (2016); Zhang and Zhang (2015); Lv et al. (2016)) approaches were also employed extensively with the aim of improving thermoelectric performance of MX_2 structures. In addition to Mo and W based compounds, there are also a few studies Zr and Hf based TMDs in their 1T-phases (Ding et al. (2016); Guo and Wang (2016); Zhen et al. (2017); Guo and Wang (2016); Qin et al. (2017); Lv et al. (2016)) However, a comprehensive study on thermoelectric properties of pristine TMD/TMOs, specifically 2H-phase of Ti, Zr and Hf based structures, is still lacking. In this thesis, we focus on expanding the library of 2D TMD/TMO candidates starting with an investigation of their ballistic properties. Electronic transport, thermal transport and thermoelectric properties of 26 dynamically stable semiconducting TMDs/TMOs are explored. Structural parameters are computed for obtaining accurate electronic band structures and vibrational spectra based on *ab initio* calculations. Thermoelectric coefficients are computed by combining first-principles calculations and Landauer-Büttiker formalism. Also band gap corrections are performed using hybrid HSE06 functionals when necessary.

Compared to TMDs and TMOs, some of the group III-monochalcogenides (MX : $\text{M}=\text{Ga}, \text{In}; \text{X}=\text{S}, \text{Se}, \text{Te}$) have superior optoelectronic and thermoelectric properties due to the moderate as well as tunable band gaps and unique band structures. It is reported that, exfoliated few-layer GaSe and GaTe hold great potential for photodetectors and field-effect transistors (Hu et al. (2012); Li et al. (2014); Lei et al. (2013); Liu et al. (2014); Huang et al. (2016); Late et al. (2012)). Experimental and theoretical efforts have been made to investigate of stability, electronic and optical properties (Mudd et al. (2013); Wang et al. (2019); Zólyomi et al. (2013)), absorption spectra (Antonius et al. (2018)), modulation of optical and electronic properties via strain engineering (Maeso et al. (2019); Ma et al. (2013)) for GaX and InX structures. Band alignment and band edge position analysis show that Ga- and In-monochalcogenides are outstanding 2D materials as photocatalysts for water splitting (Sun et al. (2017); Zhuang and Hennig (2013)). Furthermore mechanical, vibrational and thermal transport properties are systematically studied (Yagmurcukardes et al. (2016); Longinhos and Ribeiro-Soares (2019); Zhou et al. (2018); Zhao et al. (2019); Nissimagoudar et al. (2017); Chang et al. (2019); Pandey

et al. (2017).) Apart from these features, TE properties of Ga- and In-monochalcogenides have attract considerable attention from researchers. However, ballistic transport and TE properties of remaining group III-VI compounds have never been studied. Also, the peculiar valence band shape so called "Mexican Hat Shaped" ("sombbrero shaped") of these compounds have provided motivation to investigate ballistic transport and TE properties of group III-monochalcogenides. Beyond Ga- and In-monochalcogenides we investigate structural, electronic, vibrational, transport and TE properties of all group III oxides and chalcogenides including a total of 25 compounds.

It is well understood that 2D structures, which have a Mexican Hat Shaped (MHS) valence band, are very important for enhancing TE efficiency. Recently exfoliated lead monoxide (α PbO) nanosheets (Kumar et al. (2018); Wang et al. (2017); Das et al. (2018)), monolayer tin oxide (α SnO (Seixas et al. (2016); Daeneke et al. (2017); Saji et al. (2016)), monolayers of Bi_2Te_3 (Zahid and Lake (2010)) and Bi_2Se_3 (Saeed et al. (2014)), biased bilayer graphene (Stauber et al. (2007); Min et al. (2007); Guinea et al. (2006)), group IV-V compounds which belong to $P\bar{6}m2$ space group (Özdamar et al. (2018)), hexagonal group-VA binaries (Sevinçli (2017)) and most of the members of group III-monochalcogenides exhibit quartic energy-momentum relation different from the usual quadratic dispersion (Zólyomi et al. (2013); Rybkovskiy et al. (2014); Ben Aziza et al. (2018); Wickramaratne et al. (2015)). In order to obtain efficient thermoelectric response, both large Seebeck coefficient (S) and low phonon thermal conductivity (κ_{ph}) are necessary. According to the Mott formula sudden changes in density of states (DOS) and electronic transmission spectrum around fermi energy increases S . Quartic dispersion of a valence band resulting in singularity in DOS and step-like behaviour in electronic transmission at the valence band edge. This abrupt change in τ_{el} give rise to S and hence p-type ZT . Theoretical and experimental efforts show that, most studied group III-VI members InSe, GaS, GaSe and GaTe emerge as a promising candidates for high temperature thermoelectric applications (Hung et al. (2017); T. Hung et al. (2019); Zeng et al. (2018); Shangguan et al. (2019)).

It is mentioned that group III-monochalcogenides are potential TE materials due to the having nearly flat band character and band degeneracy result from MHS dispersion. In the last chapter, contrary to expectations heavy compounds yields better TE performance due to the low thermal conductance, we predict the lightest compounds BO and BS possess extraordinary ZT at ultra-low temperatures. This is indeed arises from distinctive trend of ratio of κ_{el}/κ_{ph} at low temperatures. In the literature, very few bulk material can be used for as a thermoelectric material at low temperatures (Bahuguna et al. (2018)). An important

finding is that GaS, GaSe and GaTe monolayers possess maximum figure of merit which is nearly equal to 1 under room temperature (300 K) according to the constant-relaxation time approximation. It is interesting to note that, power factor of Ga-monochalcogenides rises, while ZT decreases with increasing temperature. We perform a detailed analyze on structural, electronic and vibrational properties of BO and BS monolayers before exploring transport and TE properties. Within the ballistic regime, electronic and thermal transport properties are calculated in a wide temperature range from 4 K to 1000 K with the help of *ab – initio* outputs. In addition we present the requirements for synergetic enhancement of TE performance at ultra-low temperatures.



CHAPTER 2

COMPUTATIONAL METHODS

In this chapter we present methodologies that we used for all structural, electronic, vibrational, transport and thermoelectric properties calculations. We performed structural and electronic properties calculations by using first-principles density functional theory (DFT). The fundamentals of DFT are presented mainly based on (Toffoli (2009); Springborg (2000); Martin (2004); Capelle (2002)). In order to obtain phonon dispersion curves of investigated monolayers, inter atomic force constants (IFCs) are calculated by employing density functional perturbation theory (DFPT). Ballistic transport and thermoelectric properties are calculated by using Landauer formalism.

2.1. Density Functional Theory: A Brief Introduction

Many-body Hamiltonian operator of such a system consisting of N_n nuclei and N_e electrons is given as the following

$$\hat{H} = \hat{T} + \hat{V} \quad (2.1)$$

Here, \hat{T} is the kinetic and \hat{V} is the potential term. Potential term includes all possible interactions between electron-electron (V_{ee}), nucleus-nucleus (V_{nn}) and nucleus-electron (V_{ne}). The explicit form of the Hamiltonian in atomic units is given by following equation

$$\hat{H} = -\frac{1}{2} \sum_i^{N_e} \nabla_i^2 - \frac{1}{2} \sum_I^{N_n} \frac{1}{N_{n_I}} \nabla_I^2 - \sum_{i=1}^{N_e} \sum_{I=1}^{N_n} \frac{Z_I}{r_{iI}} + \sum_{i=1}^{N_e} \sum_{j>i}^{N_e} \frac{1}{r_{ij}} + \sum_{I=1}^{N_n} \sum_{J>I}^{N_n} \frac{Z_I Z_J}{R_{IJ}} \quad (2.2)$$

The first two term belonging to kinetic energy of the electrons and nuclei respectively. The remaining terms describe Coulombic (attractive) interaction between electrons and the nuclei and repulsive potential resulting from electron-electron and nucleus-nucleus

interactions. Corresponding Schrödinger equation

$$\hat{H}\Psi_i(\vec{x}_1, \vec{x}_2, \dots, \vec{x}_{N_e}, \vec{R}_1, \vec{R}_2, \dots, \vec{R}_{N_n}) = E_i\Psi_i(\vec{x}_1, \vec{x}_2, \dots, \vec{x}_{N_e}, \vec{R}_1, \vec{R}_2, \dots, \vec{R}_{N_n}) \quad (2.3)$$

The wavefunction embodies all the information related to the quantum system and being a function of three type of coordinate; $3N_e$ spatial coordinates \vec{r}_i , N_e spin coordinates \vec{s}_i in agreement with the Pauli principle, and the $3N_n$ spatial coordinates \vec{R}_I .

2.1.1. Born-Oppenheimer Approximation

In order to simplify this complicated equation Born-Oppenheimer approximation can be applied. This approximation basically express that, nuclei moves much slower than electron due to its big size and heavy mass, therefore dynamics of nuclei and electron can be decoupled. Electrons only see the external potential around the static nuclei (nuclei kinetic energy is zero). Wavefunction takes the following form

$$\Psi_i(\vec{x}_1, \vec{x}_2, \dots, \vec{x}_{N_e}, \vec{R}_1, \vec{R}_2, \dots, \vec{R}_{N_n}) \rightarrow \Psi_{N_e}(r_i) * \Psi_{N_n}(R_I) \quad (2.4)$$

The electronic Hamiltonian consists of three terms

$$\hat{H} = -\frac{1}{2} \sum_i^{N_e} \nabla_i^2 - \sum_{i=1}^{N_e} \sum_{I=1}^{N_n} \frac{Z_I}{r_{iI}} + \sum_{i=1}^{N_e} \sum_{j>i}^{N_e} \frac{1}{r_{ij}} \quad (2.5)$$

$$= \hat{T} + \hat{V}_{en} + \hat{V}_{ee} \quad (2.6)$$

2.1.2. From Wavefunctions to Electron Density

Solving the many-body Schrödinger equation for real materials is a very difficult task. An alternative way to obtain the solution of the Schrödinger equation is defining an

electron density in terms of the individual electron wavefunctions.

$$n(\vec{r}) = \langle \Psi | \hat{n}(\vec{r}) | \Psi \rangle = \sum_{i=1}^{N_e} \int \delta(\vec{r} - \vec{r}_i) |\Psi(\vec{r}_1, \dots, \vec{r}_{N_e})|^2 d\vec{r}_1 \dots d\vec{r}_{N_e} \quad (2.7)$$

$$= N \int |\Psi(\vec{r}, \dots, \vec{r}_{N_e})|^2 d\vec{r}_2 \dots d\vec{r}_{N_e} \quad (2.8)$$

2.1.3. Hohenberg-Kohn Theorems

In 1964, Hohenberg and Kohn published two important theorems (Hohenberg and Kohn (1964))

- Theorem I: For isolated many electron system of interacting particles, the external potential $V_{ext}(\vec{r})$ is uniquely determined by the ground state density $n(\vec{r})$, up to an additive constant.
- Proof: Suppose that there exist two different external potentials $V_{ext}^{(1)}(\vec{r})$ and $V_{ext}^{(2)}(\vec{r})$ each giving the same $n(\vec{r})$. The difference between external potentials is more than just a trivial constant. Consider distinct two trivial wavefunction $\Psi_{ext}^{(1)}(\vec{r})$ and $\Psi_{ext}^{(2)}(\vec{r})$. From the variational principle,

$$E^{(1)} = \langle \Psi^{(1)} | \hat{H}^{(1)} | \Psi^{(1)} \rangle < \langle \Psi^{(2)} | \hat{H}^{(1)} | \Psi^{(2)} \rangle \quad (2.9)$$

$$\langle \Psi^{(2)} | \hat{H}^{(1)} | \Psi^{(2)} \rangle = \langle \Psi^{(2)} | \hat{H}^{(2)} | \Psi^{(2)} \rangle + \int d\vec{r} [V_{ext}^{(1)}(\vec{r}) - V_{ext}^{(2)}(\vec{r})] n_0(\vec{r}) \quad (2.10)$$

$$\langle \Psi^{(1)} | \hat{H}^{(2)} | \Psi^{(1)} \rangle = \langle \Psi^{(1)} | \hat{H}^{(1)} | \Psi^{(1)} \rangle + \int d\vec{r} [V_{ext}^{(2)}(\vec{r}) - V_{ext}^{(1)}(\vec{r})] n_0(\vec{r}) \quad (2.11)$$

By summation of Eq.2.10 and Eq.2.11 we obtain,

$$E^{(1)} + E^{(2)} < E^{(2)} + E^{(1)} \quad (2.12)$$

this inequality reveals the inconsistency and proves that $V_{ext}(\vec{r})$ is a unique functional of $n(\vec{r})$.

- Theorem II: The total energy of a system which is a functional of the associated ground state density, is minimized for the true ground state energy by using variational principle.
- Proof:

$$E[n] = F[n] \int V_{ext}(\vec{r})n(\vec{r})d\vec{r} \quad (2.13)$$

where $F[n]$ is a universal functional that contains all electronic energy; kinetic energy functional $T[n]$ and potential energy functional $V_{ee}[n]$ results from electron-electron interaction. For a system with a unique ground state density $n^{(1)}(\vec{r})$, the ground state energy $E^{(1)}$ is equivalent to the total energy functional $E[n^{(1)}]$,

$$E^{(1)} = E[n^{(1)}] = \langle \Psi^{(1)} | \hat{H}^{(1)} | \Psi^{(1)} \rangle \quad (2.14)$$

By following the variational principle, for a different density $n^{(1)}(\vec{r})$ with a wavefunction $\Psi^{(2)}(\vec{r})$, $E^{(2)}$ is greater than the ground state energy.

$$E^{(1)} = E[n^{(1)}] = \langle \Psi^{(1)} | \hat{H}^{(1)} | \Psi^{(1)} \rangle < \langle \Psi^{(2)} | \hat{H}^{(2)} | \Psi^{(2)} \rangle = E^{(2)} \quad (2.15)$$

In the case of universal functional is known, minimization the total energy of the system with respect to density gives the total energy and electron density of the ground state.

2.1.3.1. Khon-Sham Equations

The challenge is that explicit form of the functional is still unknown. We can write the total energy with multiple terms: kinetic energy, electron-electron interaction and the interaction of electrons with the external potential. The last term is easily defined as a simple functional of electron density that can be seen from Hohenberg-Kohn theorem. The

real problem is writing kinetic part and the electron-electron interaction.

$$\frac{\delta E_e}{\delta \phi_i^*(\vec{r})} = \frac{\delta T_0}{\delta \phi_i^*(\vec{r})} + \frac{\delta E_{ext}}{\delta \phi_i^*(\vec{r})} + \frac{\delta E_H}{\delta \phi_i^*(\vec{r})} + \frac{\delta E_{xc}}{\delta \phi_i^*(\vec{r})} = \epsilon_i \phi_i(\vec{r}) \quad (2.16)$$

ϕ_i are the single-particle orbitals of the non-interaction system.

$$T_0[n] = -\frac{1}{2} \sum_i^{N_e} \langle \phi_i | \nabla^2 | \phi_i \rangle = -\frac{1}{2} \sum_i^{N_e} \int \phi_i^*(x) \nabla^2 \phi_i(x) \quad (2.17)$$

$$\frac{\delta E_e}{\delta \phi_i^*(\vec{r})} = \frac{\delta T_0}{\delta \phi_i^*(\vec{r})} + \frac{\delta E_{ext}}{\delta n(\vec{r})} \frac{\delta n(\vec{r})}{\delta \phi_i^*(\vec{r})} + \frac{\delta E_H}{\delta n(\vec{r})} \frac{\delta n(\vec{r})}{\delta \phi_i^*(\vec{r})} + \frac{\delta E_{xc}}{\delta n(\vec{r})} \frac{\delta n(\vec{r})}{\delta \phi_i^*(\vec{r})} = \epsilon_i \phi_i(\vec{r}) \quad (2.18)$$

$$-\frac{1}{2} \nabla^2 \phi_i(\vec{r}) + [V_{ext}(\vec{r}) + \int d\vec{r}' \frac{n(\vec{r}')}{|\vec{r} - \vec{r}'|} + \epsilon_{xc}(n) + n(\vec{r}) \frac{\delta \epsilon_{xc}(n)}{\delta n(\vec{r})}] \phi_i(\vec{r}) = \epsilon_i \phi_i(\vec{r}) \quad (2.19)$$

These set of equations are called the Kohn-Sham equations.

2.1.3.2. Local Density Approximation (LDA)

Local density approximation (Ceperley and Alder (1980)) is the simplest approximation to $E_{xc}[n]$ and obtained from exchange energy of the homogeneous electron gas. The main idea of LDA is the assumption that it can be written in a simple form as following

$$E_{xc}^{LDA}[n] = \int d\vec{r} n(\vec{r}) \epsilon_{xc}^{HEG}(n(\vec{r})) \quad (2.20)$$

Here, $\epsilon_{xc}^{HEG}(n(\vec{r}))$ is the exchange correlation energy density of a HEG of density n . The exchange part of the $\epsilon_{xc}^{HEG}(n(\vec{r}))$ is known exactly,

$$\epsilon_x^{HEG}(n(\vec{r})) = -\frac{3q^2}{4} \left(\frac{3}{\pi}\right)^{1/3} n^{4/3} \quad (2.21)$$

Therefore,

$$E_x^{LDA}[n] = -\frac{3q^2}{4} \left(\frac{3}{\pi}\right)^{1/3} \int d\vec{r} n(\vec{r})^{4/3} \quad (2.22)$$

LDA is expected to work quite well for systems where the electron density varies slowly. However, LDA is inadequate for most applications in chemistry and exhibit failures in systems including strong correlations.

2.1.3.3. Generalized Gradient Approximation (GGA)

Generalized gradient approximation is a more detailed approximation which can describe the inhomogeneous real systems by taking into account derivative information of the density. The functional have a form (Perdew et al. (1996))

$$E_{xc}^{GGA}[n] = \int d\vec{r} f(n(\vec{r}), \nabla n(\vec{r})) \quad (2.23)$$

Such functionals are referred to as generalized gradient approximations. There are different flavors of GGA, each making a different choice for the function f .

2.2. Quantum Transport

In this section the basics of quantum transport theory are outlined within the Landauer formalism.

2.2.1. Contact Resistance

We consider a simple nanojunction which is composed of ballistic conductor placed between two reservoirs. In the case of size of the conductor is sufficiently large, resistance and hence conductance exist ohmic behaviour

$$R = \frac{V}{I} = \frac{L}{\sigma W} \quad (2.24)$$

$$G^{-1} = \frac{\sigma W}{L} \quad (2.25)$$

where W and L are dimensions of the ballistic conductor and σ denotes conductivity independent of the size or the geometry of the sample. If the length L of the conductor goes to zero one may expect the R to become zero and conductance become infinity. However, experimental results does not confirm this prediction. When L is going to zero, namely dimensions of conductor are shorter than mean free path ($L \ll l_{mfp}$), experimental findings show that conductance takes a finite value G_C . Therefore ballistic conductor has non zero resistance G_C^{-1} which is arises due to limited capacity of the device to transmit and $R_C = G_C^{-1}$ is called as contact resistance.

The Schrödinger equation can be written as

$$\left[E_C + -\frac{\hbar^2}{2m^*} \nabla^2(x, y, z) + V(x, y) \right] \Psi(x, y, z) = E \Psi(x, y, z) \quad (2.26)$$

According to seperation of variables the wavefunction can be written as a product of transverse and longitudinal modes

$$\Psi(x, y, z) = \chi_n(x, y) \phi_n(z) \quad (2.27)$$

where $\phi_n(z) = \alpha_n e^{ik_z z} + \beta_n e^{-ik_z z}$ represent longitudinal modes by combining incoming and outcoming traveling waves.

$$\left[-\frac{\hbar^2}{2m^*} \nabla^2(x, y) + V(x, y) \right] \chi_n(x, y) = \epsilon_n \chi_n(x, y) \quad (2.28)$$

$$E_n(k_z) = E_C + \epsilon_n + \frac{\hbar^2 k_z^2}{2m^*} \quad (2.29)$$

The current density

$$J = nv = n \frac{\vec{p}}{m} \quad (2.30)$$

$$J = \Psi(x, y, z)^* \Psi(x, y, z) \frac{\vec{p}}{m} \quad (2.31)$$

$$J(x, y, z) = \frac{1}{m} \text{Re}[\Psi^*(\vec{p}\Psi)] = \frac{\hbar}{m} \text{Im}[\Psi^*(\nabla\Psi)] \quad (2.32)$$

$$I = -e \int_{-\infty}^{+\infty} dx \int_{-\infty}^{+\infty} dy \vec{J}_z = -\frac{e\hbar}{m} \int_{-\infty}^{+\infty} dx \int_{-\infty}^{+\infty} dy \text{Im} \left[\Psi^* \left(\frac{\partial \Psi}{\partial z} \right) \right] \quad (2.33)$$

$$I_{kn} = -\frac{e\hbar}{m} \text{Im} \left[\phi_n^*(z) \frac{\partial}{\partial z} (\phi(z)) \right] \quad (2.34)$$

There are many possible quantum states for a given quantum number n . The factor of two is included to account for spin degeneracy.

$$I_{kn} = -\frac{2e\hbar}{Lm} \text{Im} \left[e^{-ikz} \frac{\partial}{\partial z} e^{ikz} \right] = -\frac{2e\hbar k}{Lm} = -\frac{2e}{L} v_{kn} \quad (2.35)$$

$$v_{kn} = \frac{1}{\hbar} \frac{\partial E}{\partial k} \quad (2.36)$$

It can be written the current I^+ carried by the $+k$ states as

$$I^+ = -\frac{2e}{L} \sum_{nk} \frac{1}{\hbar} \frac{\partial E_{nk}}{\partial k} f(E_n(k) - \mu_+) \quad (2.37)$$

μ_+ and μ_- are the chemical potentials at two reservoirs. For large L the sum over k can be approximated by an integral according to the formal transition $\sum_k \rightarrow \frac{L}{2\pi} \int dk$ and I^+ takes the following form,

$$I^+ = -\frac{2e}{h} \sum_n \int_0^\infty dk \frac{\partial E_{nk}}{\partial k} f(E_n(k) - \mu_+) \quad (2.38)$$

$$I^+ = -\frac{2e}{h} \sum_n \int_{E_n^{\min}}^{E_n^{\max}} dE f(E - \mu_+) = -\frac{2e}{h} \int_{-\infty}^{+\infty} dE M(E) f(E - \mu_+) \quad (2.39)$$

Here, $M(E)$ is the number of available transverse modes at an energy E and defined as $M(E) = \theta(E - E_n)$. Similarly, I^- can be written as

$$I^- = -\frac{2e}{h} \sum_n \int_{E_n^{\min}}^{E_n^{\max}} dE f(E - \mu_-) = -\frac{2e}{h} \int_{-\infty}^{+\infty} dE M(E) f(E - \mu_-) \quad (2.40)$$

In order to determine net current $I = I^+ - I^-$, we can apply Taylor series expansion around fermi energy at low temperatures

$$f(E - \mu_+) \cong f(E) + \left. \frac{\partial f}{\partial E} \right|_{E_f} (E - \mu_+ - E_f) \quad (2.41)$$

$$f(E - \mu_-) \cong f(E) + \left. \frac{\partial f}{\partial E} \right|_{E_f} (E - \mu_- - E_f) \quad (2.42)$$

$$(2.43)$$

The generalized current is expressed in terms of the "probability that an electron can transmit through the central region".

$$I = I^+ - I^- = -\frac{2e}{h} \int_{-\infty}^{+\infty} dE M(E) \left(-\frac{\partial f(E)}{\partial E} \right) (\mu_- - \mu_+) \quad (2.44)$$

Here, $(\mu_- - \mu_+) = -eV$. Finally at zero temperature with $\left(-\frac{\partial f(E)}{\partial E} \right) \approx \delta(E - E_F)$, quantized conductance is obtained as,

$$G_C = \frac{I}{V} = \frac{2e^2}{h} M(E) \quad (2.45)$$

2.2.2. Landauer Formalism and Green Functions

Landauer expression which is valid in one-, two- and three-dimensional resistors whether appropriate expressions for $\bar{T}(E)$

$$G = \frac{I}{V} = \frac{2e^2}{h} \int_{-\infty}^{+\infty} dE \bar{T}(E) \left(-\frac{\partial f(E)}{\partial E} \right) \quad (2.46)$$

where the $\bar{T}(E)$ is

$$\bar{T}(E) = M(E)T(E) = \frac{\lambda_{el}(E)}{\lambda_{el}(E) + L} M(E) \quad (2.47)$$

This definition of the transmission takes the following forms according to three different regimes

Diffusive Regime: $L \gg \lambda_{el}$; $\bar{T} = \frac{\lambda_{el}}{L} \ll 1$

Ballistic Regime: $L \ll \lambda_{el}$; $\bar{T} \rightarrow 1$

Quasi-ballistic Regime: $L \approx \lambda_{el}$; $\bar{T} < 1$

Electron transmission function, given by

$$T(E) = Tr[\Gamma_L(E)G_{CC}(E)\Gamma_R(E)G_{CC}^\dagger(E)] \quad (2.48)$$

$$(2.49)$$

where $G_{CC}(E)$ and $G_{CC}^\dagger(E)$ are the retarded and advanced Green functions of the central region respectively.

$$G_{CC}(E) = [(E + i\eta) - (H_{CC} - \Sigma_L(E) - \Sigma_R(E))]^{-1} \quad (2.50)$$

Broadening function is the coupling functions of the central region to the left and right leads.

$$\Gamma_{L,R}(E) = i(\Sigma_{L,R}(E) - \Sigma_{L,R}^\dagger(E)) \quad (2.51)$$

Self energies used to include the effect of the left (right) semi-infinite lead.

$$\Sigma_L(E) = H_{CL}g_LH_{LC} \quad (2.52)$$

$$\Sigma_R(E) = H_{CR}g_RH_{RC} \quad (2.53)$$

Here, $g_{L,R}$ is the surface Green's function and described as $g_{L,R} = (E + i\eta - H_{LL,RR})$.

2.2.3. Thermoelectric Coefficients

Derivation of the electronic coefficients is performed by using (Esfarjani et al. (2006))

$$L_n(\mu, T) = -\frac{2}{h} \int dE \tau_{el}(E)(E - \mu)^n \frac{\partial f_{FD}(E, \mu, T)}{\partial E}, \quad (2.54)$$

with n being an integer, $\tau_{el}(E)$ the electronic transmission spectrum and $f_{FD}(E, \mu, T)$ the Fermi-Dirac distribution function at temperature T and chemical potential μ . Using L_n , one can express the electrical conductance (G), Seebeck coefficient (S) and the electrical part of the thermal conductance (κ_{el}). The electrical conductance and electronic contribution to the total thermal conductance are written

$$G(\mu, T) = e^2 L_0 \quad (2.55)$$

and

$$\kappa_{el} = \frac{1}{T} \left(L_2 - \frac{L_1^2}{L_0} \right) \quad (2.56)$$

Seebeck coefficient (thermopower) is described as follows

$$S(\mu, T) = \frac{1}{eT} \frac{L_1}{L_0} \quad (2.57)$$

After obtaining G and S , power factor $PF = S^2G$ can be easily calculated. Phonon thermal conductance is calculated using Landauer formalism Rego and Kirczenow (1998); Sevinçli et al. (2019),

$$\kappa_{\text{ph}} = \frac{1}{2\pi} \int d\omega \hbar\omega \tau_{\text{ph}}(\omega) \frac{\partial f_{\text{BE}}(\omega, T)}{\partial T}, \quad (2.58)$$

where ω is the vibrational frequency, f_{BE} stands for Bose-Einstein distribution function and $\tau_{\text{ph}}(\omega)$ is the phonon transmission spectrum obtained from counting phonon modes with an average of 200 q -points in the transverse direction.

After computing the electronic and phononic contributions to the transport, the dimensionless thermoelectric figure of merit is obtained using,

$$ZT = S^2GT / (\kappa_{\text{el}} + \kappa_{\text{ph}}). \quad (2.58)$$

CHAPTER 3

TRANSPORT AND THERMOELECTRIC PROPERTIES OF TRANSITION METAL DICALCOGENIDES AND OXIDES

3.1. Structural and Electronic Properties

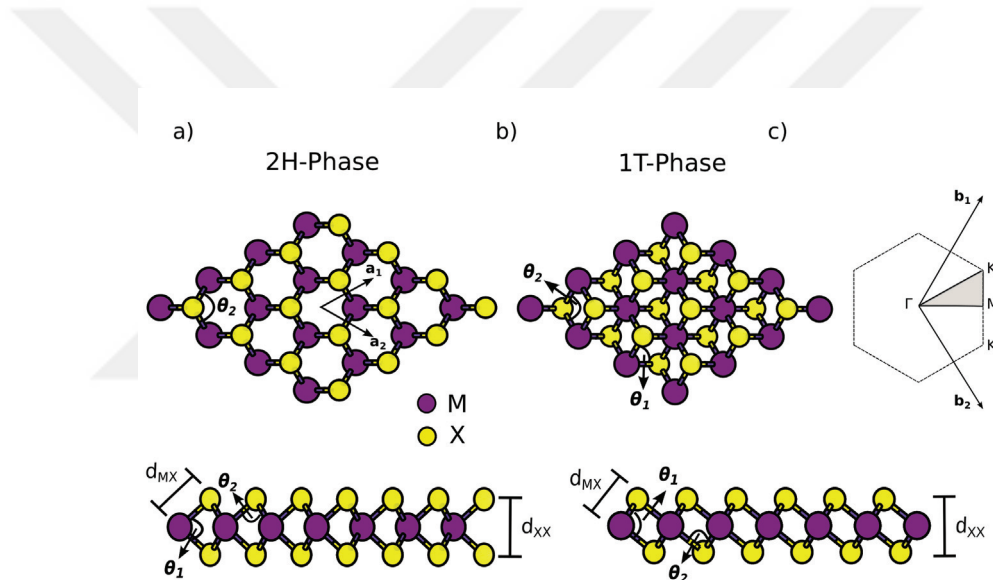


Figure 3.1. Crystal structures of TMDs and TMOs. The 2H-phase (a), and the 1T-phase (b). The Brillouin zone, reciprocal lattice vectors and the high symmetry points are given in (c).

MX_2 monolayers consist of three atomic layers in the sequence of X-M-X. These sublayers are arranged in the well-known two phases (polymorphs); trigonal prismatic 2H which is a member of $P\bar{6}m2$ (D_{3h}) symmetry group and octahedral 1T which belongs to the $P\bar{3}m1$ (D_{3d}). Schematic representation of 2H- and 1T-phases from top and side views are shown in Fig. 3.1(a) and Fig. 3.1(b), respectively, and their first Brillouin zone is given in Fig. 3.1(c).

Table 3.1. Structural and electronic properties of semiconducting TMDs and TMOs, which are dynamically stable. The lattice parameter of the unit cell (a), bond lengths (d_{MX}), layer heights (h), bond angles (θ_1, θ_2), band gap (E_g^{PBE}), cohesive energy (E_{coh}), transferred charge to X (ρ_M), charge received by X (ρ_X) and the fractional ionic character (FIC), respectively. Bond lengths and angles are shown in Fig. 3.1 and band structures are illustrated in Fig. 3.2

MX ₂	Phase	a	d_{MX}	h	θ_1	θ_2	E_g^{PBE}	E_{coh}	ρ_M	ρ_X	FIC
		(Å)	(Å)	(Å)	(deg)	(deg)	(eV)	(eV/atom)	(e^-)	(e^-)	(%)
CrO ₂	2H	2.63	1.91	2.32	74.77	86.96	0.37	5.34	1.48	-0.74	54.51
CrS ₂	2H	3.04	2.29	2.94	79.82	83.26	0.93	4.17	1.00	-0.50	19.07
CrSe ₂	2H	3.21	2.43	3.14	80.59	82.68	0.75	3.64	0.81	-0.41	17.97
CrTe ₂	2H	3.48	2.64	3.41	80.63	82.66	0.53	3.09	0.56	-0.28	4.73
MoO ₂	2H	2.83	2.05	2.47	74.18	87.39	0.91	6.24	1.67	-0.84	33.61
MoS ₂	2H	3.18	2.41	3.13	80.77	82.55	1.67	5.14	1.07	-0.57	4.31
MoSe ₂	2H	3.32	2.54	3.34	82.12	81.54	1.44	4.60	0.83	-0.42	3.73
MoTe ₂	2H	3.55	2.73	3.61	82.74	81.07	1.08	4.04	0.52	-0.26	0.09
WO ₂	2H	2.83	2.05	2.48	74.34	87.27	1.36	7.02	1.83	0.92	25.29
WS ₂	2H	3.19	2.42	3.14	80.87	82.47	1.79	5.80	1.21	-0.61	1.2
WSe ₂	2H	3.32	2.55	3.35	82.44	81.30	1.54	5.19	0.92	-0.46	0.9
WTe ₂	2H	3.55	2.74	3.62	82.89	80.96	1.06	4.54	0.58	-0.29	1.68
TiS ₂	2H	3.34	2.45	3.02	75.99	86.07	0.73	5.17	1.49	-0.75	23.69
TiSe ₂	2H	3.49	2.58	3.24	77.61	84.89	0.60	4.68	1.39	-0.70	22.51
TiTe ₂	2H	3.74	2.80	3.57	79.28	83.66	0.19	4.12	1.23	-0.61	7.54
ZrO ₂	1T	3.28	2.12	1.93	79.05	100.95	4.44	7.71	2.54	-1.27	67.14
ZrS ₂	1T	3.69	2.57	2.90	88.59	91.41	1.20	5.89	2.05	-1.02	32.34
ZrSe ₂	2H	3.71	2.73	3.38	76.61	85.62	0.79	5.21	1.80	-0.90	31.07
	1T	3.80	2.71	3.17	90.73	89.27	0.51	5.35	1.87	-0.94	31.07
ZrTe ₂	2H	3.93	2.94	3.73	78.83	83.99	0.45	4.62	1.58	-0.79	13.78
HfO ₂	1T	3.24	2.11	1.93	79.38	100.62	4.87	7.90	2.32	-1.16	68.17
HfS ₂	2H	3.53	2.57	3.13	74.92	86.85	1.09	5.78	1.84	-0.92	33.61
	1T	3.64	2.55	2.89	88.90	91.11	1.29	6.00	1.91	-0.95	33.61
HfSe ₂	2H	3.67	2.70	3.36	76.78	85.50	0.88	5.25	1.68	-0.84	32.34
	1T	3.76	2.68	3.14	90.92	89.08	0.60	5.42	1.76	-0.88	32.34
HfTe ₂	2H	3.90	2.91	3.69	78.63	84.14	0.36	4.61	1.48	-0.74	14.79

We first perform geometry optimizations and check the dynamical stabilities of the TMD/TMO monolayers by checking whether all vibrational frequencies are real and positive. The geometrical optimization and electronic structure calculations are performed using density functional theory (DFT) using plane-wave basis sets (Kresse and Furthmüller (1996)) by employing projector augmented wave (PAW) potentials (Kresse and Joubert (1999)). The exchange-correlation potential has been approximated by generalized gradient approximation (GGA) using Perdew–Burke–Ernzerhof (PBE) functionals (Perdew et al. (1996)). The plane-wave cut off energies are found to be in the range from 250 to 500 eV with convergence tests for each structure. The irreducible Brillouin zone is sampled using Monkhorst-Pack scheme with grid sizes of $n \times n \times 1$ ($n = 5 - 15$) according to the convergence tests (Monkhorst and Pack (1976)). The convergence thresholds for ionic and electronic relaxations are set to 10^{-3} eV/Å and 10^{-6} eV, respectively. During the geometry optimization process, cell shape and volume are preserved. The vacuum spacing is set to 15 Å to avoid any spurious interactions between layers. While all 2H structures group-VIB (Cr, Mo, W) TMDs/TMOs are dynamically stable semiconductors, their 1T-phases are unstable. Their distorted 1T_d phases are dynamically stable, but all are metallic and therefore they are not within the scope of this study. On the other hand, both 2H and 1T-phases of group-IVB (Ti, Zr, Hf) TMDs/TMOs are dynamically stable and semiconducting. The structural parameters which determine the geometry are tabulated in Table 3.1. The obtained parameters are in good agreement with the literature (Rasmussen and Thygesen (2015)). For a given phase, d_{MX} increases with increasing a . However, different phases (2H and 1T) of a given MX₂ (ZrSe₂, HfS₂ and HfSe₂) follow an opposite trend. For example, 1T-phase of ZrSe₂ has larger a than its 2H-phase, but smaller d_{MX} and h . For these structures, a is always larger for the 1T-phase, whereas d_{MX} is reduced by $\sim 0.7\%$ and h is reduced by $\sim 6-7\%$. Bond angles θ_1 and θ_2 follow opposite trends. Comparing two MX₂ structures, one observes that the structure with larger θ_1 has smaller θ_2 . Also θ_1 of the 1T-phase of a given structure is always larger than that in the 2H-phase.

The cohesive energy (E_c) per atom is computed as

$$E_{\text{coh}} = (n_X E_X + n_M E_M - E_{MX_2}) / (n_X + n_M). \quad (3.1)$$

Here, $n_{X(M)}$ denotes the number of chalcogen (transition metal) atoms in the unit cell. $E_{X(M)}$ is the energy of the isolated single atoms, and E_{MX_2} is the total energy of the MX₂ monolayer. For compounds of the same phase, E_{coh} decreases with increasing a as expected. A comparison of 2H- and 1T-phases of the same TMD reveal that E_{coh} is always larger

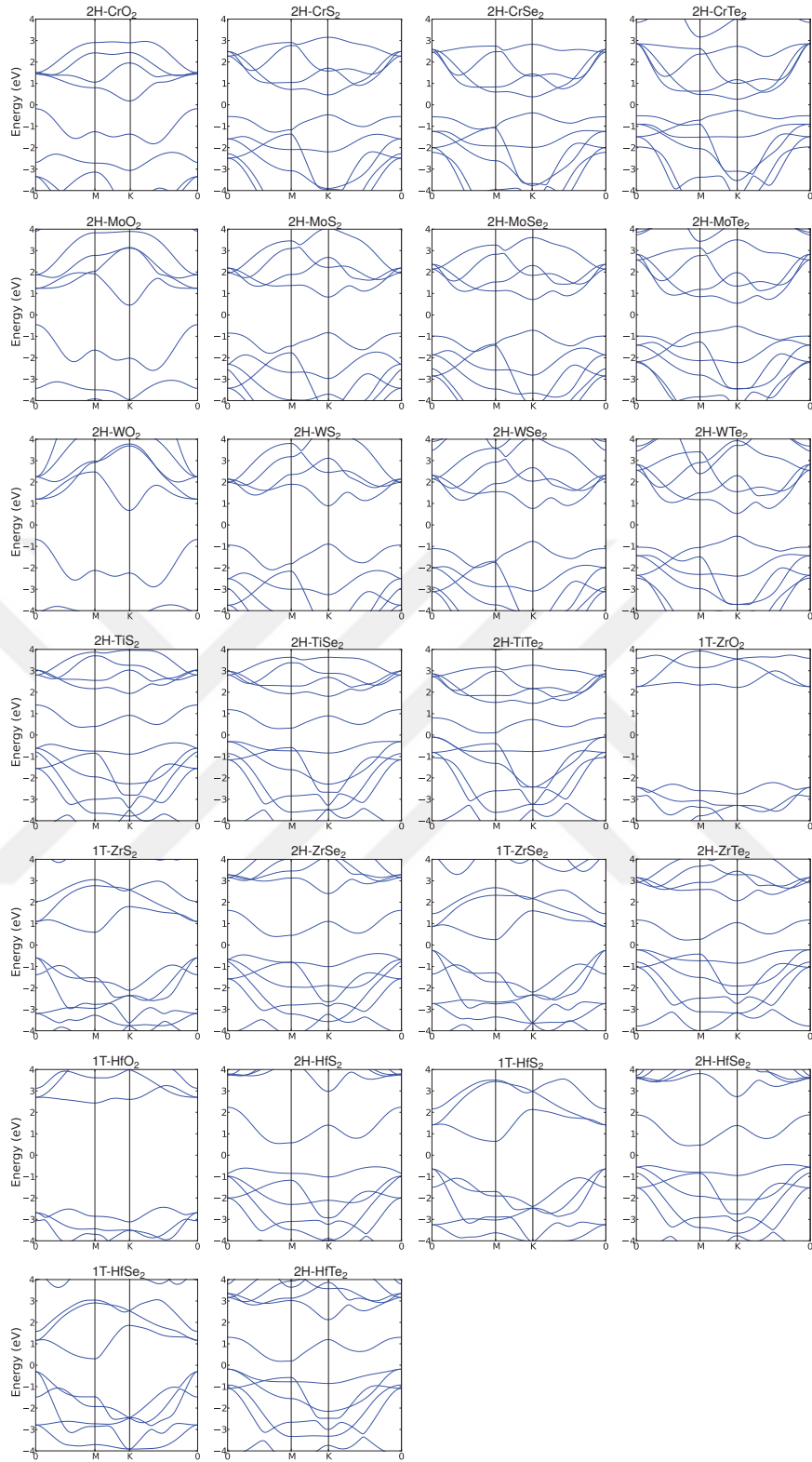


Figure 3.2. Electronic band diagrams of investigated TMDs and TMOs according to PBE results.

for the 1T-phase. That is to say, 1T-phases of studied Zr and Hf based compounds are energetically more stable, in agreement with previous studies (Gong et al. (2013); Tsipas et al. (2018); Aminalragia-Giamini et al. (2017); Mleczko et al. (2017); Yan et al. (2018)). In order to gain an understanding on bond characteristics, charge transfer calculations are conducted by using Bader method (Henkelman et al. (2006)). The percent ionic character (%*IC*) of metal and chalcogen/oxygen atoms can be calculated roughly as (Callister and Rethwisch (2013))

$$\%IC = \left\{ 1 - \exp \left[-0.25 (X_A - X_B)^2 \right] \right\} \times 100 \quad (3.2)$$

where X_A and X_B are electronegativities of the constituent atoms. According to Table 3.1, TMOs exhibit the highest ionic character in general, which is because of the largest charge transfer between the transition metal and the oxygen atoms. 1T-HfO₂, which has the highest cohesive energy and the widest electronic band gap shows the highest ionic character, whereas 2H-MoTe₂ possesses fractional covalent character.

Electronic band diagrams of the investigated structures are plotted Fig.3.2. The 2H-phases of group-VIB dichalcogenides are direct band gap semiconductors, whereas their oxides have indirect band gaps. Group-IVB dichalcogenides and oxides are all indirect semiconductors. Electronic band gaps ranging between 0.19 eV and 4.87 eV are obtained with PBE functionals. Hybrid functional (HSE06) calculations are performed with 0.25 exact Hartree-Fock, 0.75 PBE exchange mixing and the screening parameter of 0.2 Å⁻¹. Moreover, HSE06 is adopted to materials which have a E_g^{PBE} less than 0.5 eV. This has two main reasons. First, the correction to the band gap is more if the material has a narrow gap. Second, if E_g^{PBE} is large enough, the HSE06 correction does not affect the TE performance of the materials substantially because the band dispersions are less affected. When the band gap of a structure is less than $10k_B T$, simultaneous contribution from the holes in the valence band and electrons in the conduction band suppresses the Seebeck coefficient (Gerald Mahan (1997); Sofu and Mahan (1994); R. P. CHASMAR (1959); G.S. Nolas (2001); Dehkordi et al. (2015)). The effect of hybrid functionals on electronic transport and thermoelectric properties will be discussed in more detail later. The electronic band diagrams of 2H-CrO₂, 2H-TiTe₂, 2H-ZrTe₂ and 2H-HfTe₂ within PBE+HSE06 functionals are presented in Fig. 3.3. Band gap values are increased to 0.90, 0.97, 1.05 and 0.93 eV for CrO₂, TiTe₂, ZrTe₂ and HfTe₂ respectively.

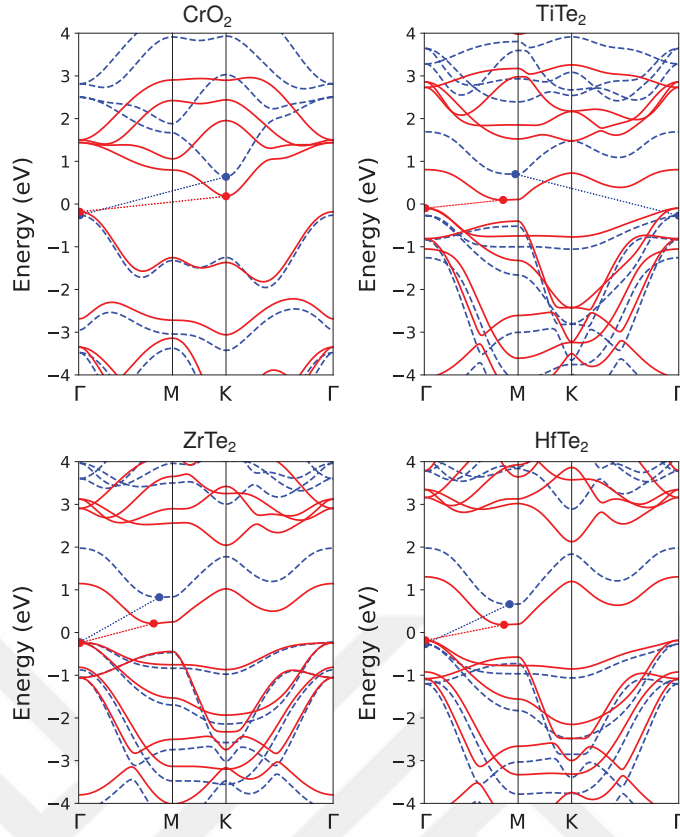


Figure 3.3. Calculated electronic band structures of selected 2H-MX₂ compounds; CrO₂, TiTe₂, ZrTe₂, HfTe₂ based on PBE (red solid line) and PBE+HSE (blue dashed line) functional. Fermi level is set to zero for all subfigures.

3.2. Vibrational Properties

It is necessary to check whether imaginary or negative frequencies exist in phonon dispersions to check the dynamical stabilities of the structures. We note that dynamical stability is a necessary condition but not conclusive for experimental realization. When both 2H- and 1T- phases of MX₂ monolayers are considered, 30 structures are found to be dynamically stable. Four of these structures are excluded in this study as they are either metallic or semimetallic. Phonon spectra of the remaining 26 structures are given in Fig. 3.4. The inter-atomic force constants (IFCs) are obtained by employing density functional perturbation theory (DFPT) (Baroni et al. (2001)). Phonon band structure and heat capacity calculations are performed by using the PHONOPY package (Togo and Tanaka (2015)). A cautionary note is in order here. Smearing is a computational tool that smoothens the Fermi distribution function around the Fermi energy. It is a necessary

ingredient in DFT calculations. Even graphene can be found dynamically unstable if appropriate smearing is not used. There does not exist a recipe for determining the smearing method or value. There are a few methods to implement smearing, most of them without a clear physical meaning. Fermi-Dirac smearing, on the other hand, is interpreted as electronic temperature. Being only applied on electrons and not on ions, it should be not confused with real temperature. Still, Fermi-Dirac smearing is used to identify temperature dependent stabilization in certain cases (Singh et al. (2017); Duong et al. (2015); Wei et al. (2017)). In this work, we implement Fermi-Dirac smearing and scan possible smearing values systematically.

For lower values of smearing ($\sigma=0.05$ eV) 2H-TiS₂, 2H-ZrSe₂ and 2H-HfS₂ out-of-plane ZA mode possess negative frequencies around the high symmetry points, whereas 2H-HfSe₂ has negative frequencies only around K-point. When the smearing is increased ($\sigma=0.4$ for 2H-HfSe₂ and $\sigma=0.5$ for 2H-TiS₂, 2H-ZrSe₂, 2H-HfS₂) all phonons frequencies are found positive. These σ values are in the same range with those used in the literature (Singh et al. (2017); Chen et al. (2018); Yan et al. (2015)).

The phonon band gap, which separates the acoustic modes from the six optical branches, decrease with decreasing mass difference between the constituent elements of MX₂ compounds. The acoustic bandwidths become narrower with increasing average mass, whereas all bands are pushed towards lower frequencies with increasing total mass of the compounds. In previous studies, in which phonon-phonon scattering was taken into account, the scatterings were limited when a band gap is present. Therefore absence of a phonon band gap was found help to reduce lattice thermal conductivity. Conversely, in the ballistic regime, the presence of a phonon band gap reduces lattice thermal conductivity, simply because there is no transmission within gap. Briefly, both a wide phonon band gap and reduced phonon frequencies decrease thermal conductance and enhances the TE performance. Thermal conductance of the investigated TMD/TMOs at various temperatures are listed in Table 4.3. 2H-CrO₂ is composed of the lightest atoms in the group, hence has the largest phonon thermal conductance at all temperatures. As temperature increases thermal conductance of CrO₂ increases considerably. A similar trend appears for all the TMOs, which is associated with the relatively higher ω_{\max} values, because of oxygen being the lightest element in group VIA.

In a previous study, which investigated the thermal conductivities of 2H group-VIB TMD family by using Boltzman Transport Equation (Zhang et al. (2017)), it was found that the thermal conductivities of sulfides (MS₂) and selenides (MSe₂) increase as M changes from Cr to Mo, and from Mo to W, due to the rapid increase in the phonon relaxation

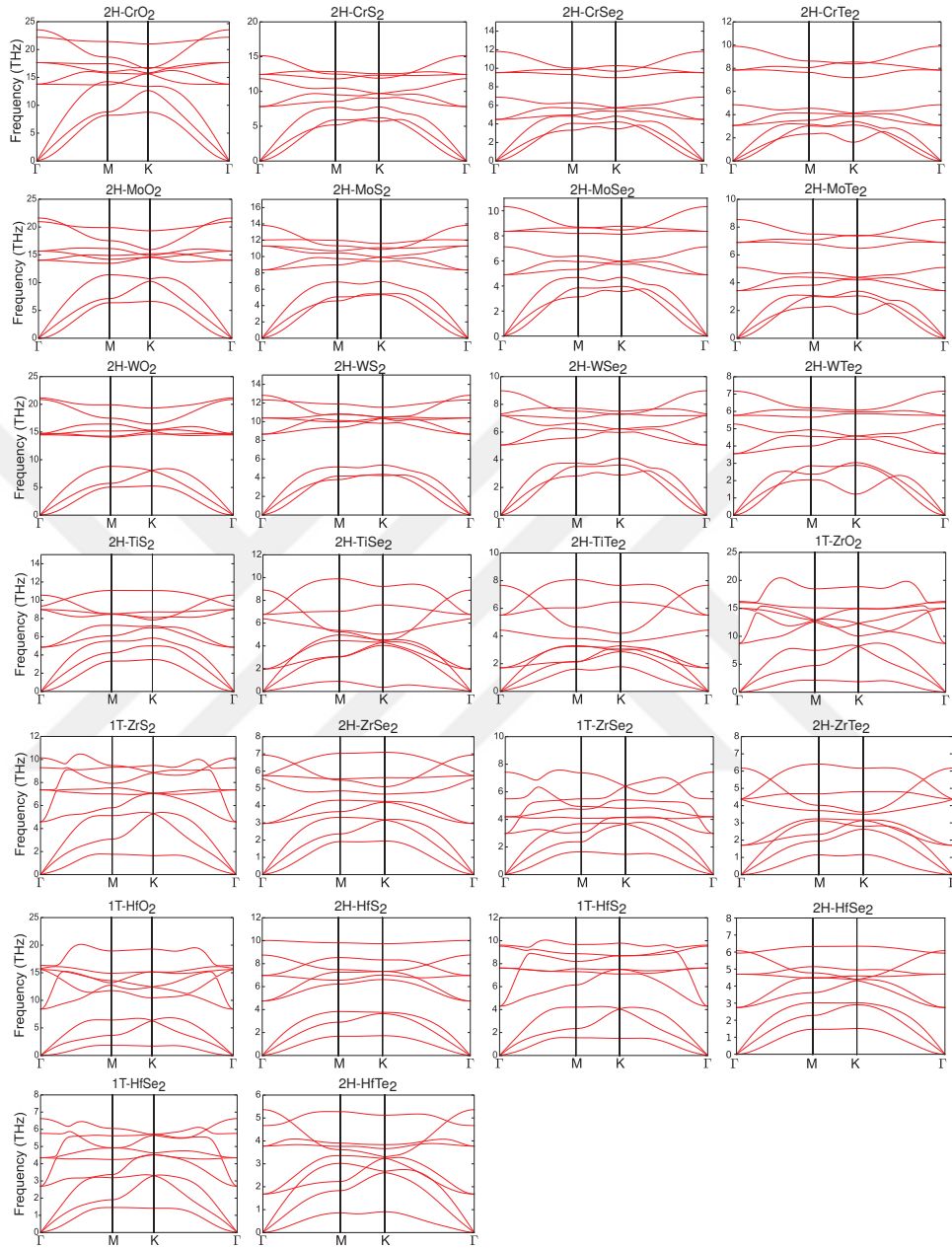


Figure 3.4. Phonon dispersion relations of investigated TMDs and TMOs.

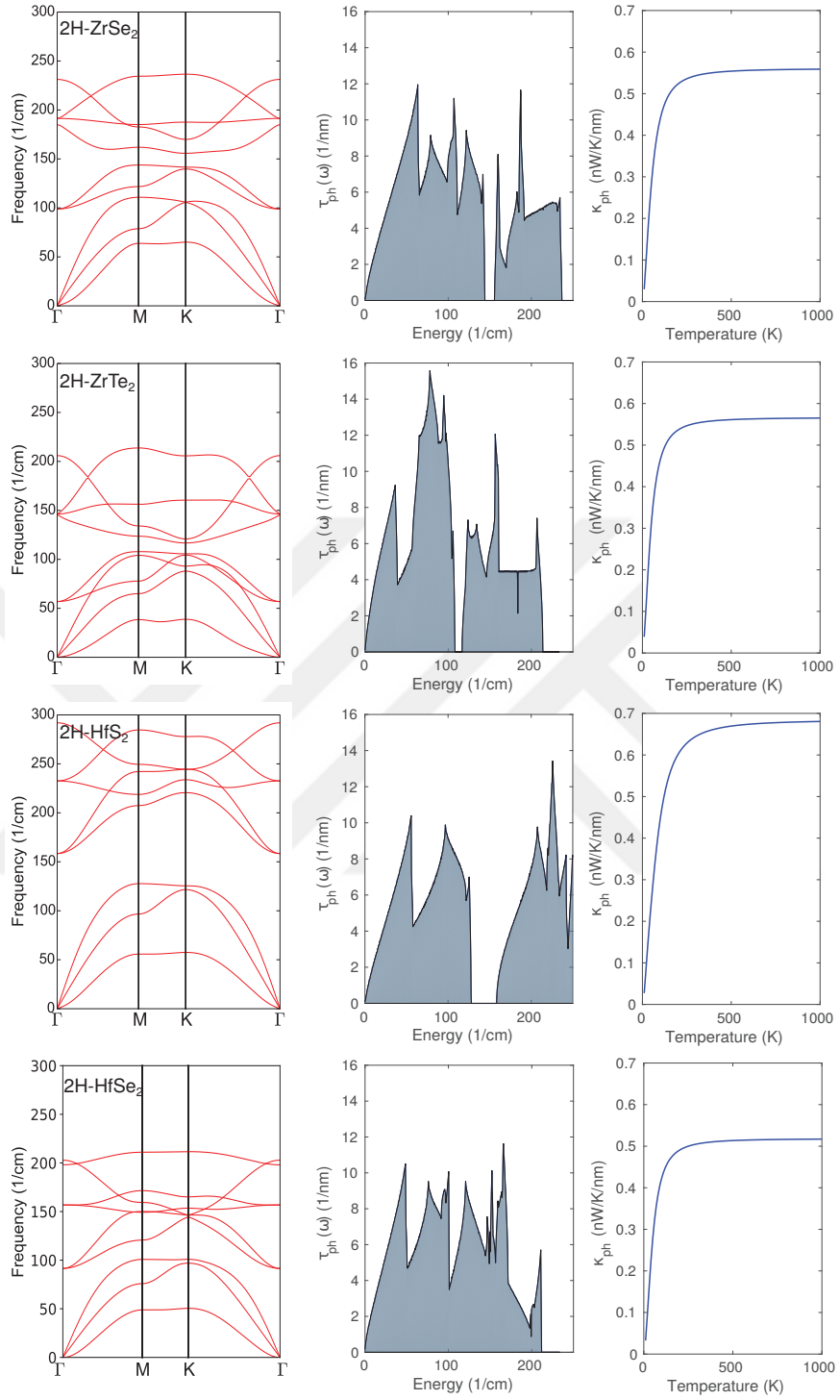


Figure 3.5. Phonon dispersion, phonon transmission spectrum and thermal conductance per length vs temperature of ZrSe₂, ZrTe₂, HfS₂ and HfSe₂ are shown respectively.

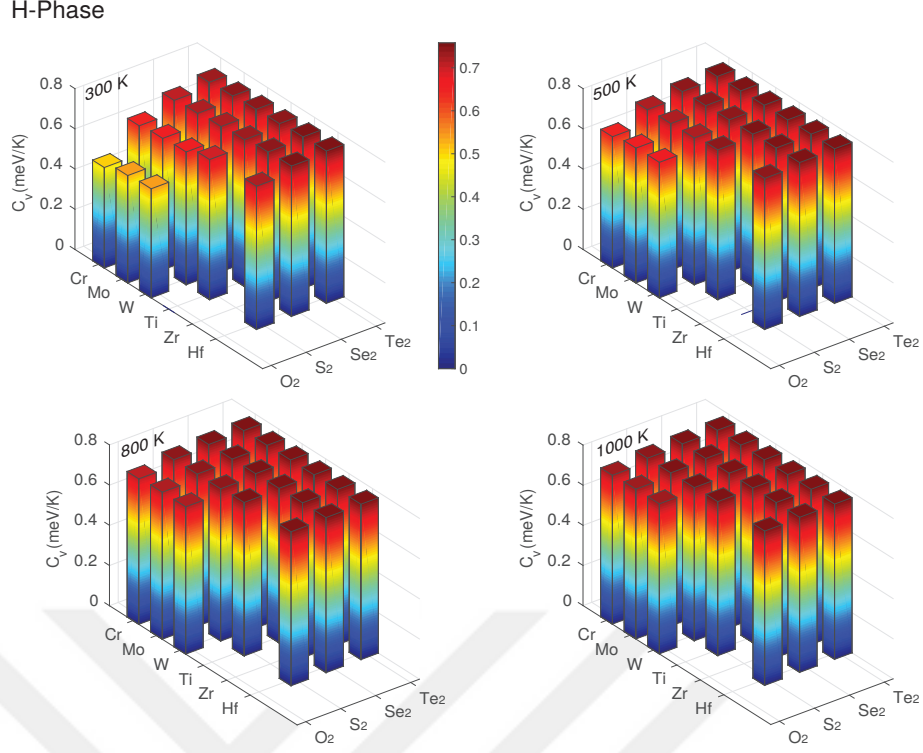


Figure 3.6. Heat capacities at various temperatures from 300K to 1000 K are shown for the semiconducting compounds in the 2H-phase.

time. In contrast to this, we find that κ_{ph} decreases as M changes from Cr to Mo to W at the ballistic limit, because of increasing atomic masses. This inverse behaviour is validated with the calculation of correlation between average atomic mass of the unitcell and phonon thermal conductance, where %80, %78 and %77 inverse correlations are found for 300 K, 500 K and 800 K respectively. In addition, it is found that correlation between m and κ_{ph} does not change at even higher temperatures. We also note that, in a recent theoretical study the ballistic thermal conductance value of 1H-MoS₂ was reported as 1.06 nW/K for a sample having a width of 1.27 nm (Cai et al. (2014)). The corresponding thermal conductance per width value (0.84 nW K⁻¹ nm⁻¹) is considerably less than our present result (1.03 nW K⁻¹ nm⁻¹). The disagreement is because we employ a fine sampling of the k-points in the transmission spectrum, whereas Cai *et al.* uses only the Γ point. Hence they find a stepwise transmission spectrum like in a one-dimensional system, which overestimates the contributions from low energies.

Table 3.2. Thermal conductance per length which is perpendicular to the transport direction for various temperatures.

MX_2	Phase	κ_{ph} (nW/K/nm)		
		300K	500K	800K
CrO ₂	2H	2.09	2.49	2.66
CrS ₂	2H	1.24	1.34	1.37
CrSe ₂	2H	0.83	0.87	0.88
CrTe ₂	2H	0.60	0.62	0.63
MoO ₂	2H	1.63	1.89	2.00
MoS ₂	2H	1.03	1.10	1.13
MoSe ₂	2H	0.72	0.75	0.76
MoTe ₂	2H	0.54	0.55	0.55
WO ₂	2H	1.29	1.48	1.56
WS ₂	2H	0.83	0.89	0.91
WSe ₂	2H	0.66	0.68	0.68
WTe ₂	2H	0.50	0.51	0.51
TiS ₂	2H	0.95	1.00	1.02
TiSe ₂	2H	0.95	0.99	1.00
TiTe ₂	2H	0.70	0.72	0.73
ZrO ₂	1T	1.45	1.71	1.81
ZrS ₂	1T	0.83	0.87	0.89
ZrSe ₂	2H	0.54	0.55	0.56
	1T	0.71	0.72	0.73
ZrTe ₂	2H	0.55	0.56	0.56
HfO ₂	1T	1.28	1.50	1.60
HfS ₂	2H	0.65	0.67	0.68
	1T	0.71	0.74	0.75
HfSe ₂	2H	0.51	0.51	0.52
	1T	0.59	0.61	0.61
HfTe ₂	2H	0.48	0.49	0.49

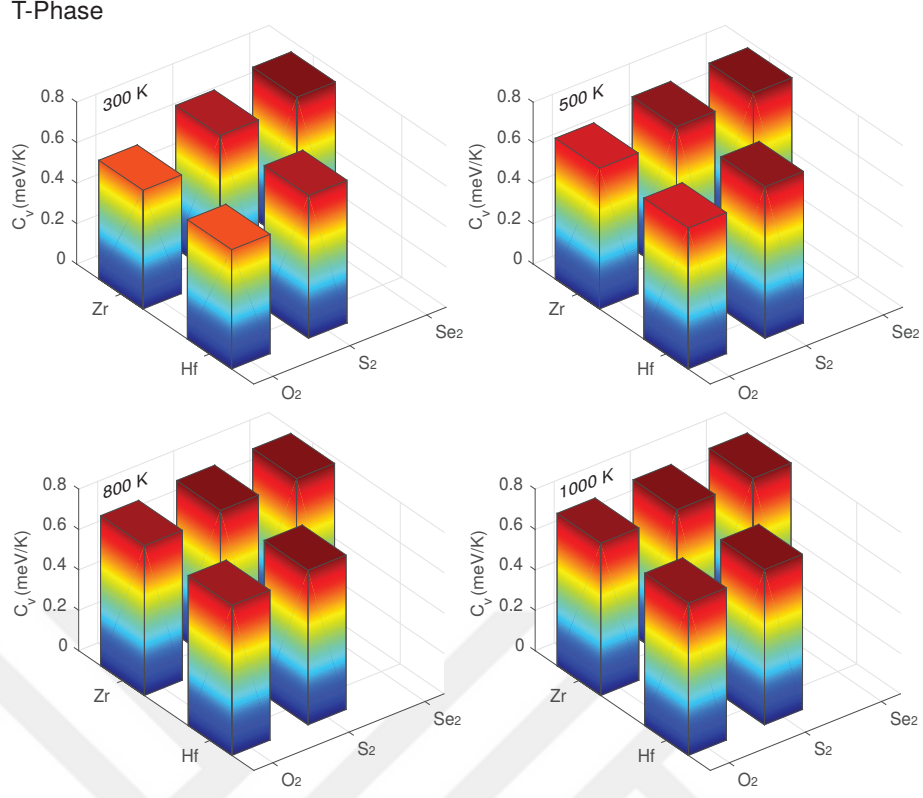


Figure 3.7. Heat capacities at various temperatures from 300K to 1000 K are shown for the semiconducting compounds in the 1T-phase.

The vibrational heat capacity at constant volume is calculated using

$$C_v = k_B \int d\omega \rho(\omega) p(\omega, T), \quad (3.2)$$

where ρ is the phonon density of states, $p(x) = -x^2 \partial f_{BE} / \partial x$, $f_{BE} = 1/(e^x - 1)$ being the Bose-Einstein distribution function, and $x = \hbar\omega/k_B T$. In Fig. 3.6(a) and (b) the vibrational heat capacities are plotted at $T = 300$ K, 500 K, 800 K and 1000 K. At lower temperatures, the heat capacity is dominated by low frequency modes which possess low group velocity and larger phonon density of states. Therefore, heavier compounds, like Hf and Zr based structures, have higher heat capacities at 300 K. At increased temperatures, the differences in the C_v tend to decrease. At 1000K, the function $p(x)$ is almost constant and equal to unity in the entire spectrum. The heat capacities approach to the classical limit, which is proportional to the number of modes per unit cell.

Table 3.3. *p*- and *n*-type Seebeck coefficient (*S*), power factor (*P*) and thermoelectric figure of merit (*ZT*) at different temperatures based on PBE calculations.

MX ₂	Phase	<i>S</i> (10 ⁻⁴ V/K)			<i>P</i> (10 ⁻³ nW/K ² nm)			<i>ZT</i>		
		300 K	500 K	800 K	300 K	500 K	800 K	300 K	500 K	800 K
CrO ₂ ¹	2H	2.01/-1.86	1.99/-1.93	1.49/-1.80	0.69/1.15	0.89/1.52	0.98/1.92	0.10/0.15	0.17/0.27	0.23/0.44
CrS ₂	2H	2.04/-1.99	2.20/-2.23	2.47/-2.43	1.57/1.20	2.58/1.66	3.50/2.41	0.33/0.27	0.74/0.53	1.40/1.02
CrSe ₂	2H	2.13/-1.97	2.35/-2.39	2.65/-2.66	1.30/1.31	1.87/1.75	2.74/2.50	0.41/0.40	0.83/0.80	1.59/1.49
CrTe ₂	2H	2.08/-2.24	2.48/-2.40	2.46/-2.43	1.35/1.26	1.82/1.77	2.76/2.69	0.55/0.54	1.08/1.05	1.70/1.59
MoO ₂	2H	1.92/-1.94	1.95/-1.97	2.02/-2.15	0.51/0.82	0.66/1.06	0.84/1.35	0.09/0.14	0.17/0.26	0.30/0.47
MoS ₂	2H	2.05/-2.07	2.37/-2.13	2.52/-2.52	1.89/0.81	2.31/1.17	2.88/1.98	0.47/0.22	0.86/0.45	1.46/0.97
MoSe ₂	2H	2.08/-2.00	2.27/-2.45	2.57/-2.79	1.02/0.95	1.38/1.68	1.95/3.17	0.38/0.35	0.74/0.81	1.38/1.91
MoTe ₂	2H	2.18/-2.11	2.36/-2.48	2.71/-2.99	1.06/0.97	1.46/1.62	1.98/2.66	0.51/0.46	1.00/1.00	1.85/2.21
WO ₂	2H	2.01/-1.88	2.01/-2.10	2.06/-2.14	0.50/0.75	0.65/0.96	0.82/1.25	0.11/0.16	0.21/0.30	0.37/0.54
WS ₂	2H	2.08/-2.00	2.28/-2.12	2.58/-2.62	1.41/0.67	1.95/1.00	2.38/1.90	0.43/0.22	0.86/0.46	1.50/1.08
WSe ₂	2H	2.06/-1.97	2.24/-2.43	2.51/-2.85	0.83/0.86	1.09/1.93	1.47/3.43	0.34/0.33	0.67/0.92	1.21/2.18
WTe ₂	2H	1.99/-2.07	2.37/-2.33	2.59/-2.82	0.82/0.68	1.06/0.98	1.42/1.72	0.42/0.36	0.83/0.74	1.49/1.57
TiS ₂	2H	2.42/-2.24	2.47/-2.61	2.52/-2.52	3.74/4.43	3.98/4.84	3.98/5.29	0.98/1.05	1.55/1.79	2.14/2.66
TiSe ₂	2H	2.19/-2.39	2.38/-2.54	2.33/-2.39	3.33/3.43	3.68/3.99	4.31/4.64	0.86/0.90	1.38/1.51	1.81/2.09
TiTe ₂ ¹	2H	1.94/-2.16	1.26/-1.64	1.11/-1.21	1.19/2.78	1.39/3.06	2.65/2.86	0.40/0.90	0.38/0.87	0.38/0.55
ZrO ₂	1T	2.20/-2.01	2.37/-2.34	2.47/-2.58	5.12/3.35	5.56/5.17	5.65/6.25	0.86/0.52	1.28/1.08	1.87/1.94
ZrS ₂	1T	2.02/-2.19	2.21/-2.30	2.45/-2.69	0.67/1.85	0.88/2.40	1.31/2.78	0.23/0.57	0.44/1.04	0.87/1.75
ZrSe ₂	2H	2.38/-2.43	2.63/-2.76	2.75/-2.87	3.36/3.59	3.34/4.00	3.29/4.21	1.41/1.42	2.19/2.41	2.96/3.61
ZrSe ₂	1T	1.93/-2.09	2.13/-2.40	1.90/-2.05	0.56/1.80	0.72/2.22	0.91/2.71	0.22/0.63	0.43/1.16	0.65/1.76
ZrTe ₂ ¹	2H	2.26/-2.35	2.65/-2.50	2.11/-2.02	2.56/2.82	2.84/3.21	4.10/3.85	1.06/1.18	1.73/1.88	1.58/1.67
HfO ₂	1T	2.33/-2.28	2.45/-2.45	2.53/-2.63	4.80/2.67	5.28/3.92	5.43/5.30	0.92/0.54	1.38/0.99	2.00/1.80
HfS ₂	2H	2.38/-2.26	2.62/-2.62	2.70/-2.83	3.85/3.33	3.78/3.59	3.59/3.88	1.38/1.17	2.11/1.89	3.03/2.92
HfS ₂	1T	2.05/-2.32	2.21/-2.36	2.38/-2.71	0.66/1.87	0.85/2.39	1.16/2.69	0.26/0.67	0.50/1.19	0.92/1.96
HfSe ₂	2H	2.55/-2.47	2.73/-2.75	2.83/-2.91	3.36/2.74	3.35/2.91	3.40/3.19	1.57/1.28	2.36/2.04	3.30/3.04
HfSe ₂	1T	1.92/-2.20	2.13/-2.46	2.12/-2.65	0.56/1.84	0.73/2.23	0.92/2.61	0.26/0.75	0.51/1.35	0.84/2.11
HfTe ₂ ¹	2H	2.29/-2.31	2.24/-2.44	1.74/-1.86	1.05/2.41	1.52/2.64	2.48/3.09	0.56/1.17	1.00/1.75	0.91/1.34

3.3. Thermoelectric Properties

According to the Mott formula (Cutler and Mott (1969); Gunst et al. (2011); Guttman et al. (1995))

$$S(T, \mu) \approx \frac{\pi^2 k_B^2 T}{3e} \left. \frac{d \ln \tau(E)}{dE} \right|_{\mu}, \quad (3.2)$$

the logarithmic derivative of the electronic transmission determines the Seebeck coefficient at low temperatures. Namely, the abrupt changes in the transmission spectrum gives rise to large Seebeck coefficient and power factor. The structures studied in this work agree with this rule of thumb. The thermoelectric coefficients, *S*, *P* and *ZT* for various temperatures are tabulated in Table 3.3. The chemical potential (μ) is chosen around the band edges where *ZT* is maximized. The difference between μ at the valence band edge (conduction band edge) and the μ where *p*-type *ZT* (*n*-type *ZT*) is maximized is crucial for determining the optimal doping levels of the semiconductor (see Table 3.4).

One observes that most of the 2H group-VIB TMD/TMOs have relatively low *ZT* values compared to the 2H group-IVB TMD/TMOs. Notably, oxide compounds from

group-VIB show considerably weak TE performance due to their low atomic masses and hence high κ_{ph} . While p -type ZT values of the group-VIB TMOs reach a maximum value around 0.11 at room temperature, the corresponding values for n -type ZT can be as high as 0.16. There are various theoretical studies on the TE properties of MX_2 ($M = Mo, W$; $X = S, Se$) monolayers. In a previous work, n -type ZT of the most studied MoS_2 monolayer was predicted 0.04 by using Boltzmann equation and equilibrium molecular dynamics (EMD) simulations (Jin et al. (2015)). Wickramaratne et al., obtained different n -type ZT values (0.87/1.35) by adopting layer thickness dependent and constant κ_{ph} values in diffusive regime calculations. In another work, reported ZT values are overestimated compared to our findings for well-studied MoS_2 , $MoSe_2$, WS_2 and WSe_2 in the frame of ballistic transport (Chen et al. (2015)). In addition, previously reported p - and n type ZT values (0.58/0.25) in ballistic regime are consistent with our results (0.47/0.22) (Huang et al. (2013)). Also, there is an agreement on the results of Huang et al. that, p -type ZT of MoS_2 at room temperature and n -type ZT of WSe_2 at high temperatures are found to be higher than those of the $MoSe_2$ and WS_2 (Huang et al. (2013)).

Among all investigated compounds, $ZrSe_2$, HfS_2 and $HfSe_2$ are dynamically stable in both 2H- and 1T-phases. We predict substantial differences in their TE performances. Both n -type and p -type ZT values of the 2H-phases are much larger than those of the 1T-phase, and κ_{ph} of the 1T-phases are always slightly higher than the 2H-phases (see Table 4.3). The underlying reason lies mostly in their electronic band structures. The frontier bands in the 2H-phase are less dispersive than in the 1T-phase. The valence band maximum is almost flat, which leads to sharp changes in the DOS and the electronic transmission spectrum and give rise to enhanced S , P , and ZT . As a result, the p -type ZT values of the 2H-phases are 5 to 6 times higher than those of the 1T-phases. In the n -type ZT , the difference is not as dramatic as in the p -type ZT , but those of 2H-phases are considerably larger again. 1T phases of $ZrSe_2$, $HfSe_2$ and HfS_2 were previously predicted to have promising ZT values, when phonon scatterings are taken into account (Ding et al. (2016); Qin et al. (2017)).

In order to quantify the role of κ_{ph} on ZT , we study their correlation from the available data. The p -type ZT for 2H compounds is inversely correlated with κ_{ph} as 55%, 60% and 59% at 300 K, 500 K and 800 K, respectively. On the other hand, inverse correlation between n -type ZT and κ_{ph} is slightly larger than that of p -type ZT . Inverse correlation values of 57%, 62% and 61% are obtained for the same temperatures. These illustrate the role of κ_{ph} in determining the TE performance of the crystals considered.

The 2H-phases of $ZrSe_2$, $ZrTe_2$, HfS_2 and $HfSe_2$ provide ZT values larger than 1

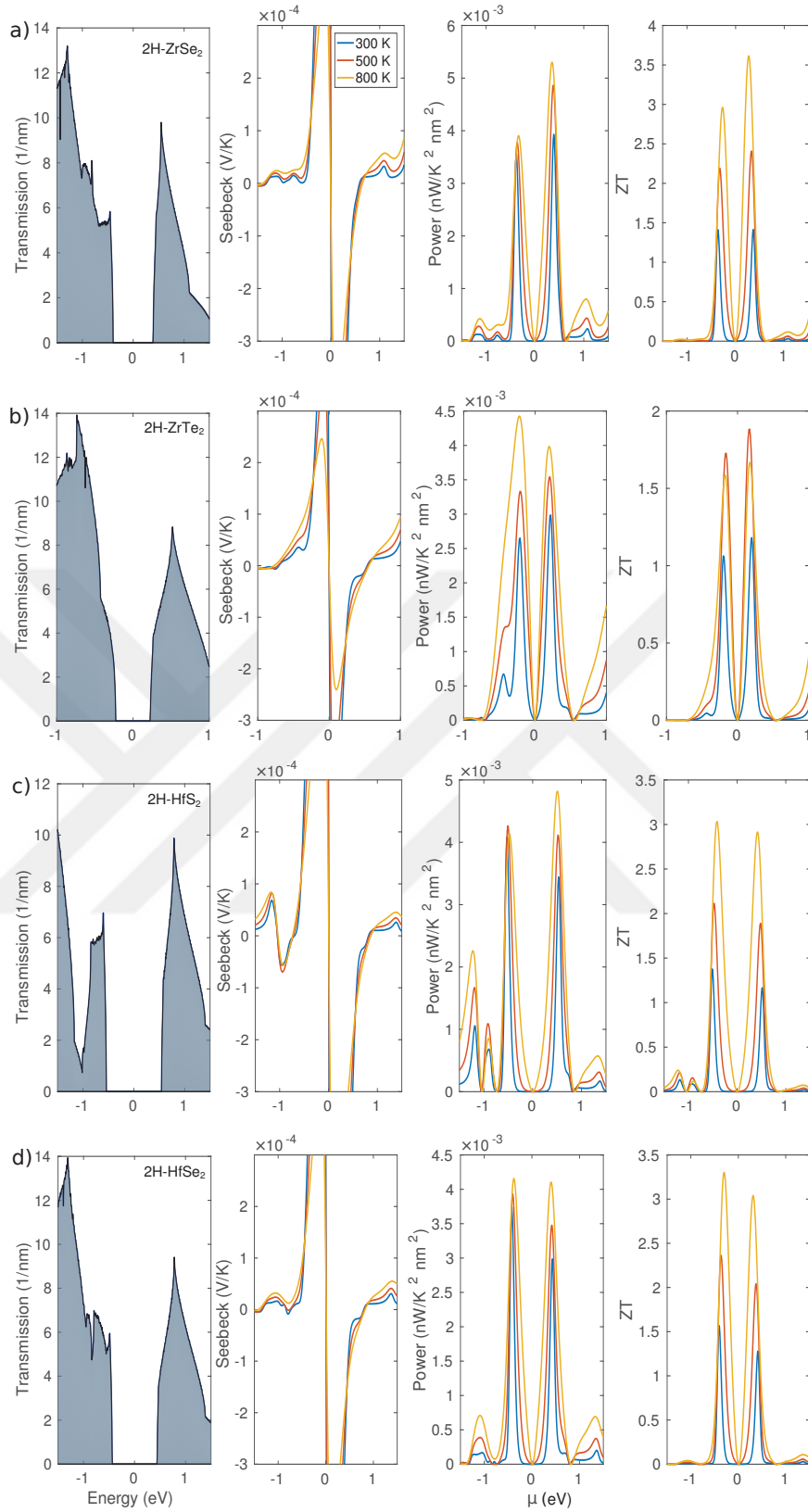


Figure 3.8. Electronic transmission, Seebeck coefficient, power factor and thermoelectric figure of merit are plotted around the Fermi level for 2H-ZrSe₂, 2H-ZrTe₂, 2H-HfS₂ and 2H-HfSe₂.

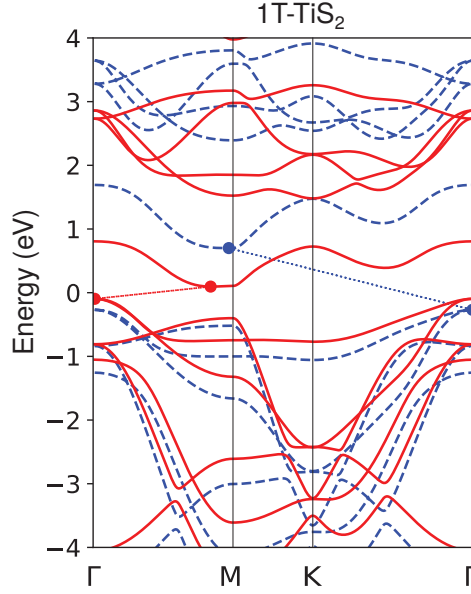


Figure 3.9. Electronic band structure of 1T-TiS₂ with PBE (solid red) and hybrid HSE06 (dashed blue) functionals. Transition from semimetallic to semiconducting phase is occurred with hybrid functional.

for both n - and p -type carriers at room temperature. The electronic transmission, Seebeck coefficient, power factor and TE figure of merit of these compounds are presented in Fig. 3.8. Although 2H-ZrSe₂ and 2H-ZrTe₂ have almost the same thermal conductance values, ZrTe₂ has the lowest ZT compared to other promising compounds due to relatively smooth transmission spectra at the valence band edge. It is also observed that PBE results yield a decreasing ZT for ZrTe₂ above 500 K. This stems from the fact that the band gap of ZrTe₂ as predicted from PBE is not sufficient to support an efficient TE response at high temperatures. We use hybrid functionals to correct the calculated band gap, which will be discussed separately below. Abrupt changes in the transmission spectra are observed at the valence band edges of ZrSe₂, HfS₂, and HfSe₂ (see Fig. 3.8). Although κ_{ph} of 2H-HfTe₂ is lower than that of 2H-HfSe₂, its p -type ZT is much lower than that of 2H-HfSe₂, which is found to have the highest p -type ZT value (1.57) at room temperature. The lower ZT value of 2H-HfTe₂ is because of its electronic transmission being smoother than that of 2H-HfSe₂. In the case of n -type ZT , in addition to these four TMDs, for 2H-HfTe₂ and 2H-TiS₂, it exceeds 1 at room temperature. It is worth mentioning that, a remarkably high p -type power factor is achieved for the 1T-ZrO₂ and 1T-HfO₂ but their lattice thermal conductances are higher than those of 2H-ZrSe₂, 2H-ZrTe₂, 2H-HfS₂ and 2H-HfSe₂ by

about a factor of 2 or 3, thus their ZT values remain under 1 at 300 K. In principle, TE response of these oxides can be enhanced by reducing κ_{ph} with phonon engineering.

Seebeck coefficient is reduced with simultaneous contribution of p - and n -type carriers. Accordingly, obtaining accurate S , PF and ZT values will mostly depend on electronic band gap of material, especially at higher temperatures. If the band gap of the material is smaller than about $10k_B T$, S is suppressed with increasing temperature as in the cases of 2H-CrO₂, 2H-HfTe₂, 2H-TiTe₂ and 2H-ZrTe₂. The E_g^{PBE} is 0.36 eV (0.45 eV) for 2H-HfTe₂ (2H-ZrTe₂), and S is suppressed when temperature is above 300 K (500 K). Suppression of S reduces ZT when T is above 500 K for 2H-HfTe₂, because the increase in G compensates the decrease in S at lower temperatures. For 2H-CrO₂, a similar trend in S is observed, however ZT is not suppressed at higher temperatures because G increases with T . 2H-TiTe₂ has the narrowest E_g^{HSE} (0.19 eV) among the investigated TMDs. Therefore, the decrease in S and ZT appear above room temperature. $\tau_{el}(E)$, S , PF and ZT calculated from hybrid-functional-corrected band gaps are demonstrated in the Fig. 3.10 Band gap correction using hybrid functionals results in better ZT values for these MX₂ compounds as seen in Table 3.5.

Besides the semiconducting TMD/TMOs, TE properties of semimetallic 1T-TiS₂ is also investigated. 1T-TiS₂ is more stable with a $E_{coh}=5.31$ eV, which is higher than its 2H-phase for about 0.14 eV (Xu et al. (2015)). HSE06 correction exhibits a transition from semimetallic to semiconducting behaviour as shown in Fig. 3.9 with a band gap of 0.62 eV, in agreement with previous results (Samad et al. (2017)). It is clearly seen that 1T-TiS₂ does not achieve a high value of p -type ZT , but n -type ZT exceeds 1 when temperature reaches 800 K (see Table 3.5 and Fig. 3.10).

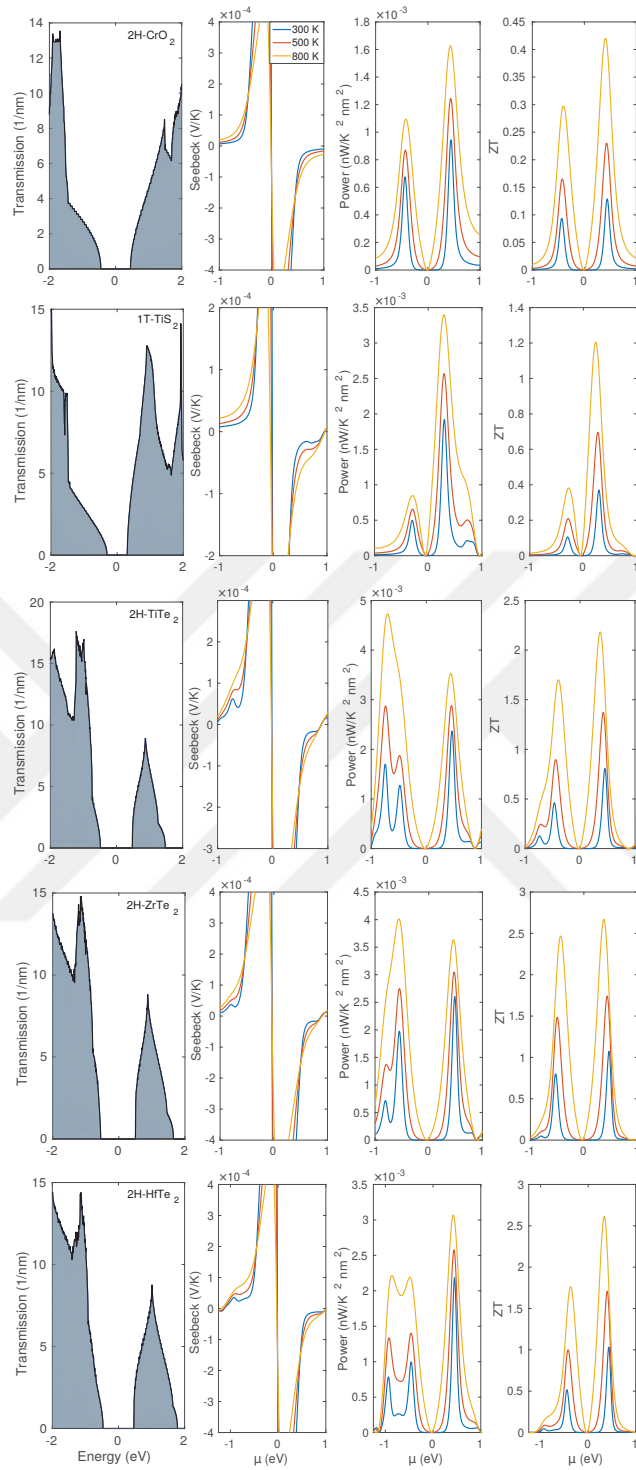


Figure 3.10. Electronic transport and thermoelectric properties are performed based on HSE06+PBE functional for these narrow gap 2H phases of CrO₂, TiTe₂, ZrTe₂, HfTe₂ and semimetallic 1T-TiS₂ compounds.

Table 3.4. Difference between chemical potential μ where p-type ZT_{max} (n-type ZT_{max}) is obtained and valence band edge value (conduction band edge) in meV.

MX ₂	Type	ϵ_p (meV)			ϵ_n (meV)		
		300 K	500 K	800 K	300 K	500 K	800 K
CrO ₂	2H	-15	-25	5	5	15	15
CrS ₂	2H	-5	-15	-55	10	30	60
CrSe ₂	2H	-15	-35	-75	10	40	80
CrTe ₂	2H	-30	-60	-80	20	40	60
MoO ₂	2H	-10	-20	-40	10	20	50
MoS ₂	2H	-10	-40	-80	10	20	50
MoSe ₂	2H	-15	-35	-75	10	30	60
MoTe ₂	2H	-15	-35	-85	15	35	85
WO ₂	2H	-10	-20	-40	5	25	45
WS ₂	2H	-5	-25	-75	10	20	50
WSe ₂	2H	-15	-35	-75	5	15	55
WTe ₂	2H	-10	-40	-80	15	35	75
TiS ₂	2H	-30	-60	-110	20	60	100
TiSe ₂	2H	-30	-60	-90	30	60	90
TiTe ₂	2H	-10	30	130	25	15	-15
ZrO ₂	1T	-20	-50	-100	-5	15	65
ZrS ₂	1T	-10	-30	-60	20	40	100
ZrSe ₂	2H	-30	-70	-130	25	65	125
ZrSe ₂	1T	-10	-30	-30	15	45	85
ZrTe ₂	2H	-25	-65	-55	25	55	55
HfO ₂	1T	-25	-55	-105	20	40	80
HfS ₂	2H	-30	-70	-130	25	65	125
HfS ₂	1T	-15	-35	-65	25	45	105
HfSe ₂	2H	-35	-75	-135	30	70	130
HfSe ₂	1T	-10	-30	-50	20	50	100
HfTe ₂	2H	-20	-30	10	30	60	50

Table 3.5. *p*- and *n*-type ZT values at different temperatures based on the HSE06 calculations.

MX ₂	Phase	ZT (<i>p</i> -/ <i>n</i> -type)		
		300K	500K	800K
CrO ₂	2H	0.09/0.13	0.17/0.23	0.30/0.42
TiTe ₂	2H	0.47/0.81	0.90/1.37	1.70/2.18
ZrTe ₂	2H	0.80/1.08	1.49/1.74	2.47/2.67
HfTe ₂	2H	0.52/1.03	1.00/1.71	1.76/2.62
TiS ₂	1T	0.11/0.37	0.21/0.70	0.38/1.21

CHAPTER 4

BALLISTIC TRANSPORT AND THERMOELECTRIC PROPERTIES OF GROUP III-VI MONOCHALCOGENIDES

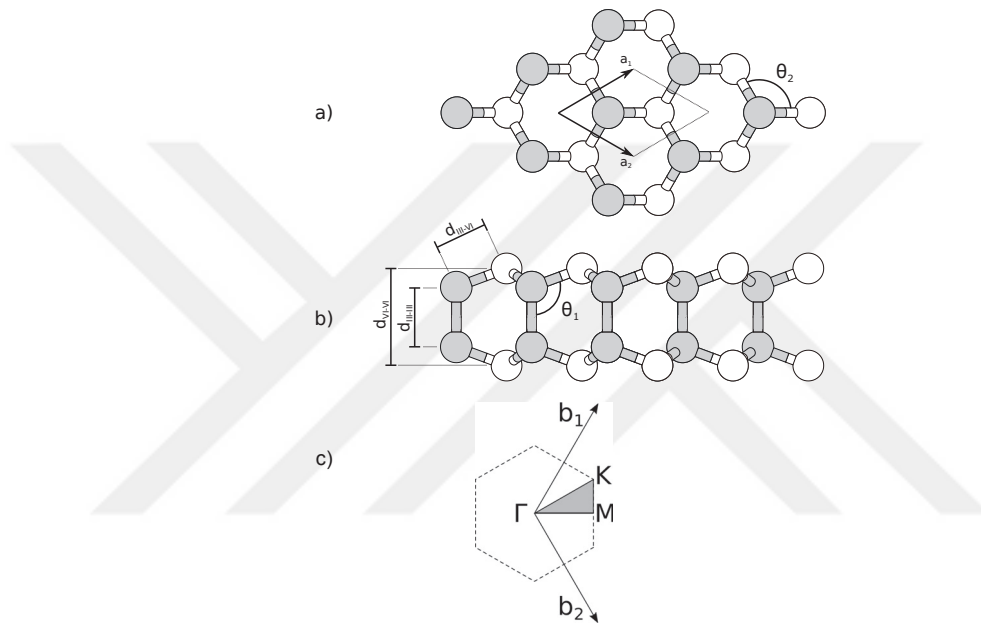


Figure 4.1. Atomic structure of group III-monochalcogenides from (a) top and (b) side view. (c) First Brillouin zone.

4.1. Structural and Electronic Properties

In this section, structural and electronic properties of group III-monochalcogenides are investigated in α -phase (Özdamar et al. (2018)) which exhibits $P\bar{6}m2$ crystal symmetry. The representative structure of the monolayer from top and side view can be seen in 4.1(a) and (b) respectively. Unit cell is composed of four atoms which are in the arrangement of X-M-M-X where M and X belongs to group III and group VI respectively. Calculated lattice constants, bond lengths and bond angles of 25 compounds are summarized in Table

4.1. In a recent theoretical study (Mortazavi and Rabczuk (2018)), structural properties and stability of boron monochalcogenides are investigated and Ab-Initio Molecular Dynamics (AIMD) simulations put forward that BS, BSe and BTe monolayers are not straggled up to 1500 K. Also, a phase transition from α -phase to β -phase ($P\bar{3}m1$) is not observed at high temperatures. Theoretical results indicate that α and β -phase of BS monolayer are thermally and dynamically stable as well as β -phase can be exfoliated from polycrystalline high-pressure phase which is transformed from rhombohedral BS (r-BS) (Fan et al. (2018); Cherednichenko et al. (2018)). Indium monochalcogenides are found to be dynamically stable and optimized geometrical parameters are consistent with our results (Zólyomi et al. (2014)). Our findings show a good agreement with previous theoretical studies (Demirci et al. (2017)). However, the TI and Po combinations have never been investigated before, it is not possible to make a comparison of their structural properties. For each compound, lattice constants and bond lengths d_{VI-VI} and d_{III-VI} are increasing as chalcogen atom going down along the group VI. Bond length between group III elements $d_{III-III}$ is found to decrease from oxygen to sulfur and then shows small change with respect to chalcogen atom. Depending on the atomic radius, BO has the smallest a and TIPo has the largest a .

It is found that, except for semi-metal TlO, all monolayers are indirect band gap semiconductors as depicted in Figure 4.3. Electronic band gap values vary in a wide range from 0.24 eV to 4.72 eV. This means that most group III-monochalcogenides can be thermoelectric candidates after determining their dynamical stability. InO, TlS, TlSe, TlTe, and TIPo possess narrow band gaps. In this case, coexistence of n-type and p-type carrier contributions from conduction and valence bands will reduce Seebeck voltage. It is well known that one type charge carrier is favourable for high S . Previous theoretical calculations reveal that for indirect band gap semiconductors, optimized band gap value should be at least $E_g \geq 10k_B T$ to avoid mixing charge carriers. In the case of the InO, TlS, TlSe, TlTe, and TIPo, band gap values based on PBE functional are not sufficient for elevated temperatures. Thus, HSE06 hybrid functional is applied to narrow gap materials to obtain correct TE coefficients. Remaining materials do not require widening of the band gap because their gaps are high enough to eliminate the possibility of charge carriers cancelling each other at high temperatures. The band diagrams of narrow gap structures and semi-metal TlO, calculated from the HSE06 hybrid functional, are shown in Figure 4.4. The resulting band gap values are 1.14 (InO), 0.44 (TlO), 1.16 (TlS), 0.94 (TlSe), 0.78 (TlTe) and 0.53 (TIPo) eV. Band gap of InO and TIPo is still inadequate to prevent concurrent contribution of different types of charge carriers at the HSE06 level for high temperatures. Beyond these structural and electronic properties, the most striking feature

is the quartic dispersion of the valence band which is also called "Mexican hat shaped" valence band. Figure 4.2 illustrates the schematic representation of the linear, quadratic and quartic band dispersion.

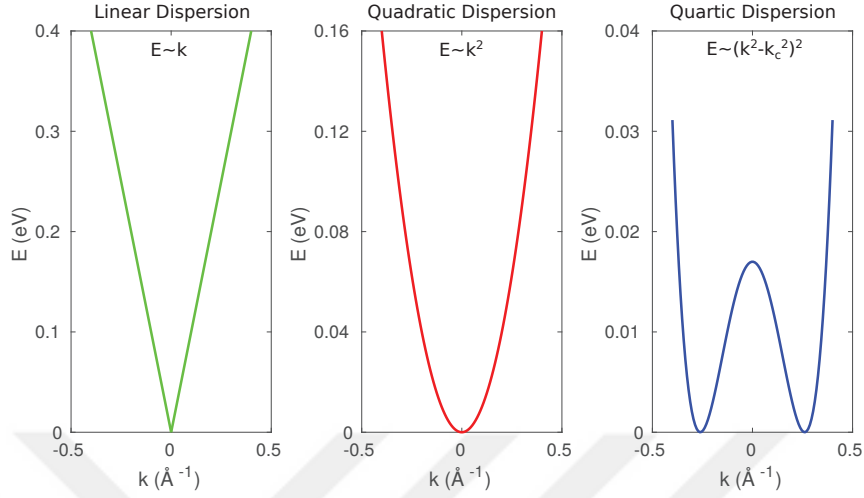


Figure 4.2. Linear, quadratic and quartic electronic band dispersion.

A total of 18 compounds have highest valence band that exhibit $E = E_v - \alpha(k^2 - k_c^2)^2$ energy-momentum relation around Γ point. Valence band edges form a closed curve around the Γ point. Critical wave vector k_c is an indication of how much the valence band fits MHS character. k_c and α parameters are given in Table. 4.2 for 18 compounds. Valence bands of GaTe, InTe, TlTe, InPo and TlPo are much closer to the pure quartic dispersion where $k_c = 0$ and $E = E_v - \alpha k^4$. In the case of BSe, BTe and BPo, MHS valence band moves downward and doubly degenerate valence bands become topmost valence bands. In this situation, dominant effect of the quartic dispersion on density of states, electronic transmission and thermoelectric coefficients is reduced. Multiple degenerate bands also have a constructive effect on TE properties results from increase in charge carrier concentration in transport window. However enhancement of S is more favourable. Additionally, extrema of the mexican valence band at the Γ point coincides with top of the multiple degenerate valence bands in AlPo, InPo and TlPo but they maintain MHS character as clearly seen from their electronic transmission spectrum at the valence band edge. In the case of GaPo, top of the degenerate bands and the dip of the MHS band overlaps. Step-like $\tau_{el}(E)$ behaviour is not conserved however, continuous variation of the dispersion of the band around Γ point does not constitute an adverse effect on S coefficient and thermoelectric efficient. GaO and InO does not exhibit MHS type band dispersion

because of the flattening of the highest valence band.

4.2. Phonon Dispersion Relations and Transmission Spectra

Figure 4.5 shows phonon band diagrams together with the phonon transmission spectra τ_{ph} of group III-VI compounds. Since the unitcell have four atoms, each monolayer exhibits three acoustic and nine optical branches. Absence of imaginary frequencies in the phonon dispersion curves, declare that all investigated structures are dynamically stable. Highest frequency of the overall branches gradually reduce from left to right with the increase in the mass of the chalcogen atom. Similarly, as the mass of the group-III atom is getting heavier, optical and acoustic bands are shifted towards low frequencies, specifically acoustic bands are confined in a narrow frequency range. Since, BO monolayer has the lightest average atomic mass in this family, vibrational frequencies of BO are higher compared to others. ω_{max} reaches 35 THz for BO monolayer. Also, it is noticed that optical modes which possess lowest and highest frequencies are well separated in all monolayers except BO as can be seen from its transmission spectrum. Downward shift of the acoustic modes to a narrower frequency range results in less dispersive acoustic modes and hence lower group velocity. Moreover, increasing bond length when moving down on a chalcogen atoms leads to weak bonding and hence less stiffened acoustic branches. In this respect, LA and TA modes of BO compound have notably higher velocity. In addition, increasing mass difference between group III and group VI elements leads to either enlarging phonon band gap or opening additional gaps. τ_{ph} is obtained from counting phonon modes with an average of 200 q -points in the transverse direction.

Average atomic mass, dispersion of the bands and phonon band gap play a key role for determining ballistic transmission spectrum. Although absence of available states inhibit phonon transmission, phonon band gap between low and high frequency optical modes has negligible effect on phonon thermal conductance (κ_{ph}). The reason is that, κ_{ph} is dominated by acoustic modes. κ_{ph} values are derived from Eq. 2.58 are shown in the Table 4.3. Unlike the κ_{ph} calculations of TMDs, applied temperature is lowered down to a 100 K for group III-chalcogenides.

κ_{ph} of the group III-VI compounds increases as temperature is increasing except heavy compounds such as TIPo. When considering structures consisting of light elements, one can see that κ_{ph} is boosted drastically as temperature is raised from 100 K to 300 K. This rapid increase is not observed for heavy compounds due to their suppressed acoustic frequencies. As an example, ω_{max} of the acoustic branches is about 1 THz for TIPo. From

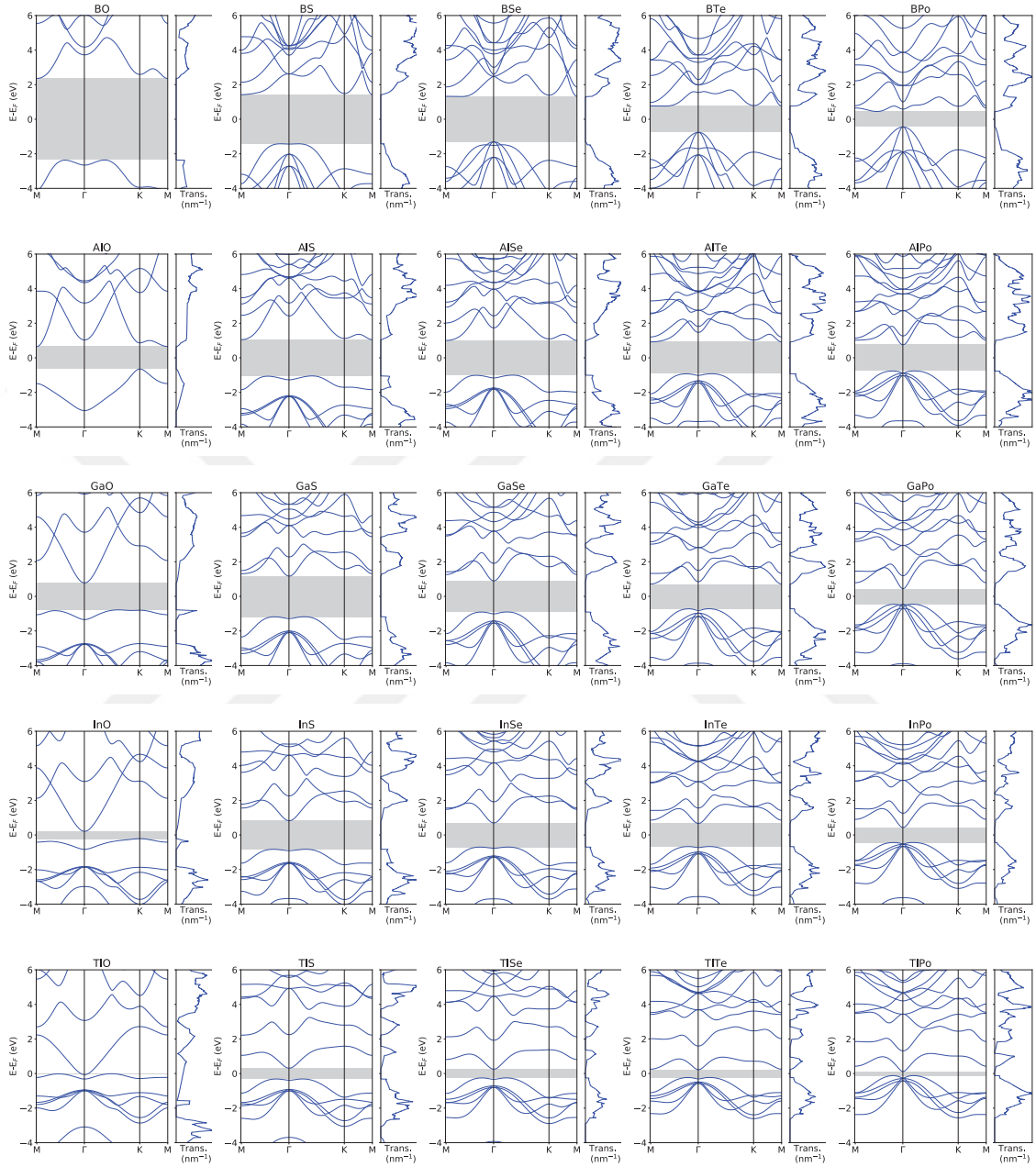


Figure 4.3. The electronic band structures and electronic transmission spectrums of the group III-monochalcogenides calculated at PBE level. Band gap values which are shown shaded area are listed in Table 4.1.

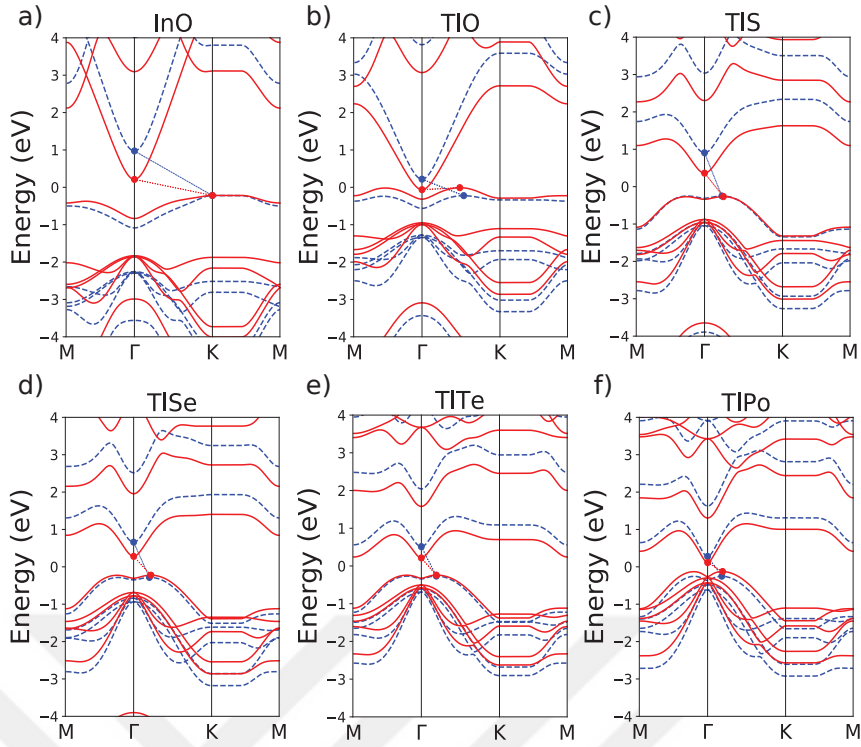


Figure 4.4. Calculated electronic band structures of narrow band gap and semi-metallic group III-VI compounds; a) InO, b) TlO, c) TlS, d) TlSe, e) TlPo based on PBE (red solid line) and PBE+HSE (blue dashed line) functional. Fermi level is set to zero for all subfigures.

the energy point of view, these branches are already occupied at 100 K. Therefore, κ_{ph} remains constant overall applied temperature range for TlTe and TlPo. κ_{ph} rapidly increases at low temperatures as related to dispersion of the acoustic bands when the average atomic mass of compounds slightly reduced. Starting from 500 K, convergence of κ_{ph} is detected. If we now consider light compounds, rapid increase in κ_{ph} decelerate but variation is maintained at high temperatures especially for BO, BS and AlO monolayers. In addition we can note that, as atomic mass of the chalcogen atom increases, κ_{ph} is significantly decreasing upon room temperature as in TMDs. AlX, GaX, InX and TiX families have also the same behaviour at 100 K. However, there is an anomalous trend arises from BO monolayer. According to the above discussions, the highest κ_{ph} value should be obtained for BO at 100 K due to its lightest elements composition. Surprisingly, BO monolayer exhibits a conductance value of 0.67 nW/K/nm which is lower than that of BS, AlO, AIS and GaO. In the next section, it seen that this unusual κ_{ph} will have a strong effect on thermoelectric performance at low temperatures.

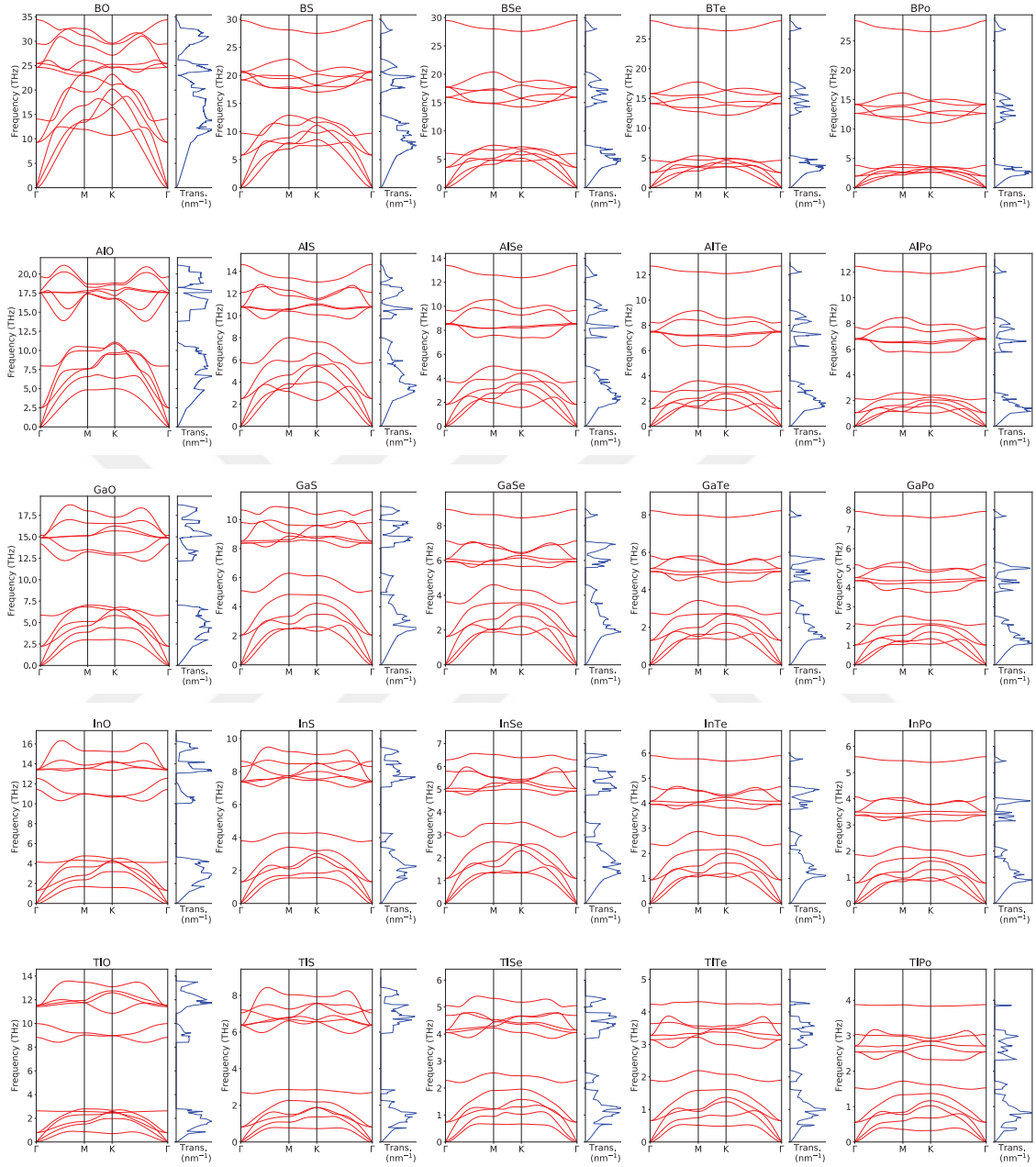


Figure 4.5. Phonon dispersion relations and phonon transmission spectrums for all studied materials.

4.3. Electronic Transport and Thermoelectric Properties

In order to calculate ballistic thermoelectric properties of group III-monochalcogenides, resulting electronic and phononic transmission spectrum are used as inputs for the L_n integrals (see Eq. 2.54). All TE coefficients which are embedded to thermoelectric figure of merit are calculated by performing the L_n integrals over energy and listed in Table 4.4 and Table 4.5. To keep the analysis of the results as general as possible, we will discuss the materials which are outstanding with their TE performance. First column in Table 4.4 belongs to thermoelectric figure of merit ZT which determines the TE efficiency of the material. Because of the ultra-low κ_{ph} of TIPO, it is no surprise being most efficient material among group III-VI at 100 K. Most interestingly, the lightest compound BO shows one of the most promising TE efficiency which corresponds to a similar ZT value with InS, TIS and TISe. We know from the previous section that BO possesses ultra-low κ_{ph} at 100 K which is beneficial for high ZT . This is a significant manifestation of possibility that BO should be good TE material at low temperatures. In the next chapter we will discuss BO in a detail. BSe, BTe, BPo and AIO exhibit remarkably poor p-type TE performance at 100 K. In the case of BSe, BTe and BPo, doubly degenerate valence bands move upward and hence, quartic band loose its effect on TE performance. Since the valence band edge is quite dispersive, AIO shows a very decent performance. The n-type ZT values reveal that most of the monolayers are suffer from dispersive conduction band edge. Surprisingly, BSe, BTe and BPo display an ultra-high n-type performance for 100 K due to the their flattened CB edge.

In order to enhance the thermoelectric efficiency of the materials, common strategies can be adopted, such as band flattening and band degeneracy. Existence of flat portion near the valence or conduction band edge gives rise to high density of states and hence induces high Seebeck coefficient. Flat band character and valley degeneracy are inherent in some group III-monochalcogenides. Now, we interpret flatness and degeneracy effects on thermoelectric properties as providing specific examples.

4.3.1. High n-type ZT Depending on Flatness and Valley Degeneracy

In this part we discuss the synergistic effect of flatness and valley degeneracy on the thermoelectric coefficients. Although their κ_{ph} values are found to be high BSe and BTe exhibit tremendous ZT values of 0.84 and 1.16 respectively at 300 K. The high

performance stems from the following features: (i) valley degeneracy occurs at M- Γ and K point in the lowermost conduction band which yields increase in G ; (ii) flat portion of the lowermost conduction band in which occurs at M- Γ gives rise to sharp variation in the transmission spectrum at the conduction band edge. In order to determine whether there is a valley degeneracy, energy difference between valleys should be within a few $k_B T$. In the case of BSe, M- Γ and K valleys are within 80 meV which is about $3 k_B T$. Therefore K valley also nourishes the carrier pockets and hence electronic conductance as can be seen from third column of the Table 4.6.

Second reason is the main source of the high n-type ZT . Seebeck coefficient is also expressed as the logarithmic derivative of the transmission with respect to energy with performing Sommerfeld expansion (see Eq. 3.3). High S coefficients desire rapid change in τ_{el} at the CBM and flat shaped CB edge meets this requirement. In Figure 4.6 three contour lines are drawn in 0.5 eV energy interval. Yellow dashed line cross over the flat portion and form two ellipsoid iso energy contours from M to Γ . Red and blue dashed lines generate ring-like contours around K point and also concentric ellipsoids from M to Γ .

4.3.2. High n-type ZT Depending on Valley Degeneracy

In this part we present three materials that exhibit valley degeneracy in their lowest conduction bands but valley degeneracy case is not limited to GaS, GaTe and TlTe. Also, AlX (S,Se,Te) can be classified in this group. GaS and GaTe display nearly the same conduction band character except that conduction band minima of the GaTe shift from Γ to M (see Figure 4.7(a) and 4.7(b)). Contour lines of GaS monolayer yield isoenergy maps which are of the same character with the GaTe. Corresponding circular rings around Γ and ellipsoid-like rings around M which are expanding towards K points are shown in Figure 4.7(a) and (b).

Energy offset between two valley is roughly $6k_B T$ for both structures. It is interesting to note that, a large n-type G and κ_{el} values are attained in GaS at room temperature. However n-type S coefficient is much less than the other structures. In contrast, GaTe possesses moderate n-type G and κ_{el} values but its n-type S coefficient is rather higher compared to GaS. As a result, GaS and GaTe show superior TE performance with n-type ZT values of 0.29 and 0.63 respectively within GaX group. Figure 4.7(c) depicts band diagram and isoenergy plots of TlTe monolayer which achieves an extraordinary n-type ZT value of 1.26 at 300 K. As taking into consideration two valley in the conduction band, one can see that TlTe reveals almost exact valley degeneracy which

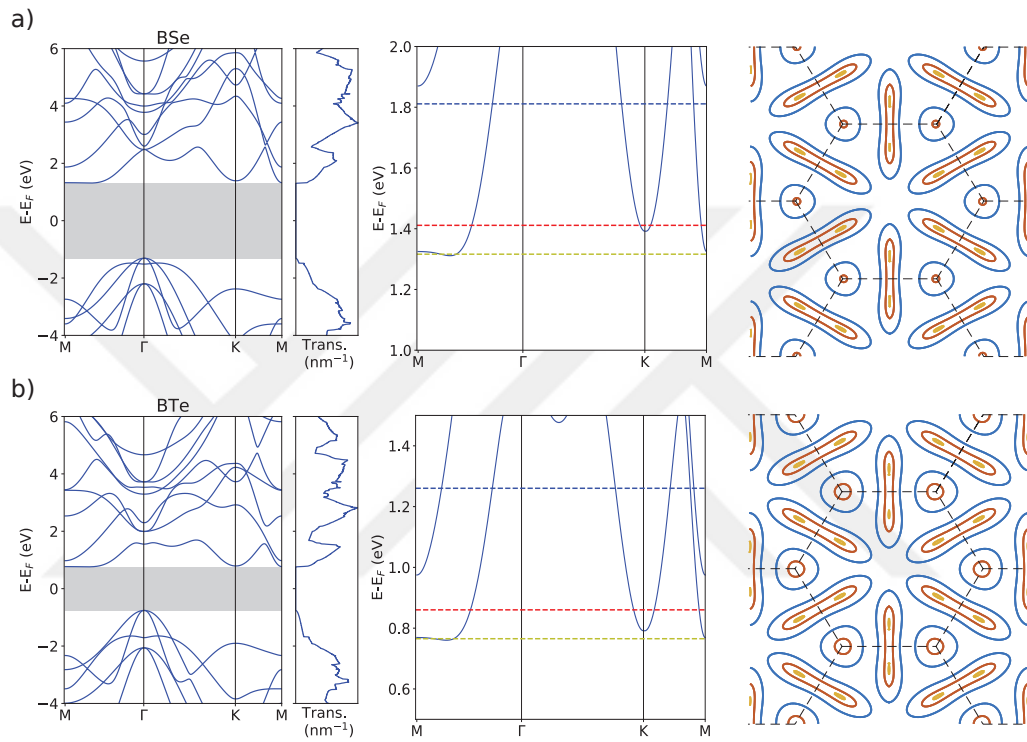


Figure 4.6. Electronic band structure, contour lines at $E - E_{CBM}$ with a value 0.5 (dashed blue), 0.1 (dashed red), 0.005 (dashed yellow) eV and related isoenergy surfaces near the conduction band in the entire Brillouin zone of a) BTe b) BSe monolayer.

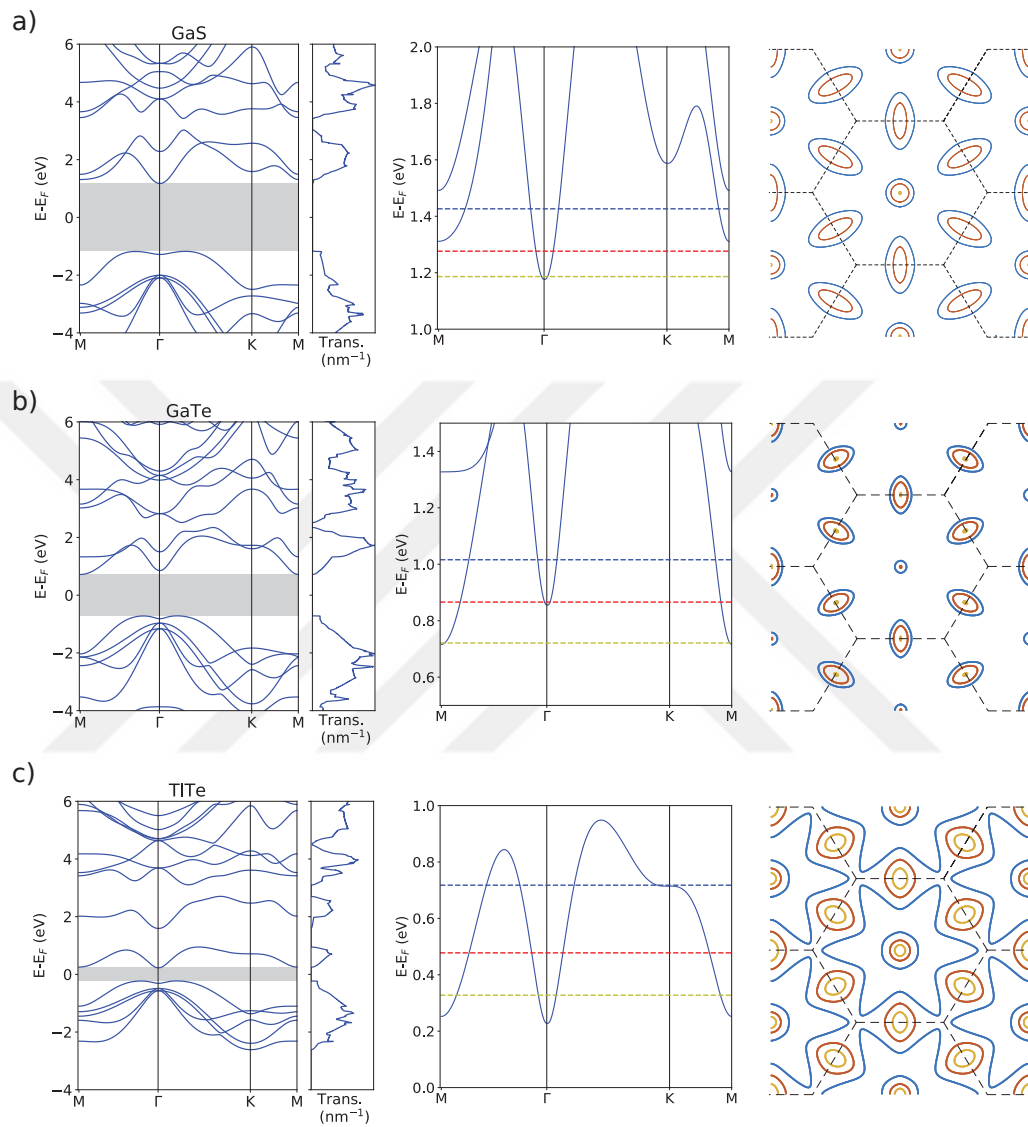


Figure 4.7. Electronic band structure, contour lines at $E - E_{CBM}$ and related isoenergy surfaces near the conduction band in the entire Brillouin zone of a) GaS b) GaTe c) TlTe monolayers.

give rise to considerable TE efficiency. This is probably due to highest S coefficient (-2.57 at 300 K) among allover group III-monochalcogenides. Isoenergy map is similar with GaS and GaTe except star-like contour which arises from flat portion of the band around K point. Flatness has negligible affect on TE coefficients since the energy difference is much larger than transport window range.

4.3.3. High p-type ZT Depending on Flatness and Valley Degeneracy

GaO monolayer exhibits both valley degeneracy and flat band character along Γ -K in the highest valence band. Figure 4.8(a) indicates that the energy difference between two valleys is less than $k_B T$. Although GaO is the lightest compound among GaX group, its p-type ZT takes value of 1.3 at 300 K which makes it a promising TE material candidate. In Table 4.4 and Table 4.6 one can see that, GaO monolayer has the highest p-type κ_{el} and G values at room temperature if we excluded semi-metal TlO. The detrimental effect of κ_{el} on TE performance is compensated by G . Therefore, excellent value of p-type ZT is originated from flatness of a valley along Γ -K. In Figure 4.8(a) three selected contour line are plotted. Yellow dashed line shows Fermi ring around Γ while the red one crosses the valence band at four points leading to two iso energy contour. The blue contour line passes through the valence band edge and forms core-like iso energy contours between Γ and K point. Next, we discuss TE properties of TlO monolayer with its valence band shape. In the uppermost valence band of TlO, the flat band portion shifts downward with a few $k_B T$ compared to VB character of GaO. Since TlO is a semi-metal, S coefficient is affected so much by the coexistence of the different type charge contributions which has the smallest value of 11.9 meV/K. Therefore TE efficiency is significantly reduced by S . However, in the presence of HSE06 hybrid functional ZT reaches 1.95 at room temperature by means of a correct band gap value (0.44 eV). This extraordinary performance arises from the participation of the flat plateau around K point and the valley degeneracy positioned at M- Γ and $\Gamma - K$. Also, iso energy pattern is very interesting. Yellow contour line intersects with the hat of the MHS and generates fermi ring around Γ as expected. Red contour line crosses both hat of the MHS from above and flat part of the valence band around K. Similarly, corresponding fermi ring positioned around Γ with a larger radius. Six ellipsoid-like iso energy contours exist in GaO, turn into continuous star-like ring.

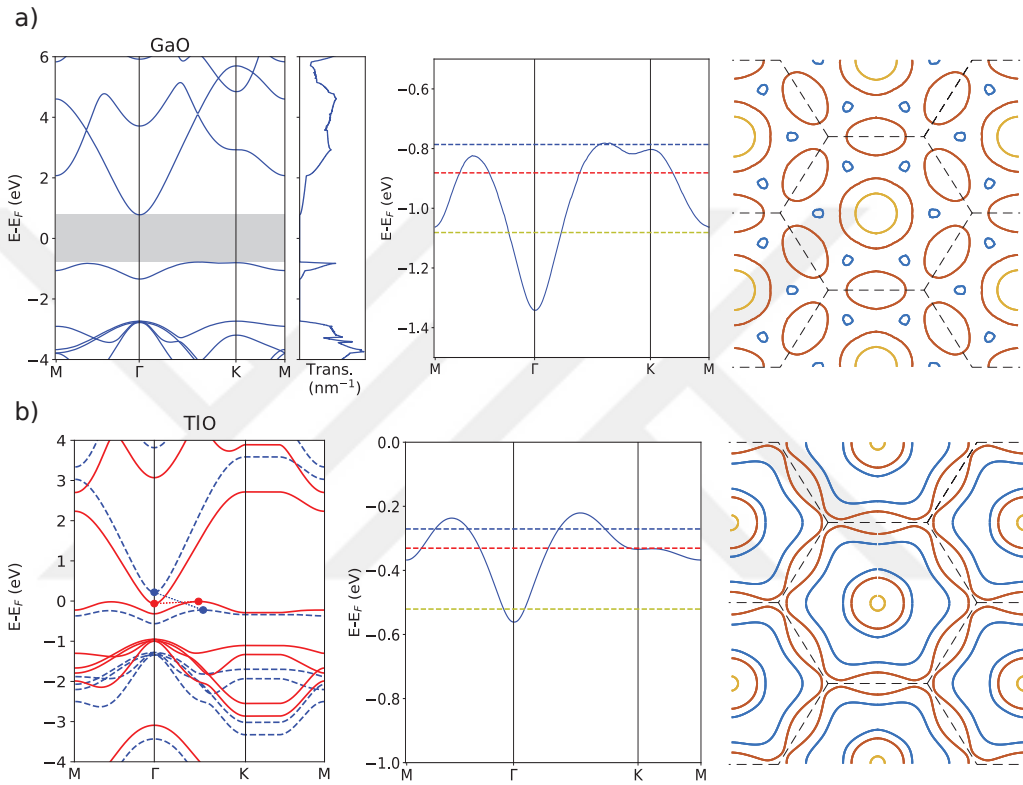


Figure 4.8. Electronic band structure, contour lines at $E_{VBM}-E$ and related isoenergy surfaces near the conduction band in the entire Brillouin zone of a) GaO b) TlO monolayers.

4.3.4. Quartic Band "Mexican Hat Shape" Effect on ZT

In order to clarify effect of Mexican hat shape, GaTe monolayer is taken into account since, its k_c value equals to 0.19 which is a signature of nearly pure quartic valence band. GaTe is the one of the material can be considered as heavy compound, therefore κ_{ph} is quite low. GaTe exhibits smallest value of G when compared to other member of GaX group. Likewise κ_{el} value is also smallest one in the GaX group. Apparently, as k_c value is decreasing in other words valence band is getting closer to the pure quartic band, G and κ_{el} are reduced. Because degenerate tops of the valence band evolve into broad and shallow type to narrow and sharper shape which yield decrease in conducting channels and hence G and κ_{el} . As shown in Figure 4.9 yellow dashed contour line crosses six point, therefore forms three iso energy contour. Two of them belong to doubly degenerate secondary valence bands which consist of light and heavy hole bands. The red contour line does not give us any new information about the band character because the yellow contour line also contains this information. Blue contour line entirely reveals quartic "Mexican Hat Shape" behaviour of the outermost valence band with isoenergy contour map. Fermi ring is located around Γ . As moving away from the Γ , the circular ring transforms into a hexagonal-like ring. It should be noted that, transmission and hence TE coefficients are mainly contributed by conducting channels in the Mexican hat since the energy difference between MHS and double degenerate bands is larger than few $k_B T$.

Table 4.1. a is the lattice constant, $d_{III-III}$, d_{VI-VI} and d_{III-VI} are bond lengths, θ_1 and θ_2 show bond angles and E_g gives bandgap of monolayers based on GGA-PBE functional. These structural parameters are illustrated in Fig. 4.1.

III-VI	a (Å)	$d_{III-III}$ (Å)	d_{VI-VI} (Å)	d_{III-VI} (Å)	θ_1 (deg)	θ_2 (deg)	E_g (eV)
BO	2.45	1.77	2.92	1.53	112.11	106.71	4.72
BS	3.04	1.72	3.42	1.95	115.80	102.47	2.84
BSe	3.25	1.71	3.61	2.10	116.73	101.33	2.62
BTe	3.56	1.71	3.83	2.31	117.22	100.74	1.52
BPo	3.72	1.70	3.96	2.43	117.70	100.13	0.90
AlO	2.97	2.62	3.94	1.84	111.08	107.81	1.31
AlS	3.58	2.60	4.73	2.33	117.29	100.65	2.10
AlSe	3.78	2.59	4.92	2.47	118.12	99.60	2.00
AlTe	4.12	2.57	5.13	2.70	118.34	99.32	1.84
AlPo	4.25	2.57	5.28	2.80	118.85	98.67	1.52
GaO	3.12	2.52	4.00	1.94	112.46	106.32	1.56
GaS	3.64	2.48	4.66	2.37	117.44	100.45	2.35
GaSe	3.82	2.47	4.83	2.50	118.12	99.68	1.80
GaTe	4.13	2.47	5.03	2.71	118.16	99.56	1.43
GaPo	4.26	2.47	5.14	2.80	118.49	99.14	0.90
InO	3.47	2.86	4.47	2.16	111.94	106.89	0.43
InS	3.94	2.82	5.20	2.57	117.61	100.24	1.65
InSe	4.09	2.82	5.39	2.69	118.52	99.10	1.40
InTe	4.39	2.82	5.60	2.89	118.82	98.81	1.34
InPo	4.50	2.82	5.73	2.98	119.27	98.23	0.87
TlO	3.69	2.92	4.63	2.29	111.80	107.04	semi-metal
TlS	4.12	2.87	5.31	2.67	117.16	100.80	0.63
TlSe	4.27	2.87	5.48	2.79	117.90	99.88	0.50
TlTe	4.56	2.88	5.68	2.98	118.05	99.69	0.46
TlPo	4.65	2.88	5.79	3.05	118.43	99.21	0.24

Table 4.2. Critical wave vector k_c and α parameters of group III-monochalcogenides.

	k_c					α				
	O	S	Se	Te	Po	O	S	Se	Te	Po
B	0.63	0.23	-	-	-	1.84	6.11	-	-	-
Al	-	0.49	0.39	0.24	0.21	-	3.83	7.17	26.44	63.94
Ga	-	0.32	0.26	0.19	-	-	10.05	22.45	72.78	-
In	-	0.32	0.27	0.19	0.18	-	7.95	14.33	42.75	79.8
Tl	0.56	0.26	0.23	0.18	0.18	3.19	17.18	31.77	73.53	129.52

Table 4.3. Phonon thermal conductance values in a wide temperature range from 100 K to 1000 K.

MX	κ_{ph} (nW/K/nm)				
	100 K	300 K	500 K	800 K	1000 K
BO	0.67	3.58	5.09	5.94	6.18
BS	0.77	2.02	2.39	2.57	2.61
BSe	0.72	1.32	1.52	1.62	1.65
BTe	0.56	0.92	1.03	1.09	1.10
BPo	0.43	0.73	0.83	0.87	0.88
AlO	0.88	2.24	2.65	2.84	2.88
AlS	0.70	1.16	1.24	1.27	1.28
AlSe	0.55	0.78	0.81	0.83	0.83
AlTe	0.41	0.54	0.56	0.56	0.57
AlPo	0.32	0.42	0.43	0.44	0.44
GaO	0.72	1.34	1.51	1.58	1.60
GaS	0.53	0.79	0.83	0.85	0.85
GaSe	0.47	0.60	0.61	0.62	0.62
GaTe	0.37	0.43	0.44	0.44	0.44
GaPo	0.30	0.37	0.34	0.34	0.34
InO	0.55	0.85	0.92	0.95	0.96
InS	0.40	0.55	0.57	0.58	0.58
InSe	0.36	0.43	0.44	0.44	0.44
InTe	0.28	0.31	0.31	0.31	0.31
InPo	0.22	0.24	0.24	0.24	0.24
TlO	0.36	0.60	0.65	0.67	0.68
TlS	0.30	0.42	0.43	0.44	0.44
TlSe	0.26	0.30	0.30	0.31	0.31
TlTe	0.21	0.22	0.23	0.23	0.23
TlPo	0.17	0.17	0.18	0.18	0.18

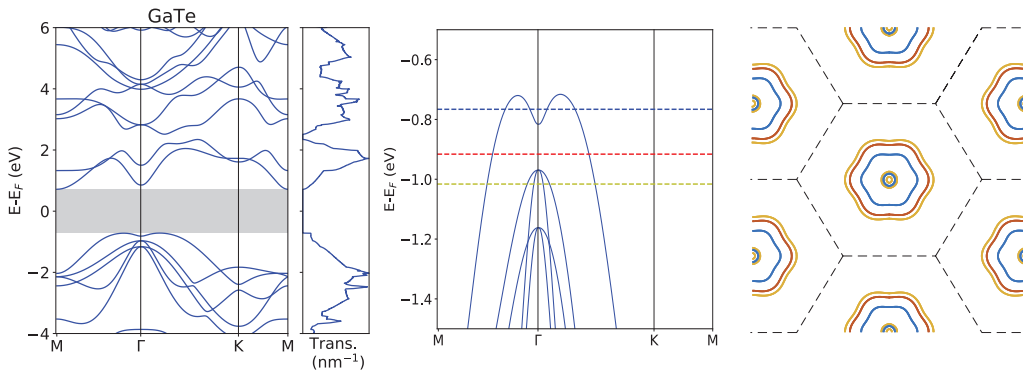


Figure 4.9. Electronic band structure, contour lines at $E_{VBM}-E$ and related isoenergy surfaces near the conduction band in the entire Brillouin zone of GaTe monolayer.

Table 4.4. Thermoelectric figure of merit ZT and power factor PF values in which ZT reaches peak value from 100 K to 1000 K.

MX	ZT					PF (10^{-3} nW/K ² nm)				
	100 K	300 K	500 K	800 K	1000 K	100 K	300 K	500 K	800 K	1000 K
BO	0.64/0.15	0.42/0.14	0.49/0.21	0.64/0.38	0.74/0.51	4.65/1.02	5.45/1.79	5.45/2.35	5.29/3.20	5.18/3.79
BS	0.22/0.17	0.26/0.37	0.39/0.67	0.61/1.15	0.77/1.47	1.78/1.42	1.89/2.84	2.06/3.89	2.24/4.86	2.37/5.31
BSe	0.06/0.43	0.15/0.84	0.35/1.27	0.80/1.91	1.12/2.31	0.70/3.42	0.69/4.53	1.27/5.03	2.18/5.56	2.62/5.55
BTe	0.06/0.52	0.18/1.16	0.33/1.74	0.59/2.55	0.78/3.06	0.34/3.34	0.59/4.69	0.77/4.93	0.96/5.34	1.07/5.42
BPo	0.07/0.33	0.21/0.89	0.38/1.51	0.67/2.47	0.83/3.05	0.31/1.62	0.55/2.80	0.70/3.57	0.87/4.23	0.98/4.57
AlO	0.05/0.09	0.1/0.18	0.18/0.33	0.34/0.64	0.46/0.87	0.4/0.79	0.77/1.43	1.03/1.95	1.35/2.79	1.54/3.30
AlS	0.47/0.12	0.91/0.38	1.32/0.78	1.85/1.43	2.16/1.85	3.52/0.85	4.18/1.67	4.07/2.41	3.79/3.12	3.67/3.40
AlSe	0.49/0.15	1.04/0.54	1.5/1.07	2.09/1.92	2.43/2.47	2.88/0.9	3.25/1.63	3.02/2.33	2.94/2.94	2.79/3.13
AlTe	0.48/0.25	0.99/0.82	1.46/1.51	2.07/2.55	2.43/3.23	2.17/1.09	2.10/1.87	2.09/2.44	2.05/3.01	2.01/3.20
AlPo	0.52/0.17	1.11/0.43	1.67/0.7	2.46/1.27	2.97/1.94	1.89/0.94	1.91/1.77	1.92/2.60	2.11/3.60	2.19/2.22
GaO	0.55/0.03	1.3/0.08	1.79/0.14	2.35/0.26	2.64/0.35	5.2/0.21	7.15/0.35	6.77/0.44	5.77/0.56	5.13/0.64
GaS	0.47/0.08	0.89/0.29	1.28/0.64	1.81/1.48	2.14/2.10	2.84/0.62	2.72/1.41	2.64/2.06	2.51/2.71	2.49/3.25
GaSe	0.44/0.03	0.97/0.12	1.43/0.24	2.05/0.51	2.4/0.80	2.34/0.13	2.28/0.24	2.25/0.32	2.18/0.50	2.11/0.76
GaTe	0.44/0.16	1.01/0.63	1.52/1.17	2.19/1.98	2.6/2.48	1.75/0.65	1.71/1.08	1.74/1.35	1.79/1.67	1.81/1.77
GaPo	0.50/0.03	1.36/0.14	2.13/0.28	3.12/0.63	3.65/0.94	1.70/0.09	2.02/0.16	2.10/0.21	2.19/0.36	2.26/0.57
InO	0.19/0.03	0.7/0.11	1.29/0.22	1.84/0.28	1.79/0.24	1.09/0.18	2.45/0.33	3.16/0.43	3.09/0.48	2.87/0.45
InS	0.64/0.04	1.19/0.16	1.69/0.31	2.36/0.58	2.77/0.77	2.84/0.16	2.61/0.30	2.43/0.39	2.37/0.49	2.38/0.56
InSe	0.56/0.04	1.24/0.17	1.82/0.34	2.57/0.65	3/0.86	2.35/0.15	2.11/0.26	2.13/0.33	2.01/0.42	2.06/0.48
InTe	0.56/0.06	1.29/0.25	1.92/0.55	2.72/1.45	3.17/2.17	1.70/0.29	1.64/0.78	1.60/0.45	1.59/1.02	1.63/1.29
InPo	0.60/0.05	1.5/0.22	2.27/0.44	3.35/0.81	3.94/1.00	1.46/0.10	1.56/0.19	1.65/0.24	1.83/0.33	1.96/0.42
TlO	0.49/0.23	0.59/0.59	0.57/0.58	0.46/0.48	0.35/0.38	3.34/0.38	3.39/3.14	2.88/3.03	1.85/2.14	1.24/1.57
TlS	0.63/0.06	1.22/0.2	1.77/0.40	2.42/0.66	2.48/0.66	2.09/0.17	2.05/0.30	2.06/0.39	2.02/0.50	2.15/0.57
TlSe	0.64/0.05	1.47/0.24	2.14/0.47	2.53/0.59	2.17/0.49	1.98/0.14	1.80/0.25	1.84/0.34	1.87/0.43	2.05/0.50
TlTe	0.69/0.24	1.65/1.26	2.34/2.17	1.63/1.92	1.08/1.46	1.66/0.66	1.53/1.25	1.61/1.61	1.92/2.39	2.15/2.72
TlPo	0.78/0.08	1.92/0.25	2.08/0.42	1.32/0.70	1.01/0.80	1.40/0.28	1.50/0.72	1.62/1.12	1.93/1.63	2.22/2.02

Table 4.5. Seebeck coefficient S and electronic contribution to the thermal conductance κ_{el} values in which ZT reaches peak value from 100 K to 1000 K.

MX	S (10^{-4} V/K)					κ_{el} (10^{-1} nW/K nm)				
	100 K	300 K	500 K	800 K	1000 K	100 K	300 K	500 K	800 K	1000 K
BO	2.63/-1.79	2.22/-1.94	2.11/-1.98	2.16/-2.1	2.20/-2.13	0.61/0.42	2.72/1.81	4.89/3.97	7.03/8.28	8.22/12.03
BS	2.17/-1.76	2.09/-2.01	2.11/-2.23	2.25/-2.43	2.24/-2.52	0.29/0.61	1.24/2.98	2.30/5.18	3.58/8.06	4.87/10.00
BSe	0.60/-2.21	2.06/-2.20	1.98/-2.39	2.27/-2.57	2.37/-2.79	4.28/0.77	0.73/2.88	3.10/4.60	5.56/7.12	6.88/7.58
BTe	2.12/-2.22	2.04/-2.23	2.03/-2.59	2.18/-2.82	2.23/-3.00	0.092/0.79	0.53/2.90	1.16/3.79	2.00/5.87	2.67/6.66
BPo	1.77/-1.90	1.94/-2.27	2.13/-2.55	2.24/-2.88	2.19/-2.97	0.13/0.58	0.55/2.10	0.95/3.60	1.73/5.02	2.88/6.13
AlO	2.28/-2.21	1.86/-2.09	1.94/-2.10	2.05/-2.22	2.15/-2.32	0.096/0.2	0.88/1.25	1.80/3.07	3.46/6.79	4.55/8.95
AlS	2.54/-2.10	2.20/-2.13	2.28/-2.35	2.5/-2.53	2.57/-2.59	5.32/0.23	2.12/1.62	3.04/3.09	3.7/4.74	4.23/5.54
AlSe	2.57/-1.79	2.18/-2.26	2.45/-2.42	2.49/-2.70	2.67/-2.82	0.39/0.36	1.64/1.32	1.93/2.79	3.01/4.00	3.19/4.39
AlTe	1.99/-1.91	2.28/-2.27	2.35/-2.57	2.58/-2.93	2.78/-3.14	0.48/0.38	0.98/1.42	1.60/2.51	2.26/3.79	2.59/4.23
AlPo	1.83/-0.9	2.24/1.2	2.56/-1.47	2.82/-1.94	3.03/-2.94	0.50/2.50	1/8.24	1.47/14.2	2.51/18.3	2.99/7.13
GaO	1.86/-1.81	2.39/-1.91	2.35/-1.95	2.32/-2.03	2.34/-2.03	2.16/0.08	3.08/0.35	3.78/0.74	3.80/1.39	3.37/1.97
GaS	1.91/-0.86	2.24/-1.21	2.30/-1.70	2.53/-2.61	2.62/-2.87	0.68/2.12	1.27/6.43	1.99/7.71	2.64/6.21	3.16/7.02
GaSe	1.94/-2.13	2.26/-2.06	2.33/-2.06	2.56/-2.29	2.75/-2.54	0.55/0.036	1.08/0.21	1.71/0.50	2.33/1.63	2.59/3.29
GaTe	2.23/-1.78	2.37/-2.20	2.41/-2.48	2.67/-2.73	2.89/-2.98	0.29/0.26	0.76/0.84	1.33/1.39	2.13/2.36	2.55/2.71
GaPo	1.88/-2.07	2.36/-2.04	2.66/-2.06	2.99/-2.35	3.15/-2.49	0.47/0.026	1.07/0.15	1.51/0.36	2.19/1.19	2.74/2.56
InO	2.33/-2.22	2.25/-1.82	2.31/-1.90	2.26/-1.44	1.93/-1.13	0.26/0.046	2.04/0.39	3/0.84	3.9/4.20	6.45/8.78
InS	2.21/-2.22	2.32/-2.09	2.54/-2.06	2.70/-2.21	2.76/-2.28	0.45/0.042	1.11/0.26	1.51/0.58	2.25/1.04	2.79/1.47
InSe	1.77/-1.78	2.49/-1.94	2.47/-2.14	2.78/-2.27	2.84/-2.32	0.63/0.059	0.80/0.26	1.47/0.46	1.88/0.85	2.46/1.21
InTe	2.22/-0.63	5.14/-0.93	3.63/-2.26	3.96/-2.72	3.52/-3.03	0.27/1.84	0.74/6.26	1.07/0.98	1.58/2.49	2.02/2.85
InPo	2.39/-1.60	2.47/-1.88	2.75/-2.11	3.11/-2.30	3.28/-2.35	0.22/0.054	0.72/0.21	1.22/0.35	1.97/0.81	2.57/1.76
TlO	1.53/0.83	1.19/1.40	1.05/1.20	0.84/0.98	0.69/0.85	3.26/2.82	11.73/11.40	19.85/19.73	27.31/29.34	30.74/34.95
TlS	2.38/-1.98	2.41/-2.00	2.43/-2.02	2.63/-2.06	2.51/-1.73	0.30/0.054	0.84/0.28	1.49/0.62	2.31/1.62	4.26/4.15
TlSe	1.84/-2.18	2.53/-2.09	2.50/-2.08	2.54/-1.69	2.25/-1.41	0.18/0.036	0.67/0.22	1.26/0.54	2.84/2.79	6.41/7.12
TlTe	2.03/-1.32	2.62/-2.57	2.57/-2.72	2.04/-2.15	1.70/-1.78	0.36/0.67	0.55/0.74	1.20/1.49	7.19/7.69	17.55/16.42
TlPo	2.69/-0.59	2.53/-0.86	2.30/-1.06	1.82/-1.36	1.64/-1.42	0.15/1.99	0.61/6.88	2.14/11.64	9.96/17.04	20.09/23.58

Table 4.6. Electronic conductance values G in which ZT reaches peak value from 100 K to 1000 K.

MX	G ($10^{-1} G_0/\text{nm}$)				
	100 K	300 K	500 K	800 K	1000 K
BO	8.66/4.12	14.32/6.16	15.75/7.75	14.68/9.34	13.83/10.76
BS	4.89/5.95	5.59/9.06	5.97/10.1	5.73/10.63	6.11/10.82
Bse	25.05/9.06	2.11/12.05	4.18/11.35	5.47/10.88	6.04/9.24
Bte	0.98/8.76	1.83/12.11	2.40/9.49	2.60/8.66	2.76/7.76
Bpo	1.26/5.79	1.87/7.02	1.98/7.1	2.23/6.61	2.64/6.68
AlO	1.0/2.07	2.87/4.21	3.52/5.72	4.16/7.33	4.33/7.94
AlS	7.06/2.48	11.12/4.74	10.08/5.63	7.85/6.29	7.19/6.54
AlSe	5.65/3.6	8.8/4.12	6.49/5.13	6.12/5.21	5.06/5.07
AlTe	7.06/3.84	5.23/4.67	4.9/4.76	3.96/4.51	3.35/4.18
AlPo	7.3/14.88	4.90/15.81	3.78/15.43	3.41/12.34	3.07/3.32
GaO	19.33/0.83	16.21/1.22	15.76/1.50	13.87/1.77	12.07/1.99
GaS	10.05/10.92	7/12.43	6.42/9.16	5.06/5.14	4.68/5.09
GaSe	8.07/0.38	5.77/0.72	5.35/0.96	4.28/1.22	3.6/1.52
GaTe	4.57/2.63	3.94/2.89	3.85/2.82	3.23/2.90	2.80/2.57
GaPo	6.2/0.27	4.66/0.49	3.82/0.65	3.16/0.85	2.93/1.17
InO	2.6/0.48	6.26/1.30	7.62/1.56	7.84/2.96	10/4.51
InS	7.48/0.43	6.24/0.88	4.86/1.18	4.21/1.30	4.04/1.40
InSe	9.67/0.6	4.41/0.88	4.50/0.93	3.36/1.06	3.29/1.15
InTe	4.46/9.5	3.79/11.69	3.04/1.13	2.42/1.78	2.20/1.82
InPo	3.32/0.51	3.30/0.68	2.82/0.70	2.45/0.80	2.35/0.98
TlO	18.34/7.02	30.98/20.65	33.91/27.19	34.27/28.57	33.24/27.89
TlS	4.74/0.57	4.56/0.96	4.51/1.24	3.76/1.51	4.39/2.43
TlSe	7.57/0.38	3.65/0.75	3.80/1.01	3.72/1.94	5.21/3.25
TlTe	5.21/4.87	2.88/2.43	3.15/2.80	5.93/6.65	9.58/11.07
TlPo	2.49/10.37	3.03/12.44	3.93/12.83	7.54/11.46	10.68/13.01

CHAPTER 5

BX (X=O,S) MONOLAYERS:PROMISING THERMOELECTRIC PERFORMANCE AT LOW TEMPERATURES

5.1. Structural and Electronic Properties

Like group III-monochalcogenides, BO and BS monolayers are explored in α -phase as can be seen in 5.1(a). Unit cell includes four atoms which have M_2X_2 formulation. Crsytal strcuture can be considered as two buckled layer are combined with B-B covalent bonding. Structural parameters are given in Table 5.1, which includes lattice constants, bond lengths and bond angles obtained by performing structural optimization. Our findings are in good agreement with (Demirci et al. (2017)). As radius is increasing from the oxygen to sulfur atom, a , d_{VI-VI} , d_{III-VI} and the angle θ_1 are increasing while $d_{III-III}$ and angle θ_2 are decreasing. According to the PBE functional results, both BO and BS

Table 5.1. a is the lattice constant, $d_{III-III}$, d_{VI-VI} and d_{III-VI} are bond lengths, θ_1 and θ_2 show bond angles and E_g gives bandgap of monolayers based on GGA-PBE. These structural parameters are also shown in Figure. 5.1.

	a (\AA)	$d_{III-III}$ (\AA)	d_{VI-VI} (\AA)	d_{III-VI} (\AA)	θ_1 (deg)	θ_2 (deg)	E_g (eV)
BO	2.45	1.77	2.92	1.53	112.11	106.71	4.72
BS	3.04	1.72	3.42	1.95	115.80	102.47	2.84

monolayers are semiconductors with a wide, indirect band gaps 4.72 eV and 2.84 eV respectively as indicated by shaded area in the first column of Figure 5.1(b) and Fig 5.1(e). For both structures, band gap values are sufficient in order to hinder simultaneous n- and p-type charge carrier contributions from conduction and valence bands. Enlarging the band gap of BO and BS does not lead any significant change in electronic transport properties. Therefore, it is not necessary adopting hybrid functionals correction. As

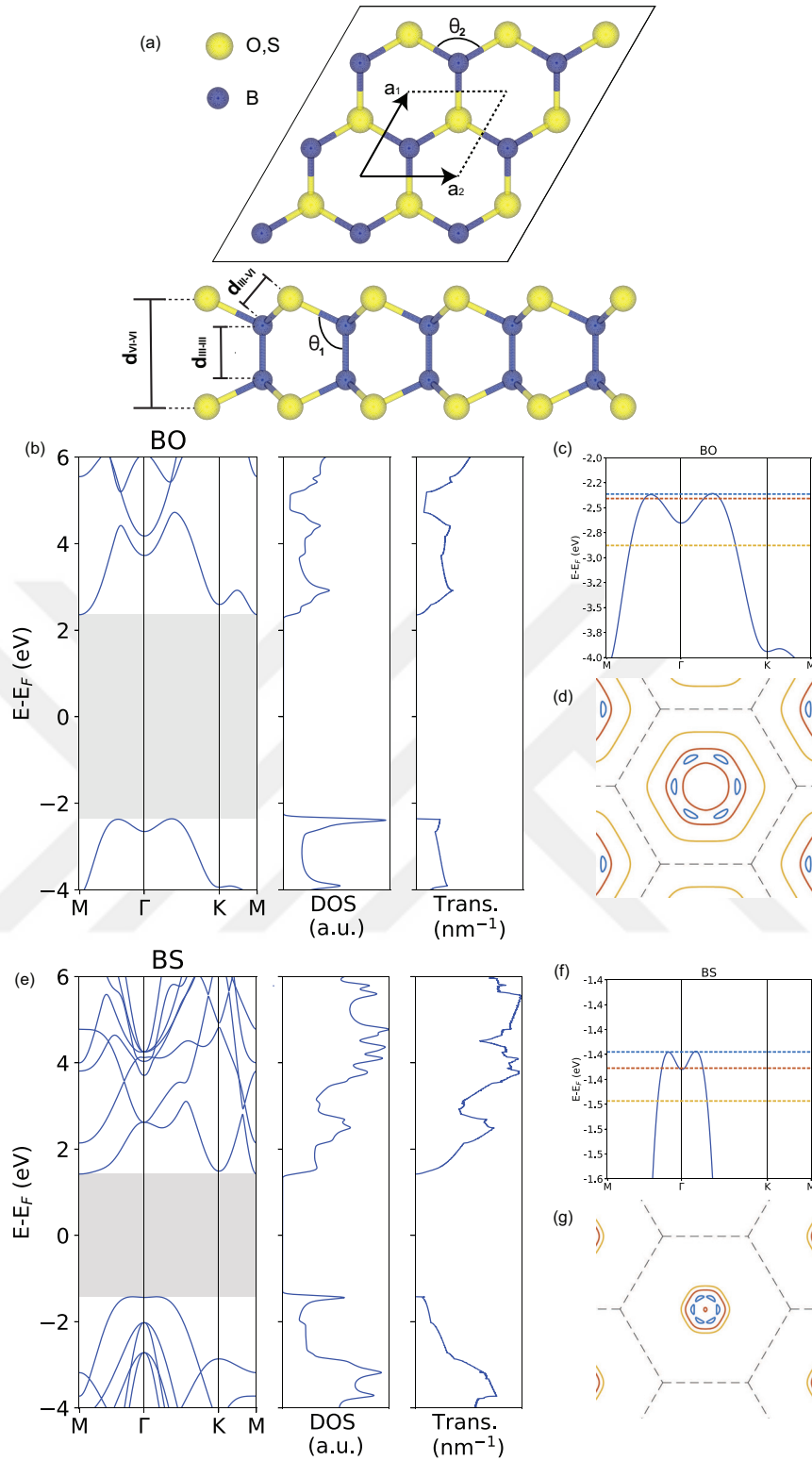


Figure 5.1. (a) Schematic illustration of the unitcell from the top and side view. (b) and (e) Electronic band structure, density of states, and electronic transmission spectra of BO and BS monolayer respectively. (c) and (f) Selected contour lines for BO and BS monolayer. (d) and (g) Isoenergy surface plot of the selected contour lines which are shown in (c) and (f).

demonstrated in the first column of Figure 5.1(b) and Fig 5.1(e), valence bands of BO and BS have distinctive dispersion around Γ point which is called "Mexican hat shape" (MHS) as mentioned in Chapter 4. MHS character corresponds to quartic energy-momentum relation $E = E_v - \alpha(k^2 - k_c^2)^2$ and responsible for a strong singularity of the type $g(E) \sim 1/\sqrt{E}$ in density of states (DOS) at the valence band edge (VBE) (see second column of Figure 5.1(b) and Figure 5.1(e)). Sharp peak in DOS results in step-like electronic transmission spectrum at the VBE. In Figure 5.1(c) and Figure 5.1(f) only the uppermost valence bands are considered in order to elucidate MHS. MHS valence band induces an approximate circular ring in reciprocal space. Three contour lines are selected in a range of 0.6 and 0.1 eV, by considering the hat height of MHS for BO and BS respectively. Blue dashed lines which pass through two degenerate top points, form ellipse-like iso-energy surfaces on the path from Γ to K as demonstrated with iso-energy contour plot in Fig. 5.1 (d) and (e). The red dashed line forms a Fermi ring which is an indication of MHS character. When line crossing is occurred near the Γ point, we see there exist circular Fermi rings. Eventually, as moving away from Γ , circular ring transforms into hexagonal-like Fermi ring for BO and BS. Fermi ring takes a point-like form when selected contour line touches the dip at Γ point as seen from Figure 5.1(f). The calculated critical wave vector values are $k_c=0.63 \text{ \AA}^{-1}$ and $k_c=0.23 \text{ \AA}^{-1}$ for BO and BS respectively. Since, peaks of the valence band of BS monolayer shift toward Γ point, equi-energy contours have a smaller radius compared to BO. Step height of the transmission spectra at the VBE is closely related to the height of the MHS and k_c . Since, small energy difference between primary and the secondary CBM which is located at K point, there exist valley degeneracy in conduction band of BS monolayer (see Figure 5.1(b)). Such a valley degeneracy gives rise to an increase in n-type charge carrier population that contributes to electronic transport. It is clearly seen that from Table 4.5, n-type G and n-type κ_{el} values for BS are higher than that of BO up to 800 K. Moreover, conduction band edge (CBE) possesses a nearly flat band form which results in a sharp-peaked DOS and enhancement in Seebeck coefficient as seen from Figure 5.1(e). More details on how this kind of band structures bring advantages to the thermoelectric efficiency are analyzed in further discussions.

5.2. Thermal Transport Properties

Fig. 5.2 illustrates phonon dispersion relations of the BO and BS monolayer. Since the unit cell of these structures includes four atoms, there exist three acoustic and nine optical branches. For 2D structures, three acoustic branches which are flexural out-of-

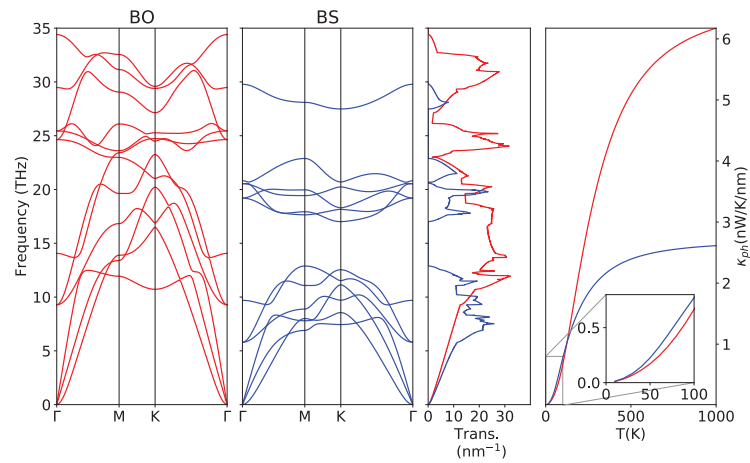


Figure 5.2. Phonon dispersion, transmission spectrum and the thermal conductance as a function of temperature of BO and BS structures. Red and blue lines indicate that BO and BS monolayers respectively.

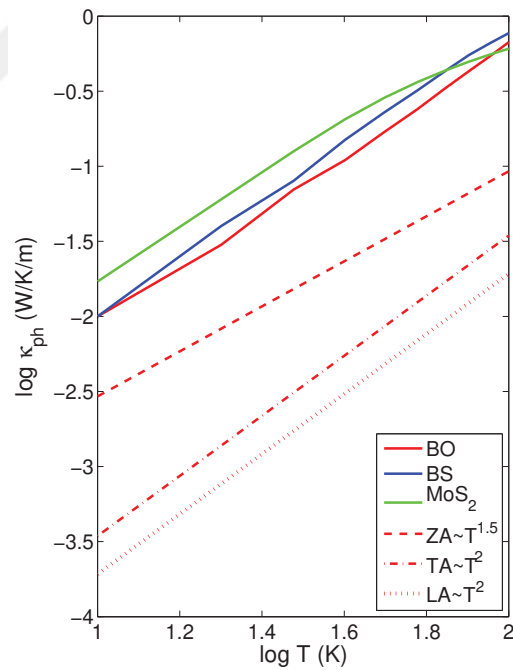


Figure 5.3. Comparison of logarithmic phonon thermal conductance of BO, BS, InS and three longitudinal-acoustic (LA), transverse-acoustic (TA) and out-of-plane (ZA) acoustic branches belong to BO in a temperature range from 10 K to 100 K.

plane (ZA), longitudinal (LA) and transverse acoustic (TA) modes mainly determine the phonon thermal conductance (κ_{ph}). Absence of the negative frequencies along whole high symmetry points implies that both BO and BS are dynamically stable. Because the vibrational frequency proportional to the inverse square root of atomic mass, high frequency optical modes reach values of 35 THz and 30 THz for BO and BS respectively. For two structure, acoustic branches are located in the 0.0-20 THz and 0.0-11 THz frequency range. Low and high frequency optical modes touch to each other around M point, while these modes are separated in BS which leads to phonon band gap.

The calculated τ_{ph} and κ_{ph} of both structures are illustrated in Fig. 5.2. It can be seen that the τ_{ph} of BO is much larger than that of BS at high frequencies while at low frequencies τ_{ph} of BO and BS possess almost overlap. This is reasonable since the dispersion of the acoustic branches at the long wave limit are very similar. The reason why the κ_{ph} of BS is much smaller than that of BO at high temperatures is that heavier atomic mass of BS compared to that of BO. In addition, phonon band gap between low frequency and high frequency optical branches may block transport channels. Nevertheless, κ_{ph} is expected to be dominated by acoustic modes, phonon band gap between optical modes has a negligible effect on κ_{ph} . Furthermore, κ_{ph} of BO and BS remain almost stable after rapidly increasing in different temperature ranges. Since acoustic branches have already been occupied due to the suppression in vibrational frequencies, κ_{ph} of BS converges at lower temperatures compared to that of BO. When the contribution of acoustic branches to the κ_{ph} is calculated separately, it is seen that κ_{ph} of ZA mode has a $T^{3/2}$ dependence whereas κ_{ph} of LA and TA mode is proportional to the T^2 as in graphene sheet (Mingo and Broido (2005); Saito et al. (2007)). For details of the calculations, see A. Inset of the Figure 5.2 displays κ_{ph} trend as a function of temperature from 3 K to 100 K. κ_{ph} of BS is slightly larger than that of BO under 100 K. From the slope of the $\log\kappa_{ph}$ as a function of $\log T$, it is seen that κ_{ph} of BO has a $T^{1.85}$ dependency that is close to the average of the acoustic modes contribution, while κ_{ph} of BS changes with $T^{1.90}$. This explains why κ_{ph} of BS is slightly larger than that of BO under 100 K.

5.3. Electronic Transport and Thermoelectric Properties

Knowledge of TE coefficients of BO and BS monolayers above 100 K exists in Table 4.4 and Table 4.5 in Chapter 4. In this section, we focus on low-temperature TE properties of BO and BS monolayers motivated by unusual temperature dependence on ZT under room temperature. Analyses of TE properties are performed by comparing

analytical and numerical calculations in order to gain better understanding of physical picture of low temperature thermoelectrics. Analytical derivations of TE coefficients are made for two separate cases which are quartic and quadratic band structure. Here, we first consider p/n-type TE properties of BO monolayer. As can be seen from Eq. 5.11, BO has p-type electronic conductance G which is independent of the temperature near the VBE. Since, there are no available states in the band gap, G starts to decrease and goes to zero when chemical potential shifts towards the band gap as shown in Figure 5.4(a). Although analytical calculations for quadratic transmission spectra at the VBE gives $T^{1/2}$ (see Eq. 5.27) dependence for n-type G , it exhibits universality. According to our prediction, this discrepancy can be originated from the following reason that, $\tau(E)$ does not possess \sqrt{E} dependency at the VBE. One can conclude that the $\tau(E)$ varies more rapidly than it should be. p-type G value is nearly 5 times larger than n-type G due to the highly degenerate peaks of the valence band. More charge carrier pockets contribute to the p-type G . p/n-type S curves belonging to various temperatures intersect each other at the VBE and CBE. Temperature independence of S at the VBE is also confirmed by analytical calculations. While p-type S value is found 0.12 meV/K from Eq. 5.13 for exact step function type transmission spectra, n-type S takes value of 0.16 meV/K. Because the p-type S and G seem to be independent of the temperature at the VBE, power factor ($PF = S^2G$) is expected to be temperature independent. However, PF increases as temperature increases. This is reasonable, since the temperature independence of S and G occurs at different chemical potentials, the PF varies with temperature at the edge of the valence band as shown in Figure 5.4(a). Compared to n-type PF , p-type PF has a much higher value, leading to large enhancement of the ZT . p-type electronic contribution to the thermal conductance κ_{el} is significantly decreasing as T falls from 100 K to 3 K at VBE. The calculation of p- and n-type κ_{el} gives T and $T^{3/2}$ dependence. p-type electronic thermoelectric figure of merit ZT_{el} is very large at ultra-low temperatures (3 K-15 K) results from small κ_{el} . According to the calculations, ZT_{el} approximately equals to 1.41 at the VBE. One can see from Figure 5.4, ZT_{el} value is around 2 at the VBE. The deviation stems from the fact that transmission spectra of BO at the VBE is not an exact step function. Nevertheless, intersection of the ZT_{el} curves at the VBE confirmed the analytical result.

Combining the electronic and phononic transport properties we can obtain ZT . More interestingly, p-type ZT is increasing from 100 K to 47 K and then decreasing as T goes to zero. This seems incompatible with the p-type PF which decreases with the temperature drop. Therefore, the key quantities that lead to extraordinary ZT are κ_{el} and κ_{ph} . This will be further discussed after investigating the TE properties of BS monolayer.

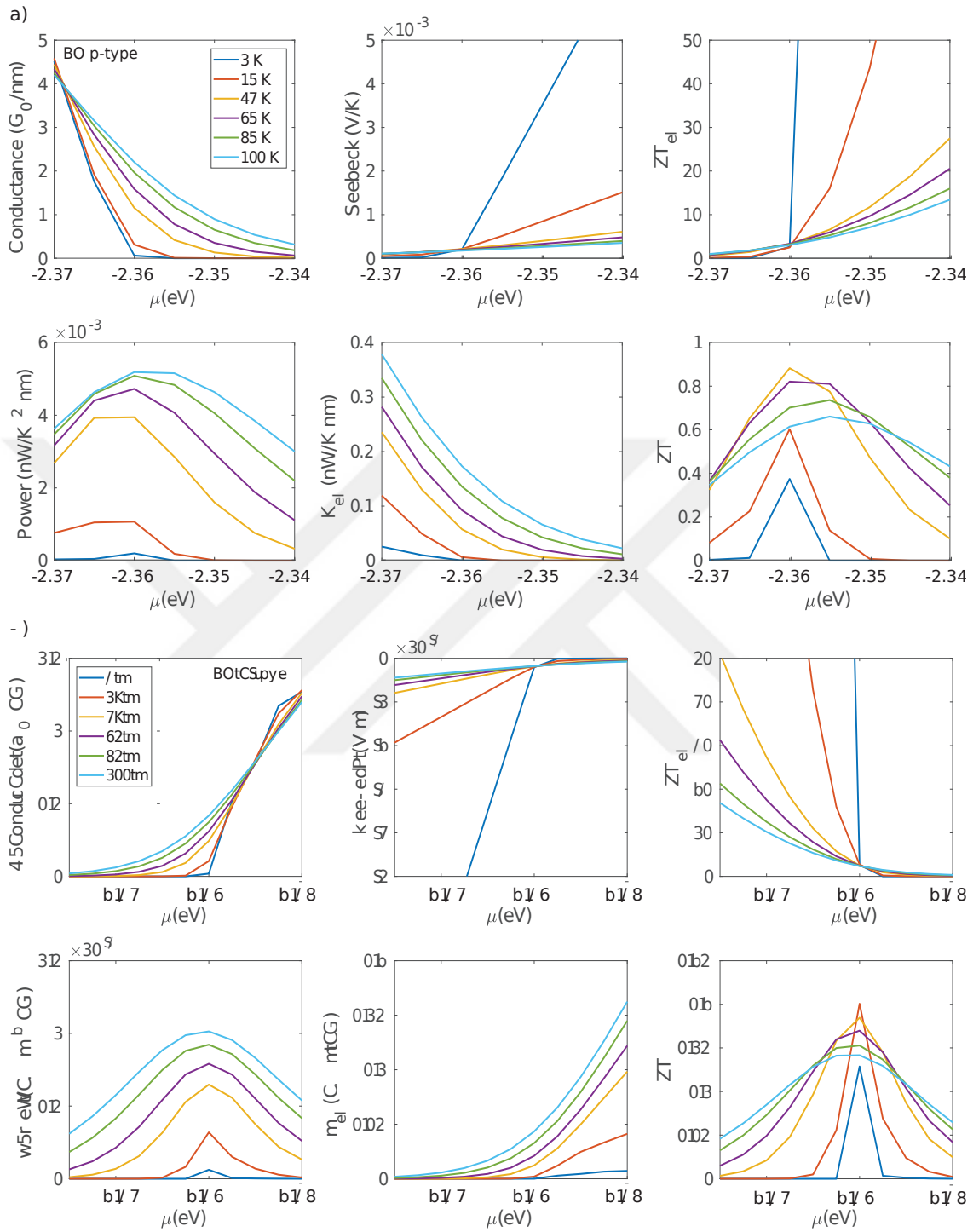


Figure 5.4. n-type and p-type ballistic thermoelectric coefficients of BO monolayer under 100 K.

Similarly, n-type ZT enhances with the reduction of temperature and this increase is maintained up to 17 K. This behaviour is unexpected for quadratic bands which exhibit \sqrt{E} -dependent transmission spectra. Turning our discussion to the τ_{el} spectra (see Figure 5.1(b) and c)) of BO and BS, one may realize that variation of their τ_{el} are not sufficiently slow at CBE. For example, in InSe, τ_{el} at the CBE is slowly increasing due to the absence of the valley degeneracy and pure parabolic character around Γ point. Thus, n-type TE properties of BO show a different behaviour from derived TE coefficients for pure quadratic dispersion.

As for the BS, TE properties similar to that of BO. Intersection of the p-type G , S and ZT_{el} curves is occurred at VBE (-1.43 eV) as plotted in Figure 5.5(a). p- and n-type PF dependencies of temperature are obviously different from each other. The p-type PF has almost same values at 100 K, 75 K and 45 K that verifies our theoretical prediction at relatively high temperatures. The underlying reason can be attributed to τ_{el} of BS at VBE is more close the step function compared to BO. Maximum p-type ZT peak is observed at $T = 15$ K while n-type ZT peak is achieved at $T = 11$ K.

In order to gain deep understanding about low temperature thermoelectrics, we need to investigate how κ_{ph}/κ_{el} ratio changes with T as can be seen from explicit expression of ZT in Eq. 5.19 and Eq. 5.31. In order to determine, whether this behaviour is originated from quartic dispersion, we consider MoS_2 having a quadratic dispersion. κ_{ph}/κ_{el} for MoS_2 increases with the decreasing temperature, leading to descending ZT as expected. However BO and BS exhibit strikingly different behaviour compared to MoS_2 as demonstrated in Figure. 5.6. Ratio of κ_{ph}/κ_{el} for both BO and BS decreases with the decreasing temperature which results in boost in ZT . However, κ_{ph}/κ_{el} of BS is larger than that of BO until temperature drops below 20 K, leading poor TE efficiency compared to BO. In the case of MoS_2 , κ_{ph}/κ_{el} rises with decreasing temperature until around 20 K which results in reduction in ZT . Also higher values of that ratio reduce the TE performance of MoS_2 at low temperatures.

- **Derivation of the TE Coefficients for Step-like Transmission Spectra**

Electronic transmission spectrum takes step function form in the lowest order approximation,

$$\tau(E) = \frac{2k_c a}{\pi} \theta(E_v - E) \quad (5.1)$$

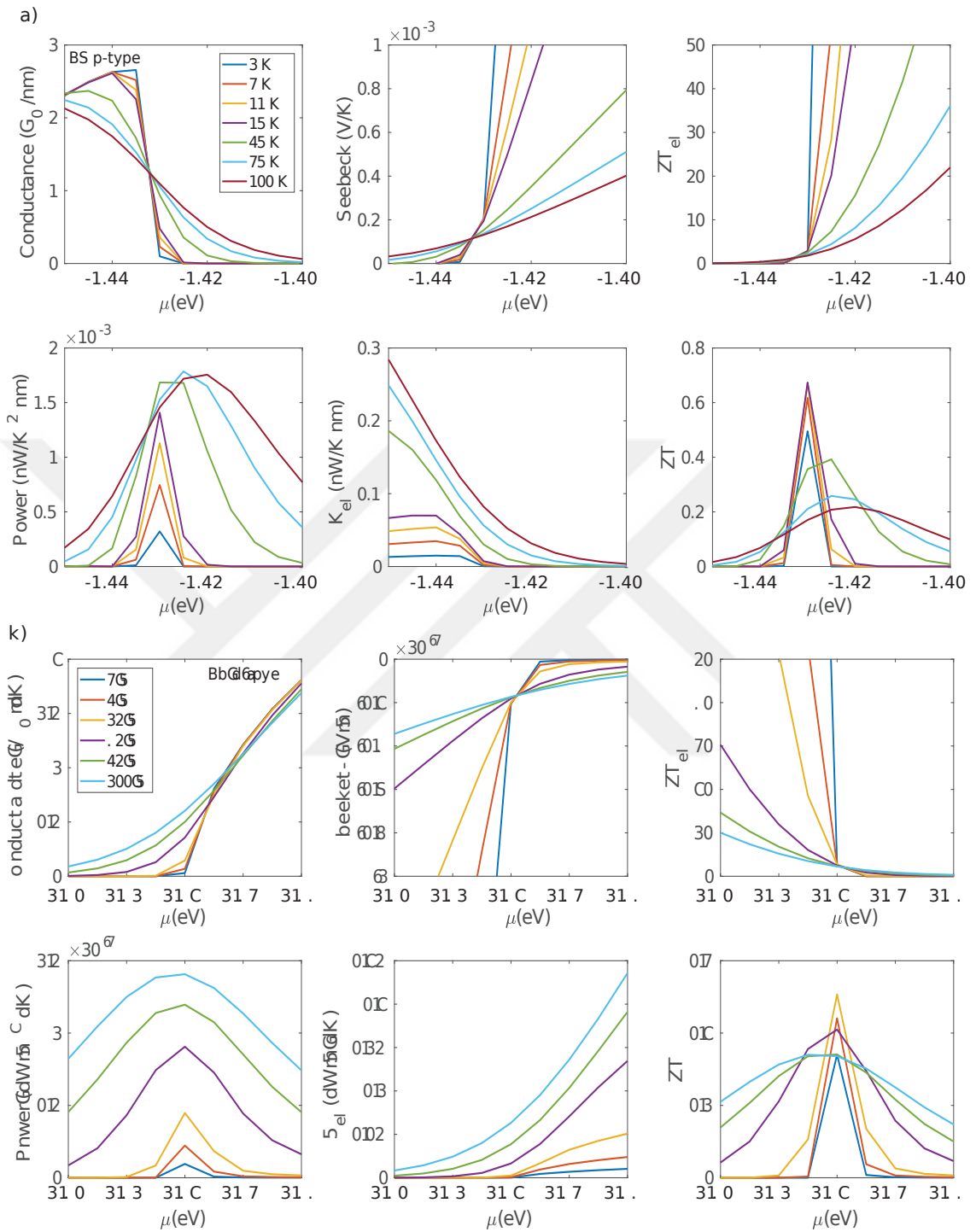


Figure 5.5. n-type and p-type ballistic thermoelectric coefficients of BS monolayer under 100 K.

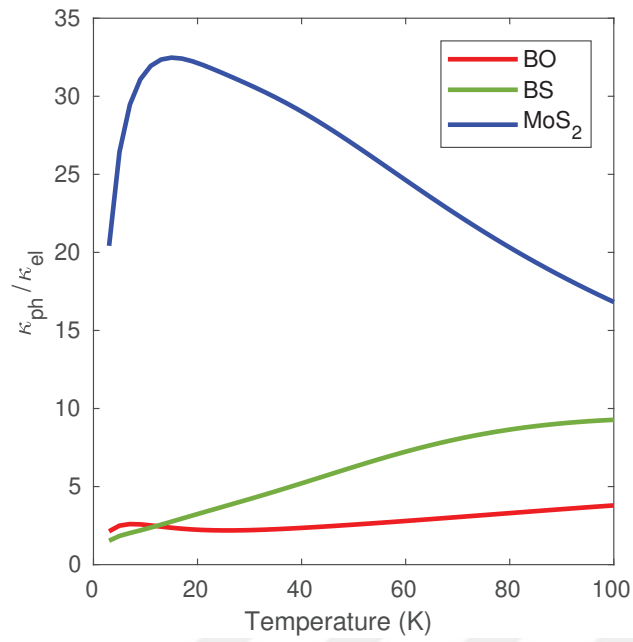


Figure 5.6. The ratio between phononic and electronic contributions to the thermal conductance of BO, BS and MoS₂ monolayers in a temperature range from 3 K to 100 K.

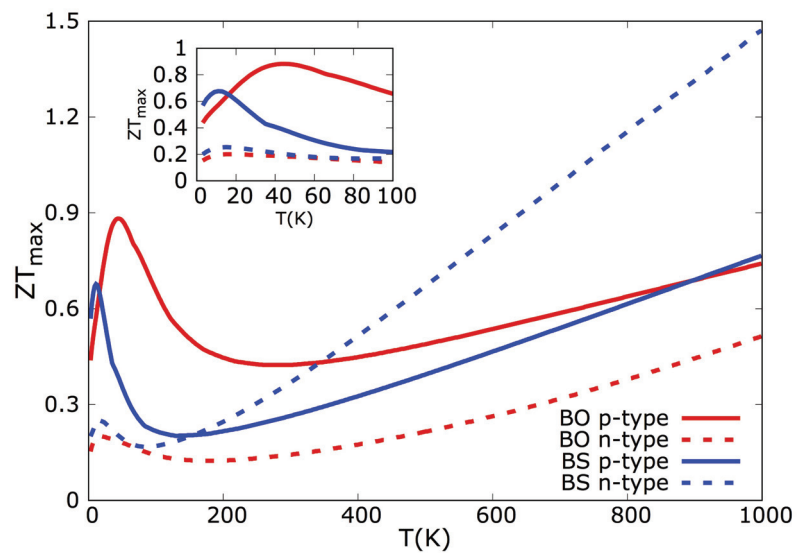


Figure 5.7. Phonon dispersion, transmission spectrum and the thermal conductance of BO and BS structures. Red and blue lines indicate that BO and BS monolayers respectively.

$T(E)$ is mainly determined by k_c and a . We start by calculating the L_n integrals

$$L_n(\mu, T) = -\frac{2}{h} \int dE \frac{\partial f}{\partial E} (E - \mu)^n \tau(E) \quad (5.2)$$

Fermi-Dirac distribution function,

$$f(E) = \frac{1}{e^{E/k_B T} + 1} = \frac{1}{e^x + 1} \quad (5.3)$$

where $x = E/k_B T$. Fermi window function,

$$\frac{\partial f}{\partial E} = -\frac{1}{k_B T} \frac{e^x}{(e^x + 1)^2} \quad (5.4)$$

The chemical potential μ at the VBE is set to zero. Zeroth power of L integrals results in,

$$L_0 = -\frac{2}{h} \frac{2k_c a}{\pi} \int k_B T \left(-\frac{1}{k_B T} \right) \frac{e^x}{(e^x + 1)^2} dx \quad (5.5)$$

$$= \frac{2k_c a}{\pi h} \quad (5.6)$$

It is seen that L_0 is independent of temperature. Its value depends only on the k_c and a of the structure. One finds first power of the L integrals,

$$L_1 = \frac{4k_c a}{\pi h} k_B T \int x \frac{e^x}{(e^x + 1)^2} dx \quad (5.7)$$

$$= -\frac{4 \ln 2 k_c a k_B T}{\pi h} \quad (5.8)$$

L_1 exhibit linear T dependence.

$$L_2 = \frac{4k_c a}{\pi h} k_B^2 T^2 \int x^2 \frac{e^x}{(e^x + 1)^2} dx \quad (5.9)$$

$$= \frac{2k_c a \pi}{3h} k_B^2 T^2 \quad (5.10)$$

Finally we can evaluate TE coefficients at the VBE. Electronic conductance becomes,

$$G_0 = e^2 L_0 \quad (5.11)$$

$$= \frac{2e^2 k_c a}{\pi h} \quad (5.12)$$

Since, G_0 includes only L_0 integral there is no T dependence.

$$S = \frac{1}{eT} \left(\frac{L_1}{L_0} \right) \quad (5.13)$$

$$= -2 \ln 2 \frac{k_B}{e} = 0.119 \text{ meV/K} \quad (5.14)$$

κ_{el} is obtained as,

$$\kappa_{el} = \frac{1}{T} \left(L_2 - \frac{L_1^2}{L_0} \right) \quad (5.15)$$

$$= \frac{2k_c a \pi k_B^2}{h} \left[\frac{1}{3} - \frac{4(\ln 2)^2}{\pi} \right] T \quad (5.16)$$

κ_{el} exhibits linear T dependence. Electronic thermoelectric figure of merit ZT_{el} which is described as

$$ZT_{el} = \frac{S^2 G}{\kappa_{el}} T \quad (5.17)$$

$$= \frac{1}{\frac{\pi^2}{12(\ln 2)^2} - 1} = 1.405 \quad (5.18)$$

is found dimensionless. Finally thermoelectric figure of merit ZT ,

$$ZT = ZT_{el} \frac{1}{1 + \frac{\kappa_{ph}}{\kappa_{el}}} \quad (5.19)$$

ZT is determined by κ_{ph}/κ_{el} ratio.

- **Derivation of the TE Coefficients for Square Root Transmission Spectra**

For quadratic bands which have $E(\mathbf{k}) \propto \mathbf{k}^2$ energy-momentum relation, electronic

transmission spectra depends on square root of the energy as $\tau_{el}(E) \propto \sqrt{E}$. When the same calculations are performed, the resulting L_n integrals take the following forms,

$$L_0 = \frac{2}{h}(k_B T)^{1/2} I_0 \quad (5.20)$$

$$L_1 = \frac{2}{h}(k_B T)^{3/2} I_1 \quad (5.21)$$

$$L_2 = \frac{2}{h}(k_B T)^{5/2} I_2 \quad (5.22)$$

where I_0 , I_1 and I_2

$$I_0 = \int_0^\infty x^{1/2} \frac{e^x}{(e^x + 1)^2} \quad (5.23)$$

$$I_1 = \int_0^\infty x^{3/2} \frac{e^x}{(e^x + 1)^2} \quad (5.24)$$

$$I_2 = \int_0^\infty x^{5/2} \frac{e^x}{(e^x + 1)^2} \quad (5.25)$$

$$(5.26)$$

Electronic conductance for quadratic bands becomes

$$G = \frac{2e^2 I_0 k_B^{1/2}}{h} T^{1/2} \quad (5.27)$$

$$S = \frac{k_B I_1}{e I_0} = 0.165 \text{meV/K} \quad (5.28)$$

$$\kappa_{el} = \frac{2}{h} k_B^{5/2} \left(I_2 - \frac{I_1^2}{I_0} \right) T^{3/2} \quad (5.29)$$

ZT_{el} can be derived from the $ZT_{el} = (S^2G/\kappa_{el})T$

$$ZT_{el} = \frac{1}{\frac{I_2 I_0}{I_1^2} - 1} = 2.03 \quad (5.30)$$

Likewise, the ZT takes the form

$$ZT = ZT_{el} \frac{1}{1 + \frac{\kappa_{ph}}{\kappa_{el}}} \quad (5.31)$$

Figure 5.7 displays maximum p- and n-type ZT_{max} as a function of temperature for BO and BS. The variation of ZT_{max} is investigated in a wide range temperature from 3 K to 1000 K. ZT_{max} is positioned at VBE with a value 0.88 is achieved at 47 K for BO monolayer. BS has smaller p-type ZT 0.68 at 15 K. Despite the larger average atomic mass and lower κ_{ph} of BS, BO possesses larger ZT_{max} . Both structure exhibit quartic dispersion in their uppermost valence band, however degenerate valence band maxima of BS shift towards to Γ therefore, valence band of BS is more close to pure quartic character. This fact reveals that TE performance at low temperatures is dominantly determined by κ_{ph}/κ_{el} ratio. For BO and BS, maximum n-type ZT_{max} values are obtained 0.20 and 0.25 at 17 K and 15 K respectively. Although n-type ZT_{max} values are 3-4 times smaller than those of p-type values, they show similar behavior. It should be noted that BS exhibit very large n-type ZT_{max} at high temperatures due to valley degeneracy at its conduction band. As a result BO and BS monolayers are promising TE materials for both low and high temperatures.

CHAPTER 6

CONCLUSION

In summary, we have investigated structural, electronic, vibrational, as well as ballistic transport and thermoelectric properties of a large number of two dimensional single layer materials by using a combination of first-principles calculations and Landauer formalism.

First, transition metal dichalcogenides (TMDs) and oxides (TMOs) are discussed in 2H- and 1T-phases. For 26 semiconducting and dynamically stable TMDs/TMOs, band structures and vibrational spectrums are presented by means of density functional calculations. These DFT results served as inputs for calculating ballistic transport and thermoelectric properties. We have identified promising thermoelectric materials which possess high ZT values close to or above 1 at room temperature. Our calculations reveal that two TMO monolayer 1T-ZrO₂ and 1T-HfO₂ are promising p-type thermoelectric candidates at room temperature. 2H-phase of ZrSe₂ HfS₂ and HfSe₂ achieve larger p- and n-type ZT compared to those of 1T phase resulting from difference between electronic transmission spectrum around Fermi energy. Furthermore, hybrid functionals are employed for five selected TMDs which are expected to be mostly affected because of their narrow electronic band gaps. Anomaly in ZT values of these TMDs are corrected with the increase of band gap, resulting in enhanced TE efficiency at high temperatures. Second, we have systematically studied the ballistic transport and thermoelectric properties of group III-monochalcogenides (group III-VI) which consists of 25 compounds in a $P\bar{6}m2$ (α) symmetry group. Group III-monochalcogenides have unique outermost valence band structure which offers quartic dispersion also called as "Mexican Hat Shape". Mexican hat feature results in strong inverse-square-root singularities in the density of states and hence step-like transmission spectra near the valence band edge. Sharp change in transmission spectra near the valence band edge leads to boost in Seebeck coefficient and hence thermoelectric figure of merit p-type ZT . 13 group III-VI monolayer possess p-type ZT above 1 at room temperature. In addition, synergistic combination of flatness and valley degeneracy in conduction band bring an advantage regarding high thermoelectric efficiency. Therefore, III-VI compounds which exhibit above mentioned features show considerable thermoelectric performance. This is a signature that group III-monochalcogenides can be used as both n- and p-type materials in thermoelectric devices. Surprisingly, p-type ZT

values of BO and BS monolayers from group III-VI, reach 0.88 and 0.68 respectively below 50 K. At the same time n-type maximum ZT values of 0.20 and 0.25 are achieved at under 20 K for both materials. When ratio of the phononic thermal conductance and electronic contribution to the thermal conductance of BO and BS are very different compared to that of MoS_2 due to the peculiar behaviour of transmission spectrum and low thermal conductance at low temperatures. As a result BO and BS monolayers are promising candidates for low temperature thermoelectric applications.



REFERENCES

- Adessi, C., S. Thebaud, R. Bouzerar, and G. Bouzerar (2017). First principle investigation on thermoelectric properties of transition metal dichalcogenides: Beyond the rigid band model. *The Journal of Physical Chemistry C* 121(23), 12577–12584.
- Aminalragia-Giamini, S., J. Marquez-Velasco, P. Tsipas, D. Tsoutsou, G. Renaud, and A. Dimoulas (2017). Molecular beam epitaxy of thin hftfe 2 semimetal films. *2D Materials* 4(1), 015001.
- Amollo, T. A., G. T. Mola, M. S. K. Kirui, and V. O. Nyamori (2018). Graphene for thermoelectric applications: Prospects and challenges. *Critical Reviews in Solid State and Materials Sciences* 43(2), 133–157.
- Anno, Y., Y. Imakita, K. Takei, S. Akita, and T. Arie (2017). Enhancement of graphene thermoelectric performance through defect engineering. *2D Materials* 4(2), 025019.
- Anno, Y., K. Takei, S. Akita, and T. Arie (2015). Enhancing the thermoelectric device performance of graphene using isotopes and isotopic heterojunctions. *Advanced Electronic Materials* 1(9), 1500175.
- Antonius, G., D. Y. Qiu, and S. G. Louie (2018, Mar). Orbital symmetry and the optical response of single-layer mx monochalcogenides. *Nano Letters* 18(3), 1925–1929.
- Arab, A. and Q. Li (2015, Sep). Anisotropic thermoelectric behavior in armchair and zigzag mono- and fewlayer mos2 in thermoelectric generator applications. *Scientific Reports* 5, 13706 EP –. Article.
- Ataca, C., H. Sahin, and S. Ciraci (2012, Apr). Stable, single-layer mx2 transition-metal oxides and dichalcogenides in a honeycomb-like structure. *The Journal of Physical Chemistry C* 116(16), 8983–8999.
- Babaei, H., J. M. Khodadadi, and S. Sinha (2014). Large theoretical thermoelectric power factor of suspended single-layer mos2. *Applied Physics Letters* 105(19), 193901.
- Bahuguna, B. P., L. K. Saini, R. O. Sharma, and B. Tiwari (2018). Hybrid functional

- calculations of electronic and thermoelectric properties of gas, gase, and gate monolayers. *Phys. Chem. Chem. Phys.* 20, 28575–28582.
- Balandin, A. A. (2011, July). Thermal properties of graphene and nanostructured carbon materials. *Nature Materials* 10(8), 569–581.
- Baroni, S., S. de Gironcoli, A. Dal Corso, and P. Giannozzi (2001, Jul). Phonons and related crystal properties from density-functional perturbation theory. *Rev. Mod. Phys.* 73, 515–562.
- Ben Aziza, Z., V. Zólyomi, H. Henck, D. Pierucci, M. G. Silly, J. Avila, S. J. Magorrian, J. Chaste, C. Chen, M. Yoon, K. Xiao, F. Sirotti, M. C. Asensio, E. Lhuillier, M. Eddrief, V. I. Fal’ko, and A. Ouerghi (2018, Sep). Valence band inversion and spin-orbit effects in the electronic structure of monolayer gase. *Phys. Rev. B* 98, 115405.
- Broido, D. A. and T. L. Reinecke (1995). Thermoelectric figure of merit of quantum wire superlattices. *Applied Physics Letters* 67(1), 100–102.
- Cai, Y., J. Lan, G. Zhang, and Y.-W. Zhang (2014, Jan). Lattice vibrational modes and phonon thermal conductivity of monolayer mos₂. *Phys. Rev. B* 89, 035438.
- Callister, W. and D. Rethwisch (2013). *Materials Science and Engineering: An Introduction, 9th Edition: Ninth Edition*. John Wiley and Sons, Incorporated.
- Capelle, K. (2002, Nov). A bird’s-eye view of density-functional theory. *arXiv e-prints*, cond-mat/0211443.
- Ceperley, D. M. and B. J. Alder (1980, Aug). Ground state of the electron gas by a stochastic method. *Phys. Rev. Lett.* 45, 566–569.
- Chang, X., H. Li, and G. Tang (2019). Tensile mechanical properties and fracture behavior of monolayer inse under axial tension. *Computational Materials Science* 158, 340 – 345.
- Chen, C., B. Singh, H. Lin, and V. M. Pereira (2018, Nov). Reproduction of the charge density wave phase diagram in 1t-tise₂ exposes its excitonic character. *Phys. Rev. Lett.* 121, 226602.

- Chen, K.-X., X.-M. Wang, D.-C. Mo, and S.-S. Lyu (2015). Thermoelectric properties of transition metal dichalcogenides: From monolayers to nanotubes. *The Journal of Physical Chemistry C* 119(47), 26706–26711.
- Cherednichenko, K. A., I. A. Kruglov, A. R. Oganov, Y. Le Godec, M. Mezouar, and V. L. Solozhenko (2018). Boron monosulfide: Equation of state and pressure-induced phase transition. *Journal of Applied Physics* 123(13), 135903.
- Cutler, M. and N. F. Mott (1969, May). Observation of anderson localization in an electron gas. *Phys. Rev.* 181, 1336–1340.
- Daeneke, T., P. Atkin, R. Orrell-Trigg, A. Zavabeti, T. Ahmed, S. Walia, M. Liu, Y. Tachibana, M. Javid, A. D. Greentree, S. P. Russo, R. B. Kaner, and K. Kalantar-Zadeh (2017, Nov). Wafer-scale synthesis of semiconducting sno monolayers from interfacial oxide layers of metallic liquid tin. *ACS Nano* 11(11), 10974–10983.
- Das, S., G. Shi, N. Sanders, and E. Kioupakis (2018, Oct). Electronic and optical properties of two-dimensional a-pbo from first principles. *Chemistry of Materials* 30(20), 7124–7129.
- Dehkordi, A. M., M. Zebarjadi, J. He, and T. M. Tritt (2015). Thermoelectric power factor: Enhancement mechanisms and strategies for higher performance thermoelectric materials. *Materials Science and Engineering: R: Reports* 97, 1 – 22.
- Demirci, S., N. Avazl 1, E. Durgun, and S. Cahangirov (2017, Mar). Structural and electronic properties of monolayer group iii monochalcogenides. *Phys. Rev. B* 95, 115409.
- Dimple, N. Jena, and A. D. Sarkar (2017). Compressive strain induced enhancement in thermoelectric-power-factor in monolayer mos 2 nanosheet. *Journal of Physics: Condensed Matter* 29(22), 225501.
- Ding, G., G. Y. Gao, Z. Huang, W. Zhang, and K. Yao (2016). Thermoelectric properties of monolayer m se 2 (m = zr, hf): low lattice thermal conductivity and a promising figure of merit. *Nanotechnology* 27(37), 375703.
- Dollfus, P., V. H. Nguyen, and J. Saint-Martin (2015). Thermoelectric effects in graphene

- nanostructures. *Journal of Physics: Condensed Matter* 27(13), 133204.
- Dragoman, D. and M. Dragoman (2007). Giant thermoelectric effect in graphene. *Applied Physics Letters* 91(20), 203116.
- Dresselhaus, M., G. Chen, M. Tang, R. Yang, H. Lee, D. Wang, Z. Ren, J.-P. Fleurial, and P. Gogna (2007). New directions for low-dimensional thermoelectric materials. *Advanced Materials* 19(8), 1043–1053.
- D'Souza, R. and S. Mukherjee (2018). Enhancement of thermoelectric figure-of-merit of graphene upon bn-doping and sample length reduction. *Journal of Applied Physics* 124(12), 124301.
- Duong, D. L., M. Burghard, and J. C. Schön (2015, Dec). Ab initio computation of the transition temperature of the charge density wave transition in TiSe_2 . *Phys. Rev. B* 92, 245131.
- Esfarjani, K., M. Zebarjadi, and Y. Kawazoe (2006, Feb). Thermoelectric properties of a nanocontact made of two-capped single-wall carbon nanotubes calculated within the tight-binding approximation. *Phys. Rev. B* 73, 085406.
- Fan, D., C. Yang, S. Lu, and X. Hu (2018, March). Two-dimensional Boron Monosulfides: Semiconducting and Metallic Polymorphs. *arXiv e-prints*.
- Gerald Mahan, Brian Sales, J. S. (1997). Thermoelectric materials: New approaches to an old problem. *PHYSICS TODAY* 50, 42.
- Ghahari, F., H.-Y. Xie, T. Taniguchi, K. Watanabe, M. S. Foster, and P. Kim (2016, Mar). Enhanced thermoelectric power in graphene: Violation of the mott relation by inelastic scattering. *Phys. Rev. Lett.* 116, 136802.
- Gong, C., H. Zhang, W. Wang, L. Colombo, R. M. Wallace, and K. Cho (2013). Band alignment of two-dimensional transition metal dichalcogenides: Application in tunnel field effect transistors. *Applied Physics Letters* 103(5), 053513.
- G.S. Nolas, J. Sharp, J. G. (2001). *Thermoelectrics*. Springer-Verlag Berlin Heidelberg.

- Guinea, F., A. H. Castro Neto, and N. M. R. Peres (2006, Jun). Electronic states and Landau levels in graphene stacks. *Phys. Rev. B* 73, 245426.
- Gunst, T., T. Markussen, A.-P. Jauho, and M. Brandbyge (2011, Oct). Thermoelectric properties of finite graphene antidot lattices. *Phys. Rev. B* 84, 155449.
- Guo, S.-D. (2016). Spin-orbit and strain effect on power factor in monolayer MoS_2 . *Computational Materials Science* 123, 8 – 13.
- Guo, S.-D. and J.-L. Wang (2016). Spin-orbital coupling effect on the power factor in semiconducting transition-metal dichalcogenide monolayers. *Semiconductor Science and Technology* 31(9), 095011.
- Guttman, G. D., E. Ben-Jacob, and D. J. Bergman (1995, Jun). Thermopower of mesoscopic and disordered systems. *Phys. Rev. B* 51, 17758–17766.
- Henkelman, G., A. Arnaldsson, and H. Jónsson (2006). A fast and robust algorithm for Bader decomposition of charge density. *Computational Materials Science* 36(3), 354 – 360.
- Hicks, L. D. and M. S. Dresselhaus (1993a, May). Effect of quantum-well structures on the thermoelectric figure of merit. *Phys. Rev. B* 47, 12727–12731.
- Hicks, L. D. and M. S. Dresselhaus (1993b, Jun). Thermoelectric figure of merit of a one-dimensional conductor. *Phys. Rev. B* 47, 16631–16634.
- Hicks, L. D., T. C. Harman, X. Sun, and M. S. Dresselhaus (1996, Apr). Experimental study of the effect of quantum-well structures on the thermoelectric figure of merit. *Phys. Rev. B* 53, R10493–R10496.
- Hippalgaonkar, K., Y. Wang, Y. Ye, D. Y. Qiu, H. Zhu, Y. Wang, J. Moore, S. G. Louie, and X. Zhang (2017, Mar). High thermoelectric power factor in two-dimensional crystals of MoS_2 . *Phys. Rev. B* 95, 115407.
- Hohenberg, P. and W. Kohn (1964, Nov). Inhomogeneous electron gas. *Phys. Rev.* 136, B864–B871.

- Hong, J., C. Lee, J.-S. Park, and J. H. Shim (2016, Jan). Control of valley degeneracy in MoS_2 by layer thickness and electric field and its effect on thermoelectric properties. *Phys. Rev. B* 93, 035445.
- Hu, P., Z. Wen, L. Wang, P. Tan, and K. Xiao (2012, Jul). Synthesis of few-layer gase nanosheets for high performance photodetectors. *ACS Nano* 6(7), 5988–5994.
- Huang, W., H. Da, and G. Liang (2013). Thermoelectric performance of mx_2 ($m=\text{mo,w}; x=\text{s,se}$) monolayers. *Journal of Applied Physics* 113(10), 104304.
- Huang, W., L. Gan, H. Li, Y. Ma, and T. Zhai (2016). 2d layered group iiiA metal chalcogenides: synthesis, properties and applications in electronics and optoelectronics. *CrystEngComm* 18, 3968–3984.
- Huang, W., X. Luo, C. K. Gan, S. Y. Quek, and G. Liang (2014). Theoretical study of thermoelectric properties of few-layer mos_2 and wse_2 . *Physical Chemistry Chemical Physics* 16(22), 10866–10874.
- Hung, N. T., A. R. T. Nugraha, and R. Saito (2017). Two-dimensional inSe as a potential thermoelectric material. *Applied Physics Letters* 111(9), 092107.
- Jiang, J.-W., J.-S. Wang, and B. Li (2009, May). Thermal conductance of graphene and dimerite. *Phys. Rev. B* 79, 205418.
- Jin, Z., Q. Liao, H. Fang, Z. Liu, W. Liu, Z. Ding, T. Luo, and N. Yang (2015, Dec). A revisit to high thermoelectric performance of single-layer mos_2 . *Scientific Reports* 5, 18342 EP –. Article.
- Kayyalha, M., J. Maassen, M. Lundstrom, L. Shi, and Y. P. Chen (2016). Gate-tunable and thickness-dependent electronic and thermoelectric transport in few-layer mos_2 . *Journal of Applied Physics* 120(13), 134305.
- Kresse, G. and J. Furthmüller (1996, Oct). Efficient iterative schemes for ab initio total-energy calculations using a plane-wave basis set. *Phys. Rev. B* 54, 11169–11186.
- Kresse, G. and D. Joubert (1999, Jan). From ultrasoft pseudopotentials to the projector augmented-wave method. *Phys. Rev. B* 59, 1758–1775.

- Kumar, P., J. Liu, P. Ranjan, Y. Hu, S. S. Yamijala, S. K. Pati, J. Irudayaraj, and G. J. Cheng (2018). Alpha lead oxide (-pbo): A new 2d material with visible light sensitivity. *Small* 14(12), 1703346.
- Kumar, S. and U. Schwingenschlögl (2015). Thermoelectric response of bulk and monolayer mose2 and wse2. *Chemistry of Materials* 27(4), 1278–1284.
- Late, D. J., B. Liu, J. Luo, A. Yan, H. S. S. R. Matte, M. Grayson, C. N. R. Rao, and V. P. Dravid (2012). Gas and gase ultrathin layer transistors. *Advanced Materials* 24(26), 3549–3554.
- Lei, S., L. Ge, Z. Liu, S. Najmaei, G. Shi, G. You, J. Lou, R. Vajtai, and P. M. Ajayan (2013, Jun). Synthesis and photoresponse of large gase atomic layers. *Nano Letters* 13(6), 2777–2781.
- Li, X., M.-W. Lin, A. A. Puretzky, J. C. Idrobo, C. Ma, M. Chi, M. Yoon, C. M. Rouleau, I. I. Kravchenko, D. B. Geohegan, and K. Xiao (2014, Jun). Controlled vapor phase growth of single crystalline, two-dimensional gase crystals with high photoresponse. *Scientific Reports* 4, 5497 EP –. Article.
- Lin, L., Y.-F. Zhang, H.-B. Liu, J.-H. Meng, W.-H. Chen, and X.-D. Wang (2019). A new configuration design of thermoelectric cooler driven by thermoelectric generator. *Applied Thermal Engineering* 160, 114087.
- Liu, F., H. Shimotani, H. Shang, T. Kanagasekaran, V. Zólyomi, N. Drummond, V. I. Fal'ko, and K. Tanigaki (2014, Jan). High-sensitivity photodetectors based on multilayer gate flakes. *ACS Nano* 8(1), 752–760.
- Liu, Y.-Y., Y.-J. Zeng, P.-Z. Jia, X.-H. Cao, X. Jiang, and K.-Q. Chen (2018). An efficient mechanism for enhancing the thermoelectricity of nanoribbons by blocking phonon transport in 2d materials. *Journal of Physics: Condensed Matter* 30(27), 275701.
- Longuinhas, R. and J. Ribeiro-Soares (2019, Feb). Monitoring the applied strain in monolayer gallium selenide through vibrational spectroscopies: A first-principles investigation. *Phys. Rev. Applied* 11, 024012.
- Lv, H., W. Lu, X. Luo, H. Lu, X. Zhu, and Y. Sun (2016). Enhancing the thermoelectric

performance of a hfs2 monolayer through valley engineering. *arXiv preprint*.

Lv, H. Y., W. J. Lu, D. F. Shao, H. Y. Lu, and Y. P. Sun (2016). Strain-induced enhancement in the thermoelectric performance of a zrs2 monolayer. *J. Mater. Chem. C* 4, 4538–4545.

Ma, Y., Y. Dai, M. Guo, L. Yu, and B. Huang (2013). Tunable electronic and dielectric behavior of gas and gase monolayers. *Phys. Chem. Chem. Phys.* 15, 7098–7105.

Maeso, D., S. Pakdel, H. Santos, N. Agraït, J. J. Palacios, E. Prada, and G. Rubio-Bollinger (2019, mar). Strong modulation of optical properties in rippled 2d GaSe via strain engineering. *Nanotechnology* 30(24), 24LT01.

Mahan, G. D. and H. B. Lyon (1994). Thermoelectric devices using semiconductor quantum wells. *Journal of Applied Physics* 76(3), 1899–1901.

Mao, J., H. Zhu, Z. Ding, Z. Liu, G. A. Gamage, G. Chen, and Z. Ren (2019). High thermoelectric cooling performance of n-type mg3bi2-based materials.

Martin, R. M. (2004). *Electronic Structure Basic Theory and Practical Methods*. Cambridge University Press.

Mazzamuto, F., V. Hung Nguyen, Y. Apertet, C. Caër, C. Chassat, J. Saint-Martin, and P. Dollfus (2011, Jun). Enhanced thermoelectric properties in graphene nanoribbons by resonant tunneling of electrons. *Phys. Rev. B* 83, 235426.

Min, H., B. Sahu, S. K. Banerjee, and A. H. MacDonald (2007, Apr). Ab initio theory of gate induced gaps in graphene bilayers. *Phys. Rev. B* 75, 155115.

Mingo, N. and D. A. Broido (2005, Aug). Carbon nanotube ballistic thermal conductance and its limits. *Phys. Rev. Lett.* 95, 096105.

Mleczko, M. J., C. Zhang, H. R. Lee, H.-H. Kuo, B. Magyari-Köpe, R. G. Moore, Z.-X. Shen, I. R. Fisher, Y. Nishi, and E. Pop (2017). Hfse2 and zrse2: Two-dimensional semiconductors with native high- oxides. *Science Advances* 3(8).

Monkhorst, H. J. and J. D. Pack (1976, Jun). Special points for brillouin-zone integrations.

Phys. Rev. B 13, 5188–5192.

Mortazavi, B. and T. Rabczuk (2018). Boron monochalcogenides; stable and strong two-dimensional wide band-gap semiconductors. *Energies* 11(6).

Mudd, G. W., S. A. Svatek, T. Ren, A. Patanè, O. Makarovskiy, L. Eaves, P. H. Beton, Z. D. Kovalyuk, G. V. Lashkarev, Z. R. Kudrynskiy, and A. I. Dmitriev (2013). Tuning the bandgap of exfoliated inorganic nanosheets by quantum confinement. *Advanced Materials* 25(40), 5714–5718.

Nakamura, K. (2018). First-principles simulation on thermoelectric properties of transition metal dichalcogenide monolayers. *Japanese Journal of Applied Physics* 57(6S1), 06HE04.

Nissimagoudar, A. S., J. Ma, Y. Chen, and W. Li (2017, jul). Thermal transport in monolayer InSe. *Journal of Physics: Condensed Matter* 29(33), 335702.

Ouyang, B., S. Chen, Y. Jing, T. Wei, S. Xiong, and D. Donadio (2018). Enhanced thermoelectric performance of two dimensional ms_2 ($m = mo, w$) through phase engineering. *Journal of Materiomics*.

Ouyang, Y. and J. Guo (2009). A theoretical study on thermoelectric properties of graphene nanoribbons. *Applied Physics Letters* 94(26), 263107.

Ouyang, Y., Y. Xie, Z. Zhang, Q. Peng, and Y. Chen (2016). Very high thermoelectric figure of merit found in hybrid transition-metal-dichalcogenides. *Journal of Applied Physics* 120(23), 235109.

Özdamar, B., G. Özbal, M. N. m. c. Çınar, K. Sevim, G. Kurt, B. Kaya, and H. Sevinçli (2018, Jul). Structural, vibrational, and electronic properties of single-layer hexagonal crystals of group iv and v elements. *Phys. Rev. B* 98, 045431.

Pandey, T., D. S. Parker, and L. Lindsay (2017, oct). Ab initio phonon thermal transport in monolayer InSe, GaSe, GaS, and alloys. *Nanotechnology* 28(45), 455706.

Perdew, J. P., K. Burke, and M. Ernzerhof (1996, Oct). Generalized gradient approximation made simple. *Phys. Rev. Lett.* 77, 3865–3868.

- Poudel, B., Q. Hao, Y. Ma, Y. Lan, A. Minnich, B. Yu, X. Yan, D. Wang, A. Muto, D. Vashaee, X. Chen, J. Liu, M. S. Dresselhaus, G. Chen, and Z. Ren (2008). High-thermoelectric performance of nanostructured bismuth antimony telluride bulk alloys. *Science* 320(5876), 634–638.
- Qin, D., X.-J. Ge, G.-q. Ding, G.-y. Gao, and J.-T. Lü (2017). Strain-induced thermoelectric performance enhancement of monolayer zrse₂. *RSC Adv.* 7, 47243–47250.
- R. P. CHASMAR, R. (1959). The thermoelectric figure of merit and its relation to thermoelectric generators. *Journal of Electronics and Control* 7, 52.
- Rasmussen, F. A. and K. S. Thygesen (2015). Computational 2d materials database: Electronic structure of transition-metal dichalcogenides and oxides. *The Journal of Physical Chemistry C* 119(23), 13169–13183.
- Rego, L. G. C. and G. Kirczenow (1998, Jul). Quantized thermal conductance of dielectric quantum wires. *Phys. Rev. Lett.* 81, 232–235.
- Rybkovskiy, D. V., A. V. Osadchy, and E. D. Obraztsova (2014, Dec). Transition from parabolic to ring-shaped valence band maximum in few-layer gas, gase, and inse. *Phys. Rev. B* 90, 235302.
- Saeed, Y., N. Singh, and U. Schwingenschlögl (2014). Thickness and strain effects on the thermoelectric transport in nanostructured bi₂se₃. *Applied Physics Letters* 104(3), 033105.
- Saito, K., J. Nakamura, and A. Natori (2007, Sep). Ballistic thermal conductance of a graphene sheet. *Phys. Rev. B* 76, 115409.
- Saji, K. J., K. Tian, M. Snure, and A. Tiwari (2016). 2d tin monoxide—an unexplored p-type van der waals semiconductor: Material characteristics and field effect transistors. *Advanced Electronic Materials* 2(4), 1500453.
- Samad, A., A. Shafique, and Y.-H. Shin (2017). Adsorption and diffusion of mono, di, and trivalent ions on two-dimensional tis₂. *Nanotechnology* 28(17), 175401.
- Sandonas, L. M., H. Sevinçli, R. Gutierrez, and G. Cuniberti (2018). First-principle-

- based phonon transport properties of nanoscale graphene grain boundaries. *Advanced Science* 5(2), 1700365.
- Seixas, L., A. S. Rodin, A. Carvalho, and A. H. Castro Neto (2016, May). Multiferroic two-dimensional materials. *Phys. Rev. Lett.* 116, 206803.
- Sevinçli, H. and G. Cuniberti (2010, Mar). Enhanced thermoelectric figure of merit in edge-disordered zigzag graphene nanoribbons. *Phys. Rev. B* 81, 113401.
- Sevinçli, H., C. Sevik, T. Çağın, and G. Cuniberti (2013, February). A bottom-up route to enhance thermoelectric figures of merit in graphene nanoribbons. *Scientific Reports* 3(1).
- Sevinçli, H., S. Roche, G. Cuniberti, M. Brandbyge, R. Gutierrez, and L. M. Sandonas (2019, apr). Green function, quasi-classical langevin and kubo–greenwood methods in quantum thermal transport. *Journal of Physics: Condensed Matter* 31(27), 273003.
- Sevinçli, H. (2017). Quartic dispersion, strong singularity, magnetic instability, and unique thermoelectric properties in two-dimensional hexagonal lattices of group-va elements. *Nano Letters* 17(4), 2589–2595. PMID: 28318269.
- Shangguan, H., L. Han, T. Zhang, R. Quhe, Q. Wang, S. Li, and P. Lu (2019, Sep). Thermoelectric properties of two-dimensional gallium telluride. *Journal of Electronic Materials* 48(9), 5988–5994.
- Shen, W., D. Zou, G. Nie, and Y. Xu (2017). Biaxial strain-induced enhancement in the thermoelectric performance of monolayer wse₂. *Chinese Physics B* 26(11), 117202.
- Singh, B., C.-H. Hsu, W.-F. Tsai, V. M. Pereira, and H. Lin (2017, Jun). Stable charge density wave phase in a 1t – –tise₂ monolayer. *Phys. Rev. B* 95, 245136.
- Snyder, G. J. (2004). Application of the compatibility factor to the design of segmented and cascaded thermoelectric generators. *Applied Physics Letters* 84(13), 2436–2438.
- Snyder, G. J. and A. H. Snyder (2017). Figure of merit zT of a thermoelectric device defined from materials properties. *Energy Environ. Sci.* 10, 2280–2283.

- Snyder, G. J. and E. S. Toberer (2008, Feb). Complex thermoelectric materials. *Nature Materials* 7, 105 EP –. Review Article.
- Snyder, G. J., E. S. Toberer, R. Khanna, and W. Seifert (2012, Jul). Improved thermoelectric cooling based on the thomson effect. *Phys. Rev. B* 86, 045202.
- Sofo, J. O. and G. D. Mahan (1994, Feb). Optimum band gap of a thermoelectric material. *Phys. Rev. B* 49, 4565–4570.
- Springborg, M. (2000). *Methods of Electronic-Structure Calculations: From Molecules to Solids*. Wiley; 1 edition (July 13, 2000).
- Stauber, T., N. M. R. Peres, F. Guinea, and A. H. Castro Neto (2007, Mar). Fermi liquid theory of a fermi ring. *Phys. Rev. B* 75, 115425.
- Sun, H., Z. Wang, and Y. Wang (2017). Band alignment of two-dimensional metal monochalcogenides mxs (m=ga,in; x=s,se,te). *AIP Advances* 7(9), 095120.
- T. Hung, N., A. R. T. Nugraha, T. Yang, Z. Zhang, and R. Saito (2019). Thermoelectric performance of monolayer inse improved by convergence of multivalley bands. *Journal of Applied Physics* 125(8), 082502.
- Toffoli, H. (2009). Lecture vii : The hohenberg-kohn theorem and the kohn-sham equations.
- Togo, A. and I. Tanaka (2015). First principles phonon calculations in materials science. *Scripta Materialia* 108, 1 – 5.
- Tsipas, P., D. Tsoutsou, S. Fragkos, R. Sant, C. Alvarez, H. Okuno, G. Renaud, R. Alcotte, T. Baron, and A. Dimoulas (2018). Massless dirac fermions in zrte2 semimetal grown on inas(111) by van der waals epitaxy. *ACS Nano* 12(2), 1696–1703.
- Wang, H., G. Qin, J. Yang, Z. Qin, Y. Yao, Q. Wang, and M. Hu (2019). First-principles study of electronic, optical and thermal transport properties of group iii–vi monolayer mx (m=ga, in; x=s, se). *Journal of Applied Physics* 125(24), 245104.
- Wang, R.-N., G.-Y. Dong, S.-F. Wang, G.-S. Fu, and J.-L. Wang (2017). Variations of

- thermoelectric performance by electric fields in bilayer mx_2 ($m = w, mo$; $x = s, se$). *Physical Chemistry Chemical Physics* 19(8), 5797–5805.
- Wang, Y., Q. Zhang, Q. Shen, Y. Cheng, U. Schwingenschlögl, and W. Huang (2017). Lead monoxide: a two-dimensional ferromagnetic semiconductor induced by hole-doping. *J. Mater. Chem. C* 5, 4520–4525.
- Wang, Z., R. Xie, C. T. Bui, D. Liu, X. Ni, B. Li, and J. T. L. Thong (2011). Thermal transport in suspended and supported few-layer graphene. *Nano Letters* 11(1), 113–118. PMID: 21142193.
- Wei, M. J., W. J. Lu, R. C. Xiao, H. Y. Lv, P. Tong, W. H. Song, and Y. P. Sun (2017, Oct). Manipulating charge density wave order in monolayer $1t - tise_2$ by strain and charge doping: A first-principles investigation. *Phys. Rev. B* 96, 165404.
- Wickramaratne, D., F. Zahid, and R. K. Lake (2014). Electronic and thermoelectric properties of few-layer transition metal dichalcogenides. *The Journal of Chemical Physics* 140(12), 124710.
- Wickramaratne, D., F. Zahid, and R. K. Lake (2015). Electronic and thermoelectric properties of van der waals materials with ring-shaped valence bands. *Journal of Applied Physics* 118(7), 075101.
- Witting, I. T., T. C. Chasapis, F. Ricci, M. Peters, N. A. Heinz, G. Hautier, and G. J. Snyder (2019). The thermoelectric properties of bismuth telluride. *Advanced Electronic Materials* 5(6), 1800904.
- Wu, T.-m., R.-x. Xu, X. Zheng, and W. Zhuang (2016). Electronic structures and thermoelectric properties of two-dimensional $mos_2/mose_2$ heterostructures. *Chinese Journal of Chemical Physics* 29(4), 445–452.
- Xiao, Y. and L.-D. Zhao (2018). Charge and phonon transport in pbte-based thermoelectric materials. *npj Quantum Materials* 3(1), 55.
- Xu, C., P. A. Brown, and K. L. Shuford (2015). Strain-induced semimetal-to-semiconductor transition and indirect-to-direct band gap transition in monolayer $1t-tis_2$. *RSC Adv.* 5, 83876–83879.

- Xu, Y., Z. Li, and W. Duan (2014). Thermal and thermoelectric properties of graphene. *Small* 10(11), 2182–2199.
- Yagmurcukardes, M., R. T. Senger, F. M. Peeters, and H. Sahin (2016, Dec). Mechanical properties of monolayer gas and gase crystals. *Phys. Rev. B* 94, 245407.
- Yan, C., C. Gong, P. Wangyang, J. Chu, K. Hu, C. Li, X. Wang, X. Du, T. Zhai, Y. Li, and J. Xiong (2018). 2d group ivb transition metal dichalcogenides. *Advanced Functional Materials* 28(39), 1803305.
- Yan, J.-A., M. A. D. Cruz, B. Cook, and K. Varga (2015, November). Structural, electronic and vibrational properties of few-layer 2h- and 1t-TaSe₂. *Scientific Reports* 5(1).
- Yang, K., Y. Chen, R. D'Agosta, Y. Xie, J. Zhong, and A. Rubio (2012, Jul). Enhanced thermoelectric properties in hybrid graphene/boron nitride nanoribbons. *Phys. Rev. B* 86, 045425.
- Zahid, F. and R. Lake (2010). Thermoelectric properties of bi₂te₃ atomic quintuple thin films. *Applied Physics Letters* 97(21), 212102.
- Zeng, J., X. He, S.-J. Liang, E. Liu, Y. Sun, C. Pan, Y. Wang, T. Cao, X. Liu, C. Wang, L. Zhang, S. Yan, G. Su, Z. Wang, K. Watanabe, T. Taniguchi, D. J. Singh, L. Zhang, and F. Miao (2018). Experimental identification of critical condition for drastically enhancing thermoelectric power factor of two-dimensional layered materials. *Nano Letters* 18(12), 7538–7545.
- Zhang, G. and Y.-W. Zhang (2015). Strain effects on thermoelectric properties of two-dimensional materials. *Mechanics of Materials* 91, 382 – 398. Mechanics of energy conversion and storage.
- Zhang, G. and Y.-W. Zhang (2017). Thermoelectric properties of two-dimensional transition metal dichalcogenides. *J. Mater. Chem. C* 5, 7684–7698.
- Zhang, Z., Y. Xie, Y. Ouyang, and Y. Chen (2017). A systematic investigation of thermal conductivities of transition metal dichalcogenides. *International Journal of Heat and Mass Transfer* 108, 417 – 422.

- Zhang, Z., Y. Xie, Q. Peng, and Y. Chen (2016, Feb). A theoretical prediction of super high-performance thermoelectric materials based on mos₂/ws₂ hybrid nanoribbons. *Scientific Reports* 6, 21639 EP –. Article.
- Zhao, Q., R. Frisenda, T. Wang, and A. Castellanos-Gomez (2019). Inse: a two-dimensional semiconductor with superior flexibility. *Nanoscale* 11, 9845–9850.
- Zhen, Y.-X., M. Yang, H. Zhang, G.-S. Fu, J.-L. Wang, S.-F. Wang, and R.-N. Wang (2017). Ultrahigh power factors in p-type 1t-zrx₂ (x=s, se) single layers. *Science Bulletin* 62(22), 1530 – 1537.
- Zhou, H., Y. Cai, G. Zhang, and Y.-W. Zhang (2018). Unusual phonon behavior and ultra-low thermal conductance of monolayer inse. *Nanoscale* 10, 480–487.
- Zhuang, H. L. and R. G. Hennig (2013). Single-layer group-iii monochalcogenide photocatalysts for water splitting. *Chemistry of Materials* 25(15), 3232–3238.
- Zólyomi, V., N. D. Drummond, and V. I. Fal’ko (2013, May). Band structure and optical transitions in atomic layers of hexagonal gallium chalcogenides. *Phys. Rev. B* 87, 195403.
- Zólyomi, V., N. D. Drummond, and V. I. Fal’ko (2014, May). Electrons and phonons in single layers of hexagonal indium chalcogenides from ab initio calculations. *Phys. Rev. B* 89, 205416.
- Zuev, Y. M., W. Chang, and P. Kim (2009, Mar). Thermoelectric and magnetothermoelectric transport measurements of graphene. *Phys. Rev. Lett.* 102, 096807.

APPENDIX A

TEMPERATURE DEPENDENCE OF PHONON THERMAL CONDUCTANCE

These calculations are performed mainly based on Mingo and Broido (2005). Ballistic phonon thermal conductance within Landauer framework is defined by

$$\kappa_{ph} = \frac{1}{2\pi} \int d\omega \hbar\omega \tau_{ph}(\omega) \frac{\partial f_{BE}(\omega, T)}{\partial T} \quad (\text{A.1})$$

where D is the width of the two-dimensional sheet and goes to infinity. Phononic transmission at low frequencies can be written as

$$\tau_{ph}(\omega) \simeq \int_{-q(\omega)}^{q(\omega)} \frac{D}{2\pi} dq = \frac{D}{\pi} q(\omega) \quad (\text{A.2})$$

Out-of-plane (ZA) mode exhibit quadratic dispersion

$$\omega = \alpha q^2, \quad q(\omega) = \sqrt{\omega/\alpha} \quad (\text{A.3})$$

Here, coefficient α can be calculated by fitting of the ZA branch where q approaches the Γ point. Contribution of the ZA branch to the phononic transmission becomes

$$\tau_{ph}(\omega) \simeq \frac{D}{\pi} \sqrt{\omega/\alpha} \quad (\text{A.4})$$

The last term to calculate temperature dependency of the thermal conductance is the derivative of the Bose-Einstein distribution function

$$\frac{\partial f_{BE}}{\partial T} = \frac{1}{T} \frac{xe^x}{(e^x - 1)^2} \quad (\text{A.5})$$

By substituting the required terms into Eq. A, phonon thermal conductance for ZA mode is obtained as

$$\kappa_{ph} = \beta T^{3/2} \quad (\text{A.6})$$

where $\beta = 4.46 \left(\frac{D}{\sqrt{\alpha}} \right) \frac{k_B^{5/2}}{2\pi^2 \hbar^{3/2}}$

For in-plane (LA,TA) modes have linear independence of q

$$\omega = v_{LA,TA} q, \quad q(\omega) = \omega / v_{LA,TA} \quad (\text{A.7})$$

$$\tau_{ph}(\omega) \simeq \frac{D}{\pi} \omega / v_{LA,TA} \quad (\text{A.8})$$

After similar calculations, phonon thermal conductance for LA and TA modes takes the following form

$$\kappa_{ph} = \beta T^{3/2} = \gamma T^2 \quad (\text{A.9})$$

where $\gamma = 1.2 \left(\frac{D}{v_{LA,TA}} \right) \frac{k_B^3}{2\pi^2 \hbar^2}$.

VITA

Date and Place of Birth: 01.01.1987, İzmir-Turkey

EDUCATION

2013 - 2019 Doctor of Philosophy in Physics

Graduate School of Engineering and Sciences, İzmir Institute of Technology,
İzmir -Turkey

Thesis Title: THERMOELECTRIC EFFECT IN LAYERED NANOSTRUCTURES

Supervisor: Prof. Dr. R. Tuğrul SENGER

2010 - 2013 Master of Science in Physics

Graduate School of Engineering and Sciences, İzmir Institute of Technology
İzmir -Turkey

Thesis Title: FRÖHLICH POLARON CALCULATIONS IN NON-INTEGER
DIMENSIONAL SPACE AS A MODEL OF CONFINEMENT

Advisor: Prof. Dr. R. Tuğrul SENGER

2005 - 2010 Bachelor of Physics Education

Department of Physics Education, Faculty of Education, Dokuz Eylül University
İzmir - Turkey

PROFESSIONAL EXPERIENCE

2010 - 2019 Research Assistant

Department of Physics, İzmir Institute of Technology,
İzmir -Turkey

PUBLICATIONS

- G. Özbal, J. T. Falkenberg, M. Brandbyge, R. T. Senger, and H. Sevinçli, "Directed growth of hydrogen lines on graphene: High-throughput simulations powered by evolutionary algorithm", Phys.Rev.Materials 2, 073406, Doi:10.1103/PhysRevMaterials.2.073406.
- Burak Özdamar, Gözde Özbal, M. Neşet Çınar, Koray Sevim, Gizem Kurt, Birnur Kaya, and Hâldun Sevinçli, "Structural, vibrational, and electronic properties of single-layer hexagonal crystals of group IV and V elements", Phys.Rev.B 98, 045431, Doi:10.1103/PhysRevB.98.045431.